

A Numerical Simulation Framework for the Design, Management and Optimization of CO₂ Sequestration in Subsurface Formations

Investigators

Hamdi Tchelepi, Associate Professor of Energy Resources Engineering; Lou Durlafsky, Professor of Energy Resources Engineering; and Khalid Aziz, Professor of Energy Resources Engineering.

Abstract

The objective is to develop a numerical simulation framework for modeling subsurface CO₂ sequestration operations. We have made significant progress on several interrelated areas of investigation.

The vertical migration of CO₂ plumes, which are immiscible with the surrounding brine, was investigated using high-resolution simulation. The flux function for buoyancy driven immiscible flow plays an important role in the resulting behavior. Plume stretching, wave interactions, overall migration distances and speeds are discussed. This analysis is a prerequisite for the ongoing study of immiscible CO₂ plume migration with capillary hysteresis.

The behavior of CO₂ gravity currents in sloping aquifers in the presence of residual trapping was investigated. Even though a simple mathematical model that accounts for residual trapping in the wake of the gravity current was used, the analysis sheds light on the long term fate of gravity currents of practical interest. Dependence of the maximum migration distance on initial plume size, aquifer slope, and viscosity ratio is described. This study indicates that regional (gently dipping) aquifers of large extent can be viable storage sites, and that the effectiveness of residual trapping increases dramatically with slope.

Consistent with our objectives to develop a flexible and efficient numerical computational framework, we are investigating the development of high-order AIM (Adaptive Implicit Method) discretizations, in both space and time. High-order approximations were developed using the MOL (Method of Lines) framework as a base. These constructions are high-order (at least second order) in space and time, locally conservative, and unconditionally stable; however, these desirable properties come with a severe positivity restriction in the implicit regions, which limits the time step size. Investigation of artificial-viscosity schemes to remedy these restrictions is ongoing.

The multiscale finite-volume method was extended for compressible multiphase flow

in strongly heterogeneous domains. The accuracy of the formulation is demonstrated for problems with high compressibility levels and strong permeability heterogeneity. This algebraic Operator Based Multiscale Method (OBMM) provides a flexible framework for solving coupled problems of multiphase flow and transport and is applicable to models with unstructured grid. Moreover, OBMM can be used to add multiscale capabilities to standard flow simulators in a straight forward manner.

Development of a stochastic approach for modeling multiscale multi-physics problems is ongoing. The framework is demonstrated for non-equilibrium capillary- pressure formulations. The description leads to a high dimensional transport equation, where one of the dimensions is the saturation random variable. This equation is then solved using standard finite volumes. The flexibility of the framework in linking complex flow behaviors across scales is demonstrated using simple one-dimensional immiscible two-phase flow.

Finally, we describe our proposed flexible formulation for incorporating chemical reactions in our general-purpose simulation framework. The extension will be performed such that we take full advantage of the existing capabilities in GPRS, including, general-compositional, adaptive implicit, unstructured grid, advanced wells, and adjoint enabled. The objective is to be able to model the reactions associated with CO₂ sequestration processes and their interactions with complex multi-component multiphase flow and transport for problems of practical interest.

Introduction

The overall objective of this project is to develop a numerical simulation framework for modeling CO₂ sequestration operations in large-scale heterogeneous formations, such as deep saline aquifers and depleted oil and gas reservoirs. This framework is constructed based on in-depth understanding of the physics in the parameter space of interest for geologic sequestration of CO₂, accurate and computationally efficient numerical algorithms for modeling flow and transport processes in large-scale porous formations, and a flexible extensible computational framework for the design and optimization of CO₂ projects during both the injection and long term storage periods.

During the past year, we worked on several interrelated items: (1) detailed understanding of the physics associated with plume migration and gravity currents, (2) high-order AIM (adaptive implicit method) formulations, (3) multiscale finite-volume formulation for compressible multiphase flow, and (4) development of a general framework for modeling reactions in porous media flows. In this annual progress report, we summarize the most recent developments, which are divided into six sub-projects. These are: (1) vertical migration of CO₂ plumes in porous media, (2) propagation of CO₂ plumes in sloping aquifers with residual trapping, (3) construction of high-order adaptive implicit methods, (4) algebraic multiscale formulation for compressible multiphase flow, (5) stochastic framework for non-equilibrium models of multiphase flow in porous media, and (6) modeling CO₂ mineralization reactions in a general-purpose flow simulator.

These projects deal with different aspects of the numerical framework we are building. The first two projects are aimed at improved understanding of the physical mechanisms that dictate the behavior of CO₂ plumes in porous media. The third and fourth projects are concerned with the development of accurate and computationally efficient numerical methods for modeling the complex behaviors associated with subsurface CO₂ sequestration. The fifth project relates to ongoing development of a stochastic framework for modeling multiphase flow across multiple scales, accounting for possibly having different equations that describe the physics at the different scales. A flexible and computationally efficient framework for modeling reactions associated with CO₂ sequestration processes in natural porous media is the subject of the sixth project.

In the first project, the evolution and vertical migration of a CO₂ plume that is immiscible with the resident brine is studied using very accurate numerical simulations of two-phase flow. The relative permeability effects and the differences in density and viscosity between the CO₂ and the brine can lead to highly complex nonlinear interactions. In this progress report, we focus on the flux function and the behavior of the various saturation fronts in the mean flow. Issues related to spreading, wave interactions, migration distances and speeds are discussed. This analysis serves as a prerequisite to the ongoing analysis of hysteresis effects and capillary trapping on CO₂ plumes in the post-injection period.

In the second project, the long term fate of a CO₂ gravity current that is initially ponded against the boundary of a deep and slightly sloping aquifer is investigated. A simple model is used to represent residual trapping in the wake of the gravity current. The migration distance of the gravity current, and its dependence on the plume size and aquifer slope are discussed.

The third project is on the construction of high-order approximations for the adaptive implicit method (AIM). Accurate simulation of the physics governing subsurface CO₂ sequestration requires solving coupled nonlinear conservation equations in highly heterogeneous domains. For such models, AIM allocates the computational resources when and where necessary. However, standard AIM is first-order in both space and time. Such a low-order treatment may be inadequate for accurate modeling of buoyancy driven transport in the post-injection period. As a result, we have been investigating high-order AIM schemes in both space and time. Our analysis has progressed quite significantly, and we summarize the effort in this report. However, several challenges remain, and we outline our plans for tackling them.

In the fourth project, we describe the extension of the multiscale finite-volume method for compressible multiphase flow in highly heterogeneous formations. This operator based multiscale method (OBMM) is a promising platform for including additional flow mechanisms (e.g., capillarity, buoyancy) as well as for solving problems on unstructured grids. We also report on the recent effort to develop an adaptive multiscale formulation for the nonlinear transport problem (saturation equations).

In collaboration with researchers at ETH, Zurich, we are further developing the stochastic framework for modeling multiphase flow and transport across scales. In this report, we describe the flexibility of this framework in dealing with non-equilibrium models of the capillary pressure for immiscible two-phase flow.

Finally, in the sixth project we describe our recent effort to extend our numerical simulation framework for coupled flow and transport processes to account for the chemical reactions that may be associated with subsurface CO₂ sequestration processes.

Next, we provide a description of the recent developments over the past year. For each of the six sub-projects, we place the activity in the larger context of the numerical framework we are building in this GCEP project, and we report our findings and their significance. Moreover, for each project, we present our conclusions, remarks, ongoing activities, and proposed future plans.

Vertical migration of CO₂ plumes in porous media

Investigators

Hamdi Tchelepi, Associate Professor of Energy Resources Engineering; Amir Riaz, Research Associate

Introduction

The behavior of two-phase flow in porous media under conditions of unstable density stratification is an important and challenging problem applicable to many practical settings of interest. Particularly, in the area of carbon dioxide storage in depleted reservoirs and saline aquifers, the dynamics of two-phase immiscible flows that are gravitationally unstable play a central role. The important issue in this regard is the understanding and prediction of the fate of CO₂ over a time period of geological scale[1]. The success of CO₂ sequestration operations in subsurface geological formations are linked with the ability of the storage site to sequester CO₂ indefinitely. The main mechanisms of sequestration are, microscopic residual trapping, dissolution of CO₂ into brine, and chemical fixing of carbon in the rock[2]. Various time scales as well as the nature of the storage site determine the relative importance of these mechanisms.

The sequestration process can be broadly classified into three phases[3]. Namely, the injection phase where super-critical CO₂ is injected into the storage site[4]. This is followed by the post injection period where CO₂ rises as a buoyant plume. Residual trapping and dissolution will be of importance in this stage. The final stage is thought to be governed by dissolution driven gravitationally unstable flows[5] as well as chemical reactions of CO₂ with the porous rock.

Figure 1 shows a sketch of a CO₂ plume. The nonwetting gas phase is immersed in brine, which is the wetting phase. A buoyancy force per unit volume F_B results in upward motion with velocity proportional to U_B , inducing a downward flow of brine around the plume. During the evolution of the CO₂ plume in the post injection period, the processes of residual trapping and dissolution are expected to play the primary role. While in general, one can expect the CO₂ plume, which is immiscible with the surrounding brine, to rise due to buoyancy, the particular mechanisms of transport are the subject of active research [6, 7, 8].

The main issues that need to be addressed are: (1) How far can the plume rise, (2) what is the velocity of rise and (3) how far does the plume spread during its ascent? The last issue is important from the point of view of dissolution, which occurs immediately when the gas comes into contact with unsaturated brine. However, since the amount of CO₂ that can be dissolved in brine is small, a continuous supply of fresh

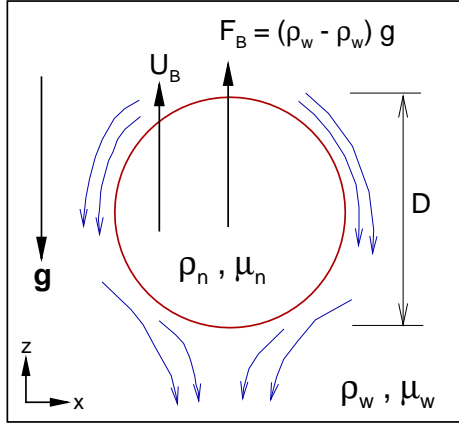


Figure 1: Sketch of the CO₂ plume. The nonwetting gas phase is represented by subscript n and the surrounding brine is the wetting phase denoted by subscript w . A buoyancy force per unit volume F_B induces an upward motion with velocity proportional to U_B .

brine around the buoyant plume can increase dissolution significantly. In this investigation, we analyze the dynamics of the CO₂ plume during the period immediately following the injection phase. We use the Darcy relative permeability model to analyze the dynamics governing the natural convection of the buoyant plume and provide some preliminary estimates of how far and how fast will the plume rise, based on this model. In order to focus on the primary characteristics of transport governed by the Darcy model, we carry out the analysis for homogeneous rocks, without residual trapping and dissolution. Hence, the first order behavior of the system will be considered as a primary guide to subsequently develop a better understanding of more complex processes.

Governing equations and scaling

The immiscible two-phase flow process is modeled by Darcy's equations for each phase, which can be expressed in dimensional form as

$$\mathbf{u}_w^* = -\frac{kk_{rw}}{\mu_w} (\nabla P_w^* + \rho g \hat{\mathbf{z}}) \quad (1)$$

$$\mathbf{u}_n^* = -\frac{kk_{rn}}{\mu_n} (\nabla P_n^* + \rho g \hat{\mathbf{z}}) \quad (2)$$

where the subscripts w and n refer to the wetting and the nonwetting phase, respectively and $\hat{\mathbf{z}}$ is a unit vector in the z -direction. The total velocity and capillary pressure are defined as

$$\mathbf{u}_T^* = \mathbf{u}_w + \mathbf{u}_n \quad (3)$$

$$P_c^* = P_n^* - P_w^* \quad (4)$$

Equations 1 and 2, along with Eqs. 3 and 4, can be used to construct an expression for the nonwetting phase velocity

$$\begin{aligned} \mathbf{u}_n^* &= \frac{\mu_w k_{rn}^*}{\mu_n k_{rw}^* + \mu_w k_{rn}^*} \mathbf{u}_T^* \\ &- k \frac{k_{rw}^* k_{rn}^*}{\mu_n k_{rw}^* + \mu_w k_{rn}^*} \left(\frac{dP_c^*}{dS_w} \nabla S_n - \Delta \rho g \hat{\mathbf{z}} \right) \end{aligned} \quad (5)$$

Similarly, the equation for the total velocity is

$$\begin{aligned} \mathbf{u}_T^* &= -\frac{k}{\mu_w \mu_n} (\mu_n k_{rw}^* + \mu_w k_{rn}^*) \nabla \bar{P}_n^* \\ &+ k \frac{k_{rw}^*}{\mu_w} \left(\frac{dP_c^*}{dS_w} \nabla S_n - \Delta \rho g \hat{\mathbf{z}} \right) \end{aligned} \quad (6)$$

where the density difference $\Delta \rho = (\rho_w - \rho_n)$. Pressure is redefined to be

$$\nabla \bar{P}_n^* = \nabla P_n^* + \rho_n g \hat{\mathbf{z}}. \quad (7)$$

In order to make the above equations dimensionless we use the plume diameter D as the length scale, as shown in Fig. 1 and the buoyancy velocity U_B as the velocity scale,

$$U_B = k \Delta \rho g / \mu_w. \quad (8)$$

Equations 5 and 6 in dimensionless form are

$$\mathbf{u}_n = f_n \mathbf{u}_T - \frac{k_{rw} k_{rn}}{Ca \lambda} \frac{dP_c}{dS_w} \nabla S_n + \frac{k_{rw} k_{rn}}{\lambda} M \hat{\mathbf{z}} \quad (9)$$

$$\mathbf{u}_T = -\frac{\lambda}{M} \nabla P_n + \frac{k_{rw}}{M Ca} \frac{dP_c}{dS_w} \nabla S_n - k_{rw} \hat{\mathbf{z}}, \quad (10)$$

where

$$f_n = \frac{M k_{rn}}{\lambda} \quad (11)$$

$$\lambda = M k_{rn} + k_{rw} \quad (12)$$

$$M = \frac{\mu_w k_{rn}^{(1)}}{\mu_n k_{rw}^{(0)}}. \quad (13)$$

The end point values of relative permeability, $k_{rw}^{(0)}$ and $k_{rn}^{(1)}$, are used to scale relative permeability functions and appear in the definition of the mobility ratio M . The relevant scalings for the nonwetting phase pressure and the capillary pressure are,

$$\bar{P}_n^* = P_n \frac{\mu_n U_B D}{k}, \quad (14)$$

$$P_c^* = P_c \gamma_{nw} \sqrt{\frac{\phi}{k}}, \quad (15)$$

where γ_{nw} is the interfacial tension, ϕ is the porosity and k the permeability. The capillary number, Ca , is defined as

$$Ca = \frac{\mu_n U_B D}{\sqrt{k \phi} \gamma_{nw}}. \quad (16)$$

This capillary number can be interpreted as the macroscopic capillary number. Ca can also be stated in terms of the microscopic capillary number, Ca_m ,

$$Ca = Ca_m \frac{D}{\sqrt{k \phi}}. \quad (17)$$

Equations governing the transport of the nonwetting phase and the incompressibility condition are,

$$\frac{\partial S_n}{\partial t} + \nabla \cdot \mathbf{u}_n = 0, \quad (18)$$

$$\nabla \cdot \mathbf{u}_T = 0, \quad (19)$$

where t is scaled with U_B/D . The boundary conditions are

$$\begin{aligned} \mathbf{u}_T &= 0 \quad ; \quad \mathbf{x} = \pm\infty \\ S_n &= 0 \quad ; \quad \mathbf{x} = \pm\infty \\ \nabla P_n &= 0 \quad ; \quad \mathbf{x} = \pm\infty, \end{aligned} \quad (20)$$

which assume infinite vertical extent. The above equations are characterized by two main nondimensional parameters, which are the time, t , and capillary number, Ca . These parameters can be expressed as

$$t^* = \frac{\mu_n D \phi}{k \Delta \rho g} t, \quad (21)$$

$$Ca = \frac{\Delta \rho g D \sqrt{k}}{\sqrt{\phi} \gamma_{nw}}. \quad (22)$$

Note that the capillary number is independent of viscosity and can also be expressed in terms of the Bond number as,

$$Bo = \frac{\Delta \rho g d^2}{\gamma_{nw}}, \quad (23)$$

$$Ca = Bo \left/ \frac{\sqrt{\phi} d^2}{D \sqrt{k}} \right., \quad (24)$$

where d is some characteristic pore length $\sim \mathcal{O}(10^{-5})$ m. Hence the capillary number in this problem can be interpreted as representing the influence of the ratio of gravity to capillary effects relative to the ratio of the microscopic to macroscopic lengths.

Some particular values of density, viscosity and permeability relevant to the CO₂ sequestration problem are

$$\begin{aligned} \Delta \rho &= 10^3 \text{ kg/m}^3 \\ \mu_w &= 1 \times 10^{-3} \text{ Pa-s} \\ \mu_n &= 0.03 \times 10^{-3} \text{ Pa-s} \\ \gamma_{nw} &= 40 \times 10^{-3} \text{ N/m} \\ \phi &= 0.3 \\ k &= 10^{-14} \text{ m}^2 \\ D &= 10^2 \text{ m} \\ d &= 10^{-5} \text{ m}. \end{aligned}$$

Based on these values, $U_B \sim 10^{-6}$ m/s, and the dimensionless numbers are estimated to be,

$$Bo \sim 10^{-3} \quad (25)$$

$$Ca_m \sim 10^{-5} \quad (26)$$

$$Ca \sim 10^2. \quad (27)$$

The values of these dimensionless numbers may indicate a regime of pore scale instability[9], such that current macroscopic models may not be applicable. However,

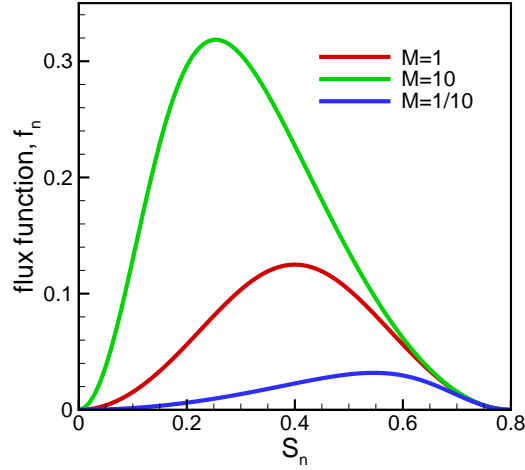


Figure 2: Flux function for zero injection velocity for different values of the mobility ratio. The flux function decays to zero at the maximum and minimum values of saturation. The vanishing gradient at intermediate saturations implies that the saturations move in opposite directions, starting from the stagnation point.

this issue is unresolved and requires extensive investigation. For now, we will use the standard two-phase Eqs. 5 and 6 in order to obtain preliminary estimates regarding the plume evolution.

One-dimensional solution

Before we solve the full 2-D problem, it is useful to look at the 1-D solutions of Eq. 18 to determine the influence of the viscosity ratio and capillary number for some simple cases. Physically, the one-dimensional problem can be constructed as a layer of a lighter nonwetting fluid, unbounded in the lateral extent, which is surrounded by the heavier wetting fluid. The wetting phase is not connected, hence the plume will not rise as a whole. This allows the analysis of the frontal displacements, only as a function of relative permeability and the viscosity ratio. We will designate the top portion of this layer, where the heavier wetting fluid (Brine) is above the lighter nonwetting fluid (CO_2), as the front end. The lower part of the layer, where the heavier fluid is below the lighter fluid, will be referred to as the back end. We assume the relative permeability and capillary functions to be

$$k_{rn} = \left(\frac{S_n - S_{nr}}{\Delta S} \right)^2, \quad (28)$$

$$k_{rw} = \left(1 - \frac{S_n - S_{nr}}{\Delta S} \right)^2, \quad (29)$$

$$\frac{dP_c}{dS_w} = -\frac{1}{k_{rn} k_{rw}}, \quad (30)$$

where $\Delta S = 1 - S_{nr} - S_{wr}$, and S_{nr} and S_{wr} are the residual saturations for the

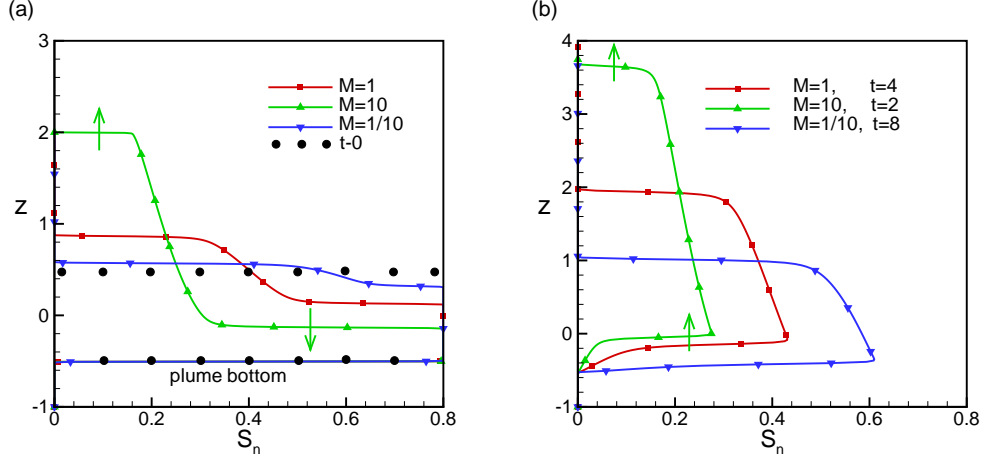


Figure 3: Saturation profiles for a 1-D plume for $Ca = 400$. (a) $t = 1$, and (b) late times. The initial profile with a unit height is indicated by circular symbols in plot (a). The bottom of the plume is stationary while portions of the top end move upwards and downwards according to Eq. 31.

nonwetting and the wetting fluids, respectively. The z -direction component of Eq. 18 with $u_T = 0$ can be expressed as

$$\frac{\partial S_n}{\partial t} + \frac{\partial}{\partial z} \left(\frac{M}{\lambda} k_{rw} k_{rn} - \frac{1}{Ca \lambda} \frac{\partial S_n}{\partial z} \right) = 0. \quad (31)$$

Equation 31 is a weakly parabolic equation for large Ca . Similar to the purely hyperbolic case $Ca \rightarrow \infty$, the solution develops along characteristics based on the flux function $f_{nw} = k_{rw} k_{rn} / \lambda$. The flux function is plotted as a function of the nonwetting saturation in Fig. 2 for various values of the mobility ratio. The plotted curves show that the f_{nw} curve goes through a maximum indicating a zero wave speed at that saturation. This leads to the development of two shocks with opposite speeds at the front end. The upward moving shock spans saturations $0 < S_n < s_{su}$, while the downward moving shock develops for $s_{sd} < S_n < s_{wi}$, where s_{su} and s_{sd} are the shock saturations for the upward and downward moving shocks, respectively. The flux function for the $M = 10$ case, that is when the plume is less viscous than the brine, shows the shock speeds are highest compared to $M = 1$ and $M = 1/10$ cases.

We use the physical capillary dispersion in the problem to obtain high accuracy numerical solutions that converge to the correct entropy solution in the limit of vanishing dispersion. High accuracy numerical solutions are obtained with the 4th order accurate in time Runge-Kutta scheme and with 6th order spatial accuracy through WENO discretization[10]. The capillary dispersion term is solved with 6th order central, compact finite-difference scheme[11].

The solution of Eq. 31 is plotted in Fig. 3(a) for various values of M . The initial condition is a layer of CO_2 of unit length positioned at $z = 0$ with $S_{wi} = 0.8$ and $S_{nr} = 0$, as shown with circular symbols in Fig. 3(a). In the $M = 1$ case, the shock

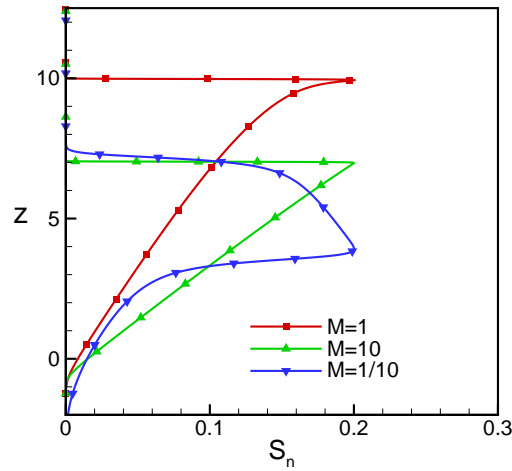


Figure 4: Saturation profiles at the final time ($Ca = 400$) when the maximum saturation has decreased to the threshold saturation $s_t = 0.2$. The front end, for $M = 1$, has moved the farthest while it is at about the same position for $M = 10$ and $M = 1/10$ cases. The corresponding times are $t = 12.5(M = 10)$, $t = 31.5(M = 1)$ and $t = 45.6(M = 1/10)$.

speeds are equal, the upward and downward moving shocks at the top boundary of the layer bifurcate symmetrically about the stationary saturation point. The saturation profile for the stable $M = 1/10$ case is relatively less developed due to small shock speeds, as indicated in Fig. 2. The $M = 10$ case has the highest shock speeds. When the downward moving rear-shock encounters the bottom end of the CO_2 layer, it is reflected upwards. As a result, the maximum saturation at the bottom of the layer decreases below the saturation associated with $df_{nw}/dS_n = 0$, allowing the back end to also move in the upward direction according to f_{nw} . The upward moving back-end now encounters progressively smaller saturations, which leads to a continuous decrease in the maximum saturation of the CO_2 layer. This behavior is shown in Fig. 3(b) for all M cases.

The simulation is stopped when the maximum saturation reaches a threshold value of $s_t = 0.2$. Saturation profiles at the final time, t_f , when the maximum saturation is at the threshold value, s_t , are shown in Fig. 4 for various values of M . The values of t_f corresponding to $M = 1, 1/10$ and 10 , respectively, are $31.5, 46.5$ and 12.5 .

Figure 5 shows the decrease of the maximum saturation with time for various values of M . For the $M = 10$ case, the decrease is rapid and s_{\max} reaches s_t in a short time. During its decrease, the maximum saturation goes through two periods of rapid decay, in between intervals of relatively mild decrease. This pattern is also observed for other values of M , but at delayed times. The first period of rapid decrease of s_{\max} occurs when the downward moving rear-shock reaches the bottom end of the CO_2 layer, which is a stationary shock. The resulting upward reflection of the back end through the expansion wave that was following the downward moving shock, results in a relatively slow decrease of s_{\max} . The upward moving shock wave from the back end is generally faster than the upward moving shock at the front end. Hence, another

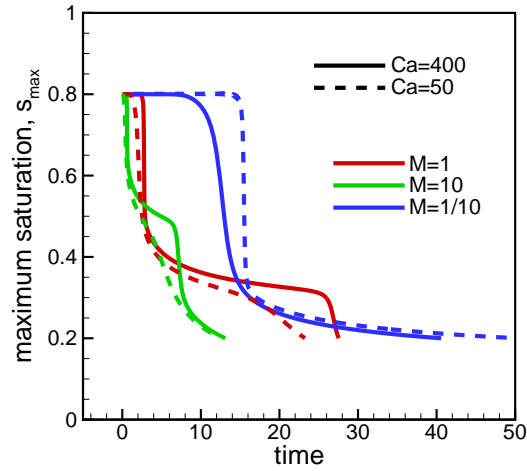


Figure 5: The decay of maximum saturation, s_{\max} in time for different values of M and Ca . For the viscously unstable case $M = 10$, the maximum saturation reduces to the threshold saturation in a very short time, while $M = 1$ and $M = 1/10$ cases require longer times. Decay of s_{\max} occurs through long periods of relatively mild decrease in between short intervals of rapid decrease.

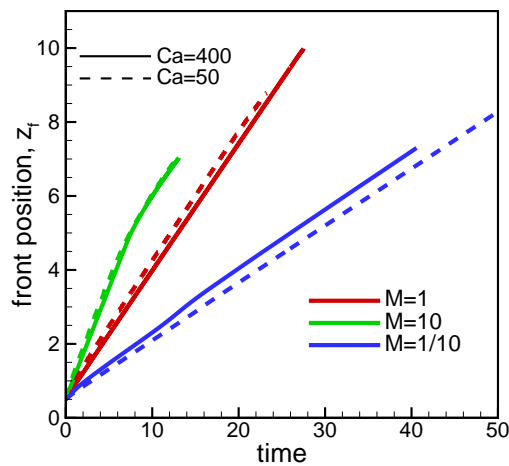


Figure 6: Speed at which the front end of the 1D plume moves upward, plotted for different values of the mobility ratio and the capillary number. Simulation is stopped when the maximum saturation is 0.2. The plume moves fastest at $M = 10$ and slowest at $M = 1/10$. The time to reach the threshold saturation is also longer in the latter case. Capillary number has a small influence on the front position.

shock interaction occurs leading to a rapid decrease in s_{\max} . Small capillary numbers mask periods of sharp decay and give rise to an almost uniformly decreasing trend at all times, as shown in Fig. 5.

The maximum position that the upward moving front reaches at the final time, t_f , determines how large a storage site needs to be for a given amount of CO₂. Figure 6 shows the position of the front, z_f , defined as the location of the saturation $S = 0.1 s_{\max}$. Note that even though the front velocity is larger in the case of $M = 10$, the front does not travel as far as in the $M = 1$ case. The slope of z_f for both $M = 1$ and $M = 1/10$ cases is constant, while that for $M = 10$ case shows a slight decrease at late times.

Two-dimensional dynamics

We now present numerical simulations of the 2-D plume. Unlike the 1-D case presented in the previous section, the entire plume will have a positive upward velocity due to the buoyancy force. Capillary and permeability drag forces act in the opposite direction and the rise velocity of the plume will be set by the balance of these forces. We solve Eqs. 18 and 19 with boundary conditions Eq. 20. The total velocity equation is expressed in terms of the vorticity variable to avoid having to deal with pressure, and to be able to employ periodic boundary conditions with spectral schemes. By taking the curl of Eq. 10 we obtain, for the vorticity $\omega = \nabla \times \mathbf{u}_T$

$$\omega = \frac{1}{\lambda} \frac{d\lambda}{dS_n} \nabla S_n \times \mathbf{u}_T - \lambda \frac{d}{dS_n} \left(\frac{k_{rw}}{\lambda} \right) \nabla S_n \times \hat{\mathbf{z}}. \quad (32)$$

The velocity field is then obtained from the streamfunction, ψ , which is related to vorticity through

$$\nabla^2 \psi = -\omega. \quad (33)$$

Streamwise and spanwise components of velocity, w and u , respectively, are obtained by

$$w = \frac{\partial \psi}{\partial x} \quad (34)$$

$$u = -\frac{\partial \psi}{\partial z}. \quad (35)$$

The relevant boundary conditions for ω and ψ are $\omega = \psi = 0$ at $\mathbf{x} = \pm\infty$. To solve for the streamfunction, a global Galerkin spectral method is employed with Fourier basis functions. We express the discrete expansion of ω and ψ as

$$\omega_{m,n} = \sum_0^J \sum_0^K \hat{\omega}_{j,k} \exp \left(i 2\pi j \frac{m}{MA_z} + i 2\pi k \frac{n}{NA_x} \right) \quad (36)$$

$$\psi_{m,n} = \sum_0^J \sum_0^K \hat{\psi}_{j,k} \exp \left(i 2\pi j \frac{m}{MA_z} + i 2\pi k \frac{n}{NA_x} \right) \quad (37)$$

where $A_z = H/D$ and $A_x = L/D$ are the normalized dimensions of the computational domain in the z and x -directions, respectively. N , M are the number of grid points and J , K are the number of Fourier modes. Equation 33 can now be formulated in the spectral space. Since ω and ψ are real valued, only real parts of the eigenfunctions $\hat{\omega}$ and $\hat{\psi}$ are calculated,

$$\hat{\psi}_{j,k} = \frac{\hat{\omega}_{j,k}}{(\pi j/A_z)^2 + (\pi k/A_x)^2} . \quad (38)$$

After $\hat{\psi}$ is obtained from Eq. 38, it is transformed back into physical space to obtain w and u velocity components from Eqs. 34 and 35. The gradients in the z and x -directions are evaluated through 6th order compact finite difference discretization with symmetric boundary conditions. The domain extents $A_z = 10$ and $A_x = 5$ were found to provide a good approximation to an infinite space.

The transport Eq. 18 is solved with 4th order Runge-Kutta method. The spatial derivatives are evaluated with 8th order accurate compact finite difference discretization. The simulation is started with a circular plume of unit diameter centered at $(z = 0, x = 0)$. The initial plume is slightly diffused to avoid discontinuities in saturation values. Initial velocities are prescribed as $(w = 0, u = 0)$ at $t = 0$. We use $\sim 10^4$ grid points to accurately resolve the steep gradients at the fronts.

Figure 7(left) shows the contour plots of saturation at an early time of $t = 1$ for $M = 1$ and $Ca = 200$. The plume has progressed slightly from its initial position leaving behind a wake of small saturation values. The location of the higher saturation values, indicated by regions with red color, has shifted towards the back end, similar to the 1-D case discussed in the previous section. Due to the generation of spanwise velocity in the 2-D case, the plume profile appears to bulge slightly in the x -coordinate. Figure 7(right) shows the plume profile at a later time $t = 6$. The plume has traveled upwards about 5 nondimensional units at this time. The shape of the plume has deviated significantly from the circular initial profile to attain a pointed tip followed by a broader tail. Velocity vectors plotted in Fig. 7 show that at early times the magnitude of the spanwise velocity is comparable to the streamwise component, which generates significant recirculation around the plume. At later time, Fig. 7(right) shows that the streamwise component is dominant and the spanwise velocity is concentrated only at the tip of the plume. Hence, the ability of the plume to induce downward motion in brine is significantly reduced at later times. As for the 1-D case, the simulation is stopped when the threshold saturation $s_t = 0.2$ is reached.

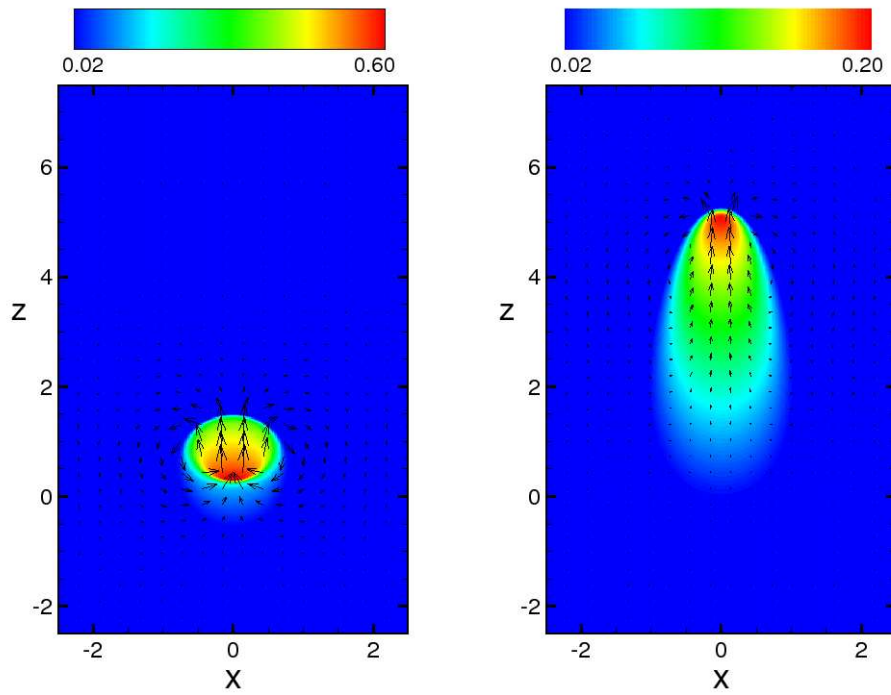


Figure 7: Saturation contour at an early time (left), and at threshold saturation (right), for the 2D case at $M = 1$ and $Ca = 250$. Arrows represent the velocity field induced around the naturally buoyant plume.

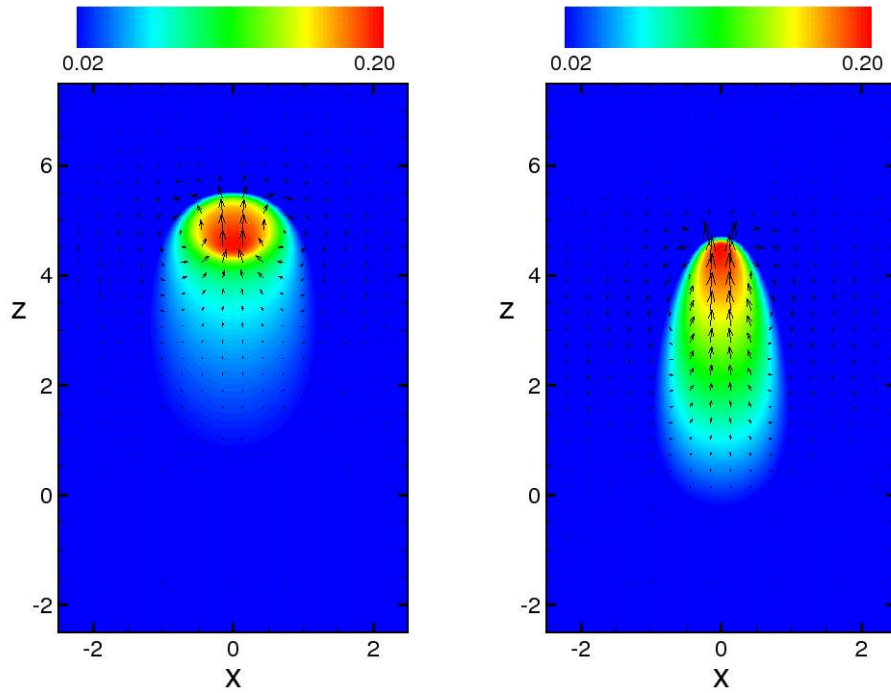


Figure 8: Saturation contour for $M = 10$ (left) and $M = 1/10$ (right).

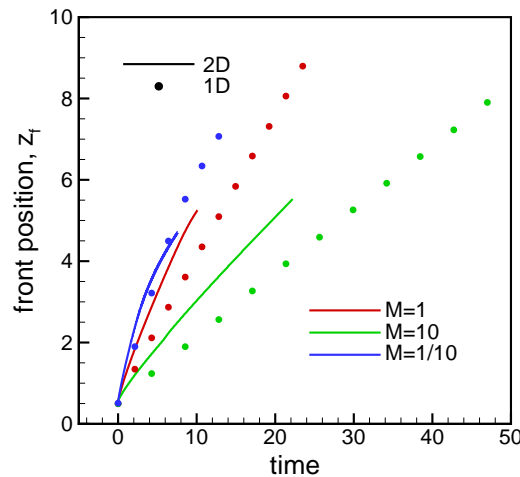


Figure 9: The front positions obtained from 2-D simulations. The plume migration distance in the 2-D case is smaller than the 1-D case. Higher values of the slope of z_f in the 2-D case indicate the contribution of buoyancy driven motion.

The saturation contours of the plume at $M = 10$ and $M = 1/10$ are shown in Fig. 8(left) and (right), respectively, at $Ca = 200$, at times close to t_f . The plume has traveled slightly farther for the $M = 10$ case. The $M = 1/10$ case shows a broadening of the rear section and a narrowing of the tip. However, the $M = 10$ case shows that the plume tends to retain its initial shape with a slight bulging along the spanwise direction. The region of small saturations trails both plumes, but is more prominent for the $M = 10$ case. The velocity vectors show a behavior similar to the $M = 1$ case. High upward velocities are produced in regions of high saturation and the spanwise velocities are localized around the tip of the plume. However, since the plume has stretched out considerably less in the $M = 10$ case, as compared to the $M = 1/10$ case, the induced motion of the brine is fairly uniform around the plume.

The plume motion in 2-D is affected by the buoyancy velocity generated due to the density contrast. Hence, one would expect, compared to the 1-D case, that the plume will tend to propagate much higher into the brine phase. The progress of the tip position z_f is plotted in Fig. 9. The results obtained for the 1-D case are also shown. Surprisingly, Fig. 9 shows that the plume actually rises less as compared to the 1-D case. Although z_f increases much more rapidly in the 2-D case, indicating a higher upward velocity due to buoyancy, the threshold saturation is reached at an earlier time for all M values, compared to the 1-D case. Hence, the plume can only travel about half as much compared to its 1-D counterpart. Two dimensional results indicate that the slope of z_f remains approximately constant throughout the simulation for the $M = 1/10$ case. On the other hand, the slope begins to decrease slightly for $M = 1$ and considerably more for $M = 10$ case. This indicates that the buoyancy generated upward velocity decreases with time such that for $M = 10$, the slope of z_f tends to drop to the 1-D level.

An important characteristic regarding the motion of the plume is the magnitude of the upward velocity generated due to buoyancy. If this velocity is constant then the

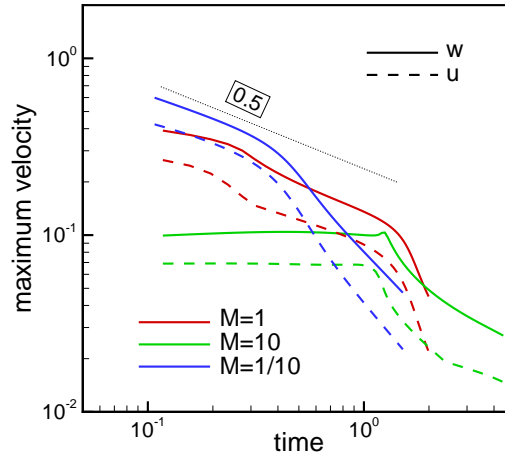


Figure 10: Maximum values of buoyancy induced velocity as a function of time. Solid line shows the maximum values of the streamwise w -component, dashed line represents the spanwise u -component. Both w_{\max} and u_{\max} start out at larger values and progressively decrease at later times, for $M = 1$ and $M = 10$. An approximate slope of $1/2$ is indicated by the dotted line. Maximum velocities remain constant during the initial phase for $M = 1/10$.

plume can rise indefinitely in the absence of residual trapping, as long as there is a sufficient level of density difference between the fluids. In order to determine how does the upward velocity evolve and how far can the buoyancy force lift the plume during its propagation, we plot the maximum values of velocity for both the w and u -components in Fig. 10. The maximum streamwise velocity has the highest magnitude for the $M = 10$ case, followed by $M = 1$ and $M = 1/10$ cases. Only in the case of $M = 1$ is this velocity related entirely to the density contrast. However, even in this case, the non-monotonicity of the mobility (λ) profile[12] contributes to vorticity generation and adds to the buoyancy driven velocity. The $M = 1/10$ case has the smallest velocity at the onset due to the favorable viscosity difference at the top of the plume.

Discussion and conclusions

The dimensional values of the height reached by the plume and the time it takes to reach that height can be estimated based on the physical values of the parameters given in section 2. Table I provides this information for different values of the mobility ratio and the capillary number for both 1-D and 2-D cases. The influence of the increase in capillary number is an increase in the values of both t_f^* and z_f^* since a greater magnitude of capillary dispersion at smaller values of Ca leads to higher rates of reduction of the maximum saturation, and consequently, smaller values of t_f^* . One-dimensional results are generally higher than the corresponding 2-D values. From Table I, we observe that the former are almost twice as much as the latter. For the 2-D case, the longest time to reach the final state is about 2000 yrs for the $M = 1/10$ case at $Ca = 400$, where the plume rises to a distance of 610 meters. The unfavorable viscosity, $M = 10$, case shows significantly smaller values of t_f^* and z_f^* . Our results

M	Ca	1-D		2-D	
		$t_f^*(\text{yrs})$ $\times 10^3$	$z_f^*(\text{m})$ $\times 10^2$	$t_f^*(\text{yrs})$ $\times 10^3$	$z_f^*(\text{m})$ $\times 10^2$
1	50	1.84	8.78	0.64	4.20
	200	2.40	9.42	0.80	5.26
	400	2.12	9.70	0.92	6.03
1/10	50	4.00	8.27	1.26	4.20
	200	3.87	8.11	1.76	5.53
	400	3.63	7.83	2.04	6.10
10	50	1.00	6.91	0.48	3.82
	200	0.66	7.18	0.61	4.70
	400	1.03	6.94	0.70	5.09

Table I: Dimensional values of the time t_f^* required to reach the maximum height z_f^* , for various values of M and Ca . Results for both 1-D and 2-D problems are noted.

indicate that for the $M = 10$ case at $Ca = 400$, the plume is sequestered in about 700 yrs after rising 500 m.

The initial size of the CO_2 plume, here the diameter D , determines to a large extent, how much the plume will rise and with what velocity. In fact, the vertical dimension of the plume is relatively more important since the longer it takes for the wave interaction to occur between the forward and the rear shocks, the longer the maximum saturation can remain at the initial level, resulting in higher upward velocities. Although, the spanwise wave interaction also becomes important, as we showed for the 2-D case, its effect is secondary to that of the streamwise mechanism. For this reason, the maximum upward velocity remains constant for the initial period for the $M = 1/10$ case, while it decays at a steady rate of $\propto 1/2$ for $M = 1$ and $M = 10$ cases.

Future work

We neglect capillary trapping and hysteresis in this analysis, therefore, we stop the simulation when the maximum saturation is reduced to some small value. If one interprets this threshold saturation as the residual, trapped saturation, then our results can be used as a prediction of the upper bounds on the final time and the maximum height for the case with hysteresis. The study of plume migration with hysteresis is the next step in our analysis and is currently under investigation. Based on preliminary analysis, the challenge is to find the right entropy solution for the waves at the front end of the plume, which are on different relative permeability curves related to hysteretic behavior. Another mechanism of importance that will be investigated is the dissolution of CO_2 in brine, which has the effect of increasing the density of saturated brine while keeping the volume approximately the same. The heavier saturated brine will sink generating a stronger circulation current around the plume. Three-dimensional effects are another potential avenue in which to extend the current analysis. Finally, the applicability of the Darcy scale macroscopic description of the flow during the drainage process needs to be clearly established, since the Bond

numbers and the capillary numbers for the CO₂ sequestration problem are very similar to the cases where microscopic instability is observed.

Propagation of CO₂ plumes in sloping aquifers with residual trapping

Investigators

Franklin M. Orr, Jr., Professor of Energy Resources Engineering; Hamdi Tchelepi, Associate Professor of Energy Resources Engineering; Marc Hesse, Graduate Research Assistant.

Introduction

As long as the CO₂ plume moves due to buoyancy, CO₂ is trapped by capillary forces in the wake of the plume, and it is left behind as trapped/residual saturation (S_{gr}). Residual CO₂ is considered immobile on the reservoir timescale[13], and it is currently assumed that the residual CO₂ will remain immobile over the timescale that is necessary to dissolve it into the brine. It is therefore assumed that CO₂ that has been trapped as residual saturation cannot leak back into the atmosphere over the entire storage period. Early numerical simulations of CO₂ storage in saline aquifers[14, 15] did not show significant amounts of residual trapping, because the relative permeability models did not account for hysteresis, and residual gas saturations were commonly set to $S_{gr} = 0.05$. More recently it has been demonstrated that relative permeability hysteresis can increase the trapped/residual CO₂ saturation to $S_{gr} \approx 0.4$ in strongly water-wet reservoirs[16]. Various numerical simulations have now demonstrated that residual trapping can immobilize significant amounts of CO₂ relatively soon after the end of the injection period[16, 17, 18, 19, 20].

It has been suggested to store CO₂ in large, gently dipping regional aquifers that do not have a structural trap, because they provide very large storage volumes often near large point sources of CO₂[21]. In such aquifers we rely entirely on other trapping mechanisms to prevent CO₂ leakage. Figure 11 illustrates the scenario, CO₂ is injected into the sloping aquifer several hundred kilometers from the outcrop. As the CO₂ plume migrates updip towards the outcrop, its volume is reduced by residual trapping until it is exhausted and reaches its maximum migration distance[21]. The maximum migration distance is an important length scale for the selection of the injection site. The total migration time also puts an upper limit on the time that is available for leakage, and is therefore an important time scale.

To focus the attention on the interaction of gravity driven flow with residual saturation in a sloping aquifer, we choose a simple model. We assume a sharp interface, a constant residual saturation, and a semi-infinite domain. These assumptions simplify the governing equations significantly, and allow some analysis. We believe that the main features of our simple model will also apply to more complex

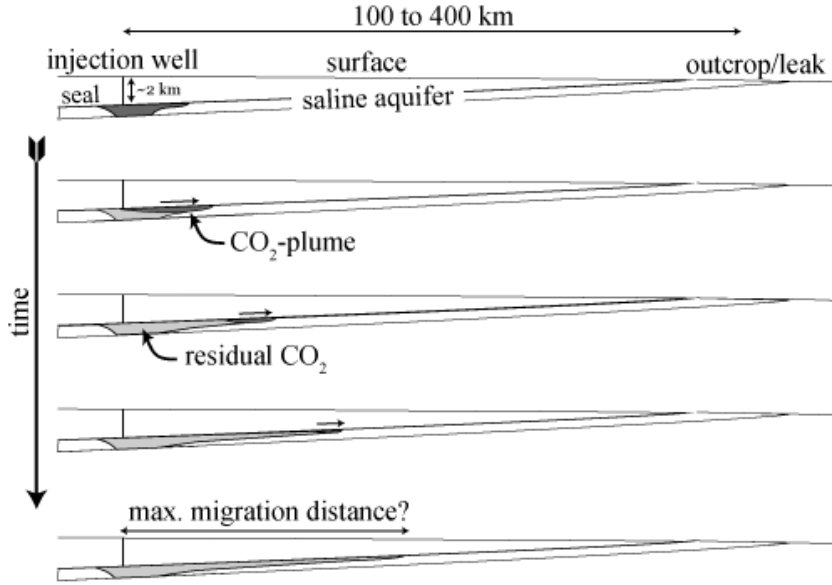


Figure 11: Migration of CO₂ in a gently dipping regional aquifer.

real flows.

Derivation of the governing equation

We consider a finite volume of CO₂ migrating along the top of a very deep porous layer saturated with water. We assume that the height of the interface between the fluids is small compared to the thickness of the porous layer, so that the porous layer can be considered semi-infinite in the vertical direction. We assume that the two fluids are immiscible, separated by a sharp interface, and that the saturations are constant within each fluid. During imbibition when CO₂ is replaced by brine, a constant trapped/residual gas saturation S_{gr} is left behind. During drainage, a constant irreducible/connate water saturation is left behind S_{wc} . The change of the volume of CO₂, ΔV_g , is given by

$$\Delta V_g = \Delta x \Delta h \phi S_g = \Delta x \Delta h \phi (1 - S_{wc}), \quad (39)$$

where $h(x, t)$ is the height of the interface separating the fluids, measured down from the top of the reservoir. S_g is the saturation of CO₂ in the plume which is given by the connate saturation of brine ($S_g = 1 - S_{wr}$), and ϕ is the porosity of the medium, which is assumed to be constant.

We assume the gravity current has a large aspect ratio so that the pressure is hydrostatic and flow is predominantly in the along slope direction. The pressure at the top of the porous medium ($z = 0$) is

$$\begin{aligned} p(x, z = 0, t) &= p_0 - g(\rho + \Delta\rho) [x \sin \theta - h(x, t) \cos \theta] \\ &\quad - g\rho h(x, t) \cos \theta, \end{aligned}$$

where ρ is the density of the gas, the density of the surrounding water is $\rho + \Delta\rho$, and p_0 is the pressure at the coordinate origin. The hydrostatic pressure at any point in the

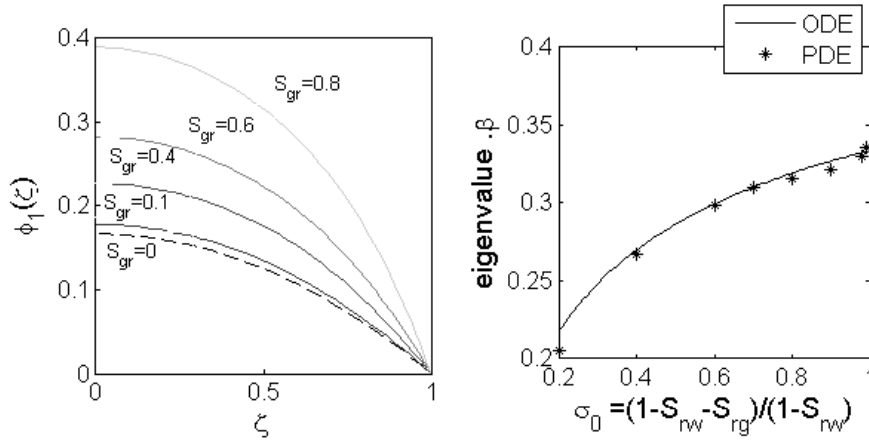


Figure 12: The self-similar current shapes for several values of the residual saturation, and the eigenvalue β that determines the scaling relations (46), have been determined solving the non-linear eigenvalue problem numerically.

gas plume is given by

$$p(x, z \leq h(x, t), t) = p_0 - g(\rho + \Delta\rho)x \sin \theta + g \cos \theta (\Delta\rho h(x, t) + \rho z)$$

The movement of the gas is assumed to be described by Darcy's law given by

$$\begin{aligned} \mathbf{q}_g &= -\lambda_g (\nabla p(x, z, t) - \nabla p_H) \\ &= -\lambda_g \left(\nabla p - \rho g \begin{pmatrix} -\sin \theta \\ \cos \theta \end{pmatrix} \right) \end{aligned}$$

where p_H is the hydrostatic gradient in a single phase fluid, given by $p_H(x, z, t) = p_0 - \rho g x \sin \theta + \rho g z \cos \theta$. The mobility of the gas is defined as $\lambda_g = k k_{rg}^* / \mu_g$, where k is the permeability of the medium, assumed to be constant, the endpoint relative permeability of the gas k_{rg}^* is defined by $k_{rg}^* = k_{rg}(1 - S_{wr})$, and μ_g is the viscosity of the gas. The along-slope component of the flux is given by

$$q = -\lambda_g \Delta\rho g \left(-\sin \theta + \cos \theta \frac{\partial h}{\partial x} \right).$$

The flux difference across the control volume per unit time is given by

$$Q|_x - Q|_{x+\Delta x} = hq|_{x,t} - hq|_{x+\Delta x,t}.$$

Finally we need to consider the CO_2 that is left behind in the areas where the height of the thickness of the current is decreasing. The volume of residual gas left behind per unit time is given by

$$R(x, t) = \begin{cases} \Delta x \Delta h \phi S_{gr}, & \text{for } \frac{\partial h}{\partial t} \leq 0, \\ 0, & \text{for } \frac{\partial h}{\partial t} > 0, \end{cases}$$

where S_{gr} is the immobile trapped/residual gas saturation left behind as gas is displaced by water. The conservation of gas volume in the control volume Δx and over time Δt can therefore be written as

$$\Delta V = (Q(x, t) - Q(x + \Delta x, t)) \Delta t + R.$$

In the limit $\Delta x \rightarrow 0$ and $\Delta t \rightarrow 0$ we obtain the following non-linear advection diffusion equation

$$\frac{\partial h}{\partial t} = \kappa(x, t) \frac{\partial}{\partial x} \left(h \left(-\sin \theta + \cos \theta \frac{\partial h}{\partial x} \right) \right), \quad (40)$$

with the discontinuous coefficient

$$\kappa(x, t) = \begin{cases} \kappa_1 = \frac{k\lambda_g \Delta \rho g}{\phi(1-S_{wc}-S_{gr})}, & \text{for } \frac{\partial h}{\partial t} \leq 0, \\ \kappa_0 = \frac{k\lambda_g \Delta \rho g}{\phi(1-S_{wc})}, & \text{for } \frac{\partial h}{\partial t} > 0. \end{cases} \quad (41)$$

The residual saturations S_{wc} and S_{gr} are between 0 and 1, so that $S_{wr} + S_{gr} \leq 1$, hence $\kappa_1 \geq \kappa_0$. The nature of equation 40 becomes clearer if we expand the right hand side to separate the advective and diffusive terms

$$\frac{\partial h}{\partial t} + v[x, t, \theta] \frac{\partial h}{\partial x} = D[x, t, \theta] \frac{\partial}{\partial x} \left(h \frac{\partial h}{\partial x} \right). \quad (42)$$

The advective velocity is given by $v = \kappa[x, t] \sin \theta$, and the diffusion coefficient is given by $D = \kappa[x, t] \cos \theta$. Note a diffusion coefficient has dimensions of $L^2 T^{-1} \Omega^{-1}$, where Ω is the dimension of the dependent variable, in this case the dependent variable is $h(x, t)$ which has dimension L , therefore the diffusion coefficient has dimensions of velocity $[D] = [v] = [\kappa] = LT^{-1}$.

For a horizontal surface ($\theta = 0$), the equation becomes parabolic and is the one dimensional equivalent of the equation derived by Kochina *et al.*[22] for the radial case. In the limit of no residual trapping ($S_{rg} = 0$) the equation reduces to the form investigated by Huppert and Woods[23]. For the numerical solution of Equation (42) we choose the following dimensionless variables

$$\eta = h/H_0, \quad \chi = x/L_0, \quad \sigma = \kappa/\kappa_1, \quad \tau = t/t^*,$$

with the time scale $t^* = L_0^2(\kappa_1 H_0 \cos \theta)^{-1}$, so that we obtain the equation

$$\frac{\partial \eta}{\partial \tau} = \sigma(\chi, \tau) \frac{\partial}{\partial \chi} \left(\eta \left(\text{Pe} + \frac{\partial \eta}{\partial \chi} \right) \right),$$

where $\text{Pe} = L_0 v / (H_0 D) = L_0 / H_0 \tan \theta$ is a Peclet number. All numerical simulations reported here had a rectangle function initial condition

$$h(\chi, \tau = 0) = u(\chi + 1/2) - u(\chi - 1/2), \quad (43)$$

where $u(\chi)$ is the unit step function. The initial volume of the plume is unity, the initial volume of mobile CO_2 within the plume is $V_0 = S_g = 1 - S_{wc}$. The discontinuous coefficient σ is now given by:

$$\sigma[\chi, \tau] = \begin{cases} \sigma_1 = 1, & \partial \eta / \partial \tau \leq 0; \\ \sigma_0 = \frac{1-S_{wc}-S_{gr}}{1-S_{wc}}, & \partial \eta / \partial \tau > 0. \end{cases} \quad (44)$$

All numerical simulations used a grid spacing of $\Delta \chi = 0.02$, and the simulation was terminated when the volume of mobile CO_2 in the plume had decreased to a value of $V_g = 10^{-3} V_0$.

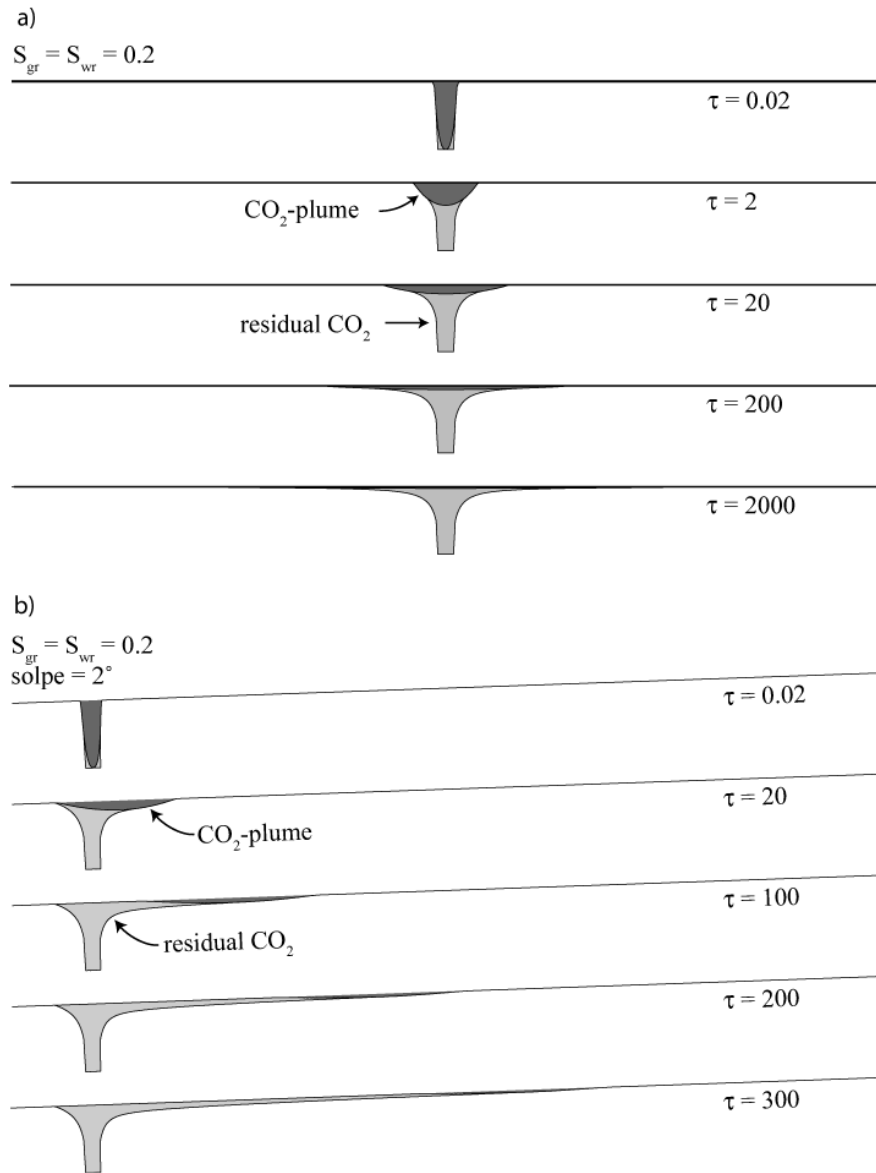


Figure 13: The numerical solution to equation 45 with a unit square initial condition is shown for a horizontal (a) and a sloping aquifer (b).

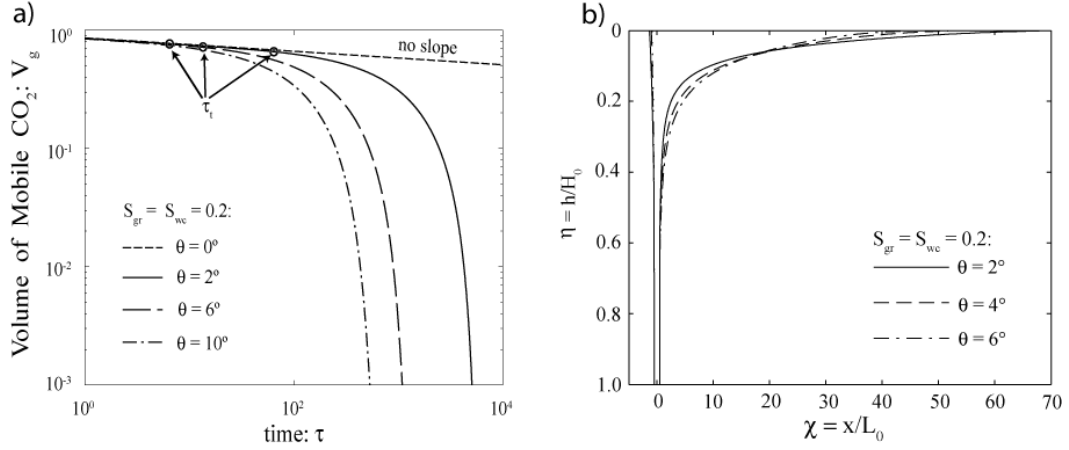


Figure 14: a) Evolution of plume volume with time at constant $S_{gr} = S_{wc} = 0.2$ for various slope angles. The transition time τ_t from power law to super-exponential behavior is marked by circles. b) The area of the aquifer saturated with trapped/residual CO₂ is shown for slope angles θ of 2°, 4°, and 6°.

Horizontal aquifers

The evolution of a CO₂ plume in a horizontal aquifer is shown in figure 13a. In a horizontal aquifer ($\theta = 0$) the governing equation reduces to

$$\frac{\partial h}{\partial t} = \kappa(x, t) \frac{\partial}{\partial x} \left(h \frac{\partial h}{\partial x} \right). \quad (45)$$

Kochina *et al.*[22] have shown that the radial equivalent to this problem has a self-similar solution of the second kind, and the same is true in this case. In these problems the exponents of the self-similar variables are not generally ratios of integers and cannot be determined from dimensional analysis. Instead these exponents have to be found from a non-linear eigenvalue problem[24]. Another characteristic of these problems is that a constant multiplier appears in the self-similar variables that cannot be determined in the general case[24]. An analysis similar to that of Kochina *et al.*[22] gives the following scaling laws for the front position x_f , the current thickness h_{max} and the volume of mobile CO₂ in the plume V_g

$$\begin{aligned} x_f &\propto t^\beta, \\ h_{max} &\propto t^{2\beta-1}, \\ V_g &\propto t^{3\beta-1}. \end{aligned}$$

The dependence of the eigenvalue β on S_{cw} and S_{gr} has been determined numerically and is shown in Figure 12. For $S_{gr} \rightarrow 0$ the eigenvalue $\beta \rightarrow 1/3$, and the scaling relation obtained from a scaling analysis is recovered. The volume of the current is only conserved in this case, and for $\beta < 1/3$ the exponent of V_g is negative, so that the volume of the plume decreases as a power law in time. This suggests that residual trapping reduces the volume of the current quickly in the beginning, but the rate of residual trapping at late time is very low. As the residual saturation increases, β decreases, and the front of the CO₂ plume slows down. The height at the center of the plume decreases as a power law as well, and the plume slumps rapidly initially and more slowly later on. The height at the center decreases faster as S_{gr} is increased.

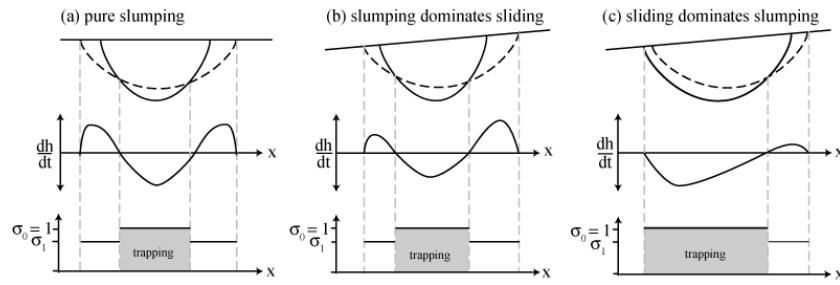


Figure 15: The top row shows the interface of the CO₂ plume at two subsequent times. The corresponding derivative that determines the value of the coefficient σ is shown in the second row. The bottom row shows the coefficient and indicates the region where CO₂ is trapped as residual saturation.

Sloping aquifers

For sloping aquifers ($\theta \neq 0$), the solution is no longer self-similar, and no analytic results exist. Therefore we present numerical solutions to Equation (42), and typical results are shown in Figure 13b. The CO₂ plume migrates updip leaving a large trail of residual saturation in its wake. Figure 14a compares the evolution of the plume volume for various dip angles. For the horizontal case we observe that the volume decays as a power law as predicted. In a sloping aquifer the evolution of the volume can be divided into two periods. An initial period of power law decay, similar to the horizontal case, is followed by a rapid super-exponential decrease of the plume volume. As the slope increases the time of the transition τ_t from the power law to the super-exponential behavior occurs earlier (Figure 14). Residual trapping is therefore much more effective in sloping aquifers than in horizontal aquifers. The rate of residual trapping continuously decreases in horizontal aquifers. In sloping aquifers on the other hand the rate of residual trapping only decreases initially and then starts to increase dramatically.

Figure 15 explains the change from the power law to the super-exponential decay. In a horizontal aquifer (Figure 15a), the CO₂ plume slumps symmetrically under gravity, the height of the current decreases in its center ($dh/dt < 0$), and residual trapping is restricted to the central part of the plume. In a sloping aquifer, the CO₂ plume is both slumping, due to the across-slope component of gravity, and sliding sideways due to the along-slope component of gravity. Initially the slumping dominates over the sliding (Figure 15b), and similar to the horizontal case residual trapping is restricted to the center of the plume. The scaling for the height (46) shows that the slumping slows with time and at some point the sliding dominates over the slumping (Figure 15c). In this case, the height of the current is decreasing over the whole back half of the plume, and the area where residual trapping occurs is increasing. The transition between the two regimes occurs when the second maximum in the derivative dh/dt disappears. The circles in Figure 14 show this transition time τ_t , and we see that it pinpoints the change from power law to super-exponential behavior. We see that the transition time decreases with increasing slope. Finally we discuss the interesting question of the effect that slope has on the maximum migration distance x_{max} of the injected CO₂. While one might expect the CO₂ plume to migrate farther with increasing aquifer dip, our numerical results show that the maximum

migration distance decreases with increasing slope. This surprising result becomes clear when we consider the following geometric argument (Figure 14b). The CO₂ plume must be exhausted once the volume of trapped/residual saturation in the area swept by the plume equals the initial volume of CO₂. The total area of the aquifer A_t that needs to be swept by the CO₂ plume is $A_t = (1 - S_{wc})/S_{gr}A_0$. As the slope increases, the CO₂ plume migrates sideways (slides) faster and slumps more slowly, and it therefore has a greater vertical sweep. Since A_t is constant, increased vertical sweep leads to a shorter migration distance.

Implications for CO₂ storage in saline aquifers.

The results presented above suggest that residual trapping will be very effective in sloping aquifers, even if the dip is very small. We will explore the length and time scales with an example calculation, using the same physical properties used above. We assume a slope of $\theta = 4^\circ$, a connate brine saturation $S_{wc} = 0.1$, a trapped/residual CO₂ saturation of $S_{gr} = 0.2$, an initial plume width at the end of injection of $L_0 \approx 1000\text{m}$, and a plume height of $H_0 \approx 100\text{m}$. In this case $\text{Pe} = 0.699$ and $\sigma = 0.778$. Numerical solution of Equation (43) gives the following maximum migration distance:

$\chi_{max} \approx 50$. The dimensional maximum migration distance in this case is $x_{max} = \chi_{max} * L_0 = 50 \text{ km}$ updip of the injection site. This example suggests that residual trapping can contain the injected CO₂ within reasonable distance of the injection well. Therefore storage in gently sloping aquifers without a structural trap may be possible if the injection site is selected to be far enough from the expected leakage location.

Further work on sloping aquifers.

The results presented above on the interaction of aquifer slope and residual trapping are preliminary, and we intend to expand them to cover the whole parameter space in $\text{Pe}[\theta, L_0/H_0]$ and $\sigma[S_{gr}, S_{wc}]$. Preliminary results suggest that simple scaling laws for the dependence of τ_t , τ_{max} , and χ_{max} on Pe and σ exist. And we will present a full discussion in our next report. An extension of this analysis to the radial case would allow more realistic estimates of the maximum migration distance, and would provide a simple tool for the screening of potential storage sites.

Conclusions

Semi-analytic results for a plume spreading in a horizontal aquifer, show that the volume of the mobile CO₂ plume decays as a power law. Therefore, the efficiency of residual trapping in horizontal aquifers decreases with time. In sloping aquifers, an initial power law decay is followed by super-exponential decrease of the mobile CO₂ volume. This result suggests that residual trapping will be an effective way to reduce the volume of mobile CO₂ in sloping aquifers. The increased vertical sweep in sloping aquifers also leads to a decrease in the maximum migration distance with increasing slope. Due to this enhanced residual trapping, sloping aquifers appear to be reasonable targets for CO₂ storage. Aquifers without a structural trap may be considered as potential storage sites, if the injection site is sufficiently far away from the potential leakage locations.

Construction of High-Order Adaptive Implicit Methods for Reservoir Simulation

Investigators

Hamdi Tchelepi, Associate Professor of Energy Resources Engineering; Romain de Loubens, Graduate Research Assistant; Amir Riaz, Research Associate.

Introduction

The success of the Adaptive Implicit Method (AIM) in reservoir simulation is mostly due to its increased efficiency compared to the traditional IMPES or FIM formulations (see [25], [26], [27], [28], [29] and [30]). The reduction of the computational cost comes from the mixed implicit-explicit treatment of the individual grid block variables. However the standard AIM discretization of the mass conservation equations is only first-order accurate in space and time. We are developing high-order AIM approximations, for both space and time, in order to enhance the solution fidelity and improve the overall computational efficiency.

In the first section we present a numerical analysis of standard AIM. The first part of this analysis focuses on the consistency and convergence properties in the presence of implicit-explicit boundaries. Then we study some important monotonicity properties in the one-dimensional case. In the second section, we propose an AIM formulation based on highly accurate MOL schemes. Fully high-order AIM schemes are derived and then tested in 1D and 2D. Finally, we present an artificial viscosity method to improve the monotonicity restriction in the implicit regions.

Numerical analysis of the standard AIM

Local inconsistency and convergence study

Consider one-dimensional flow of two immiscible phases in a porous medium. Under certain assumptions, this problem is described by the Buckley-Leverett equation

$$\frac{\partial s}{\partial t} + \frac{\partial f(s)}{\partial x} = 0, \quad (46)$$

where it is assumed for simplicity that $f'(s) \geq 0$. The initial and boundary conditions are given by

$$s(x, 0) = s_{wc}, \quad s(0, t) = s_{wi}, \quad (47)$$

where s_{wc} is the connate water saturation and s_{wi} the inlet saturation. In the following, we consider a uniform grid of size m , with a unique implicit-explicit boundary between blocks $(i - 1)$ and (i) (see figure 16). Here information propagates from left to right so this configuration corresponds to an I→E boundary.

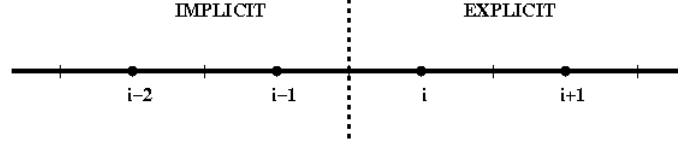


Figure 16: Schematic of an implicit-explicit (I-E) boundary

For this configuration, the standard AIM discretization reads:

$$0 = \frac{s_j^{n+1} - s_j^n}{\Delta t} + \frac{1}{\Delta x} [f(s_j^{n+1}) - f(s_{j-1}^{n+1})], \quad j < i, \quad (48)$$

$$0 = \frac{s_j^{n+1} - s_j^n}{\Delta t} + \frac{1}{\Delta x} [f(s_j^n) - f(s_{j-1}^{n+1})], \quad j = i, \quad (49)$$

$$0 = \frac{s_j^{n+1} - s_j^n}{\Delta t} + \frac{1}{\Delta x} [f(s_j^n) - f(s_{j-1}^n)], \quad j > i. \quad (50)$$

Using Taylor series expansions we can show that the truncation error in the first explicit block ($j = i$) is given by

$$E_i^n = -\frac{\Delta t}{\Delta x} [f(\tilde{s})_t]_i^{n+1} + \mathcal{O}(\Delta x) + \mathcal{O}(\Delta t) + \mathcal{O}(\Delta t^2/\Delta x). \quad (51)$$

The above equation indicates that the standard AIM scheme is inconsistent at the transition from an implicit to an explicit region. Similarly, it is inconsistent at the transition from an explicit to an implicit region. But by construction the standard AIM scheme is stable, so we do not expect the discretization errors at the various I-E boundaries to be amplified with time. Nevertheless, convergence is not guaranteed a priori because the Lax equivalence theorem does not apply. Hence we need an error analysis to understand how these discretization errors propagate and to deduce the convergence properties.

A linear error analysis shows that in the case of a fixed I-E boundary, the error after N time steps is given by

$$\mathcal{E}^{(N)} = \sum_{k=1}^N \mathbf{M}^{N-k} \tilde{\mathcal{S}}^{(k)}. \quad (52)$$

Here \mathbf{M} is the standard AIM operator corresponding to the mesh size $\Delta x = L/m$ and the time step size $\Delta t = T_f/N$, while $\tilde{\mathcal{S}}^{(k)}$ is a first-order source term due to the

inconsistency at the I-E boundary. The matrix vector products in (52) can be computed exactly, and we can prove that in the sense of the infinite norm, we obtain

$$\lim_{\substack{\Delta x, \Delta t \rightarrow 0 \\ \Delta t < \Delta x}} \mathcal{E}^{(N)} = 0. \quad (53)$$

This statement means that in this particular case the standard AIM scheme is convergent, even though it is inconsistent at the I-E boundary. In fact, the convergence properties rely on the dissipative nature of the discretization. In practice, each I-E boundary may create a “kink” in the solution profile. Those kinks are of order one, so they are comparable to the numerical dispersion. But as we will see in the following subsections, in general the standard AIM still verifies strong monotonicity properties

Linear positivity and the maximum principle

In the linear case, the numerical approximation at t^{n+1} is given by

$$\mathbf{s}^{(n+1)} = \mathbf{M}\mathbf{s}^{(n)}, \quad (54)$$

where \mathbf{M} is the standard AIM operator. It is easy to show that this operator satisfies $\mathbf{M} \geq 0$ (component-wise inequalities), which means that it is monotone. In particular, if $\mathbf{s}^{(n)} \geq 0$, we have

$$\mathbf{s}^{(n+1)} = \mathbf{M}\mathbf{s}^{(n)} \geq 0. \quad (55)$$

The above statement shows the linear positivity of the standard AIM scheme. In fact the monotonicity of \mathbf{M} implies that this scheme satisfies the maximum principle, which is an even stronger monotonicity property. Indeed, if $\mathbf{s}^{(n)} \leq C_1 \mathbf{e}$ (component-wise inequality with $\mathbf{e} = (1, \dots, 1)^T$) for some arbitrary constant C_1 , then

$$\mathbf{s}^{(n+1)} = \mathbf{M}\mathbf{s}^{(n)} \leq C_1 \mathbf{M}\mathbf{e} = C_1 \mathbf{e}. \quad (56)$$

Similarly if $\mathbf{s}^{(n)} \geq C_2 \mathbf{e}$, we obtain $\mathbf{s}^{(n+1)} \geq C_2 \mathbf{e}$. Therefore, the standard AIM approximation satisfies the maximum principle. However there is no guarantee that the standard AIM scheme is oscillation-free. In fact, a scheme may satisfy the maximum principle and still produce localized overshoots or undershoots. Hence we propose to analyze the total variation diminishing (TVD) property of the standard AIM scheme.

TVD property in the linear case

In the linear homogeneous case, for an I→E boundary (see figure 16), we have

$$(1 + \lambda)[s_i^{n+1} - s_{i-1}^{n+1}] = \lambda[s_{i-1}^{n+1} - s_{i-2}^{n+1}] + [s_i^n - s_{i-1}^n], \quad i = 1, \dots, p, \quad (57)$$

$$[s_{p+1}^{n+1} - s_p^{n+1}] = (1 - \lambda)[s_{p+1}^n - s_p^n] + \lambda[s_p^{n+1} - s_{p-1}^{n+1}] + \lambda[s_p^{n+1} - s_p^n], \quad (58)$$

$$[s_{p+2}^{n+1} - s_{p+1}^{n+1}] = (1 - \lambda)[s_{p+2}^n - s_{p+1}^n] + \lambda[s_{p+1}^n - s_p^n] - \lambda[s_p^{n+1} - s_p^n], \quad (59)$$

$$[s_i^{n+1} - s_{i-1}^{n+1}] = (1 - \lambda)[s_i^n - s_{i-1}^n] + \lambda[s_{i-1}^n - s_{i-2}^n], \quad i = p + 3, \dots, m, \quad (60)$$

where $\lambda = \frac{\Delta t}{\Delta x} \leq 1$. By manipulating these equations, we can show that

$$\sum_{i=1}^m |s_i^{n+1} - s_{i-1}^{n+1}| \leq \sum_{i=1}^m |s_i^n - s_{i-1}^n|, \quad (61)$$

which means that the scheme is TVD, i.e. $TV(s^{n+1}) \leq TV(s^n)$ (see [31]). The same result is obtained in the case of an E→I boundary.

Figure 17 shows numerical results for the linear advection problem when the initial condition is a jump discontinuity. The standard AIM solution (AIM-STD-UW1) can be compared with the exact solution computed by the Method of Characteristics (MOC), and with the Forward Euler solution (FE-UW1). In the left plot, there is only one I→E boundary moving at a unit speed, thus following the jump discontinuity. As expected from the above results, the numerical solution remains monotonic. In the right plot, every other block is implicit, i.e. there is an I-E boundary at each cell interface. Even in this situation, the TVD property is preserved.

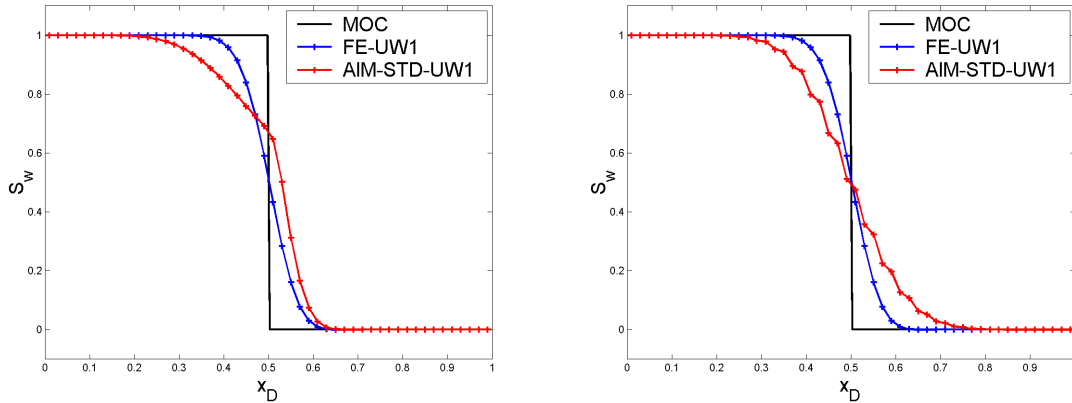


Figure 17: Linear homogeneous case with a jump discontinuity

TVD property in the quasi-linear case

Here we consider the more general case where f is a nonlinear function of s , but for simplicity we assume that $f' \geq 0$. As required, every explicit block satisfies the classical CFL condition:

$$\max_{s \in [s_{i-1}^n, s_i^n]} |f'(s)| \frac{\Delta t}{\Delta x} \leq 1. \quad (62)$$

First we can show that the standard AIM discretization is always TVD across an E→I boundary. The proof relies on the fact that the numerical speed of propagation in the explicit region is greater than the physical speed, as implied by (62). Therefore the mass accumulation over one time step in the first implicit block is limited by the positive or negative mass difference with the upstream block.

In the case of an I→E boundary, the standard AIM is generally not TVD. However we can show that the TVD property is maintained under the following restriction in the last implicit block:

$$\max_{s \in [s_p^n, s_p^{n+1}]} |f'(s)| \frac{\Delta t}{\Delta x} \leq 1. \quad (63)$$

This additional condition comes from the fact that the incoming flux for the first explicit block is calculated implicitly. But it cannot be verified a priori since the value of s_p^{n+1} is unknown.

Figure 18 shows a simulation of the Buckley-Leverett problem where (63) is not satisfied, resulting in oscillatory behavior. The red curves in the right plot correspond to the numerical solution at different time steps. Oscillations appear near the leading edge, due to the transition from an implicit region to an explicit region. These oscillations are damped by the numerical diffusion but new overshoots appear at each time step. Therefore the oscillations move with the saturation front while remaining bounded. Recalling that the standard AIM discretization is locally conservative, we can simply interpret this phenomenon in terms of mass conservation. Indeed the mass flowing through the I→E boundary at the leading edge is entirely accumulated in the first explicit block because the outgoing flux from this block is almost zero. Hence for a large enough time step, there can be a significant overshoot in this block.

In practice, the oscillatory behavior can be avoided by using the maximum speed everywhere, i.e., $\max_{[0,1]} |f'(s)|$, to determine which blocks should be explicit. But this approach does not take full advantage of AIM because many blocks are solved implicitly, although they could be treated explicitly. Another option is to enforce the maximum saturation change below a fixed threshold, but this limits the time step size. The best option is to evaluate the local gradients everywhere in order to avoid the presence of an I-E boundary in a steep region.

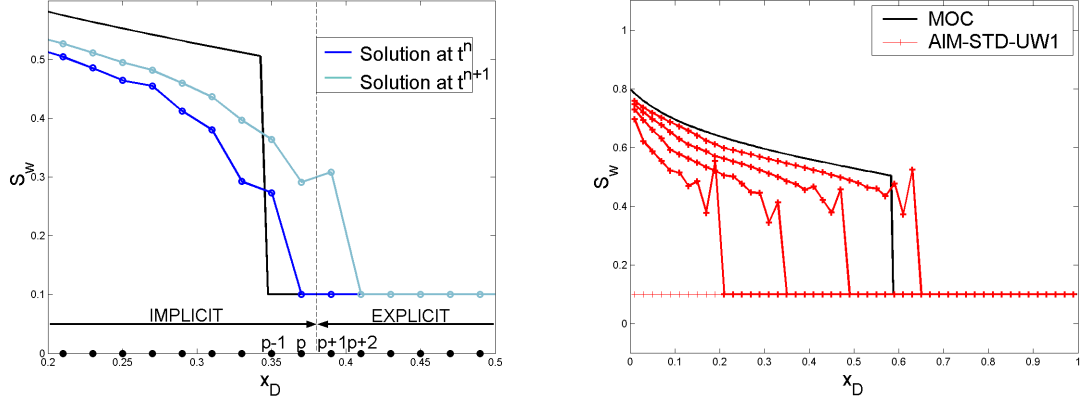


Figure 18: Quasi-linear homogeneous case with discontinuity

In the heterogeneous case, the classical CFL condition becomes

$$\max_{s \in [s_{i-1}^n, s_i^n]} |f'(s)| \frac{\Delta t}{\phi_i \Delta x} \leq 1, \quad (64)$$

where ϕ_i is the porosity in the i -th block. The TVD property across an I→E boundary is now guaranteed under the restriction:

$$\max_{s \in [s_p^n, s_{p+1}^{n+1}]} |f'(s)| \frac{\Delta t}{\phi_{p+1} \Delta x} \leq 1, \quad (65)$$

where $p + 1$ is the index of the first explicit block. In presence of heterogeneities, oscillations are more likely to occur because the number of I-E boundaries generally increases, and the saturation can change more rapidly in a block with low porosity.

Figure 19 shows the simulation of a Buckley-Leverett problem for a heterogeneous case using the standard AIM scheme. Here the porosity values were randomly sampled from a lognormal distribution (see left plot), and the reference solution was calculated on a fine grid. In this case, we observe a large overshoot at the leading edge.

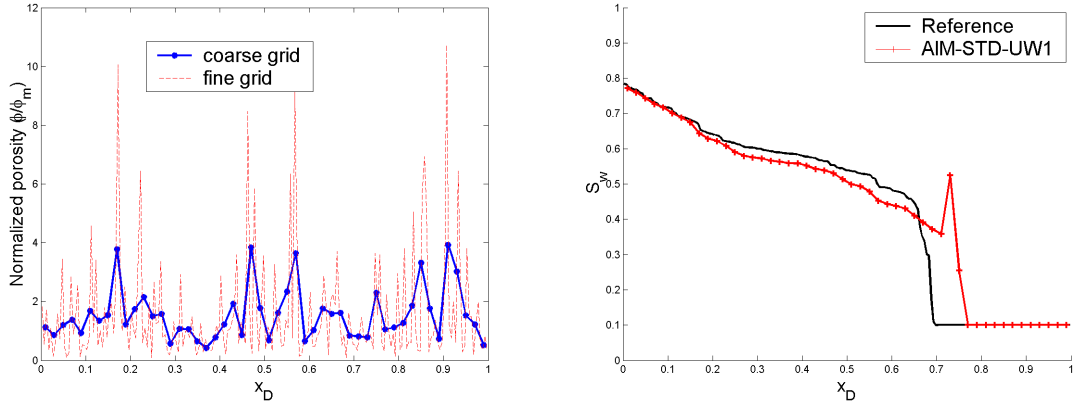


Figure 19: Quasi-linear heterogeneous case with discontinuity

Construction of high-order AIM

Requirements and methodology

Our objective is to construct a class of adaptive implicit methods that satisfies the following requirements:

- High-order accuracy both in time and space.
- Unconditional stability in the implicit regions.
- Local mass conservation.

In the above list, there is no requirement regarding the monotonicity properties of the method, but this point will be discussed further in this section.

To construct a high-order AIM discretization, we use the highly accurate numerical schemes formulated in the Method of Lines (MOL) framework (see [32] and [33]). The choice of the MOL approach is justified by many practical reasons (e.g., multi-dimensional extensions, treatment of diffusive and reactive terms), and the necessity to have a locally conservative scheme. High-order MOL schemes are derived by combining a high-resolution spatial discretization with a highly accurate time integration method. As an initial step, a prototype program was written to test various combinations of space-time discretization schemes. Classical time integration methods are listed below:

- Central and Trapezoidal rules with a Runge Kutta scheme (CRK2 and TRK2).
- Second-order Implicit Runge-Kutta scheme (IRK2).
- Third-order Diagonally Implicit Runge-Kutta scheme (DIRK3).

The common flux discretization strategies (see [34], [35], [36], [37], [38]) include:

- Second-order flux limiting scheme (FL2),
- Second-order central scheme (CS2),
- High-order ENO and WENO schemes (e.g. WENO2).

In a high-order AIM formulation, implicit and explicit time integration methods must be combined consistently. Otherwise, the inconsistencies at the various I/E boundaries would lead to first-order errors. Thus, we propose using a high-order implicit method as the framework for both implicit and explicit regions. The idea is to use a predicted value at the explicit nodes, whenever an implicit value is normally required.

AIM with high-order spatial accuracy

Given a high-order numerical flux $F_{i+\frac{1}{2}}$, we define the following AIM scheme:

$$\begin{aligned} s_i^{n+1} &= s_i^n - \frac{\Delta t}{\Delta x} \left(F_{i+\frac{1}{2}}^{n*} - F_{i-\frac{1}{2}}^{n*} \right) \\ F_{i+\frac{1}{2}}^{n*} &= F_{i+\frac{1}{2}}(s^{n*}), \quad s_i^{n*} = \begin{cases} s_i^{n+1} & \text{if } (i) \text{ implicit} \\ s_i^n & \text{otherwise.} \end{cases} \end{aligned} \quad (66)$$

This scheme can be seen as an extension of the standard AIM because the time integration methods in the explicit and implicit regions correspond to Forward and Backward Euler. Alternatively, we propose the following AIM scheme:

$$\begin{aligned} s_i^{n+1} &= s_i^n - \frac{\Delta t}{\Delta x} \left[\tilde{F}_{i+\frac{1}{2}}^{n+1} - \tilde{F}_{i-\frac{1}{2}}^{n+1} \right] \\ \tilde{F}_{i+\frac{1}{2}}^{n+1} &= F_{i+\frac{1}{2}}(\tilde{s}^{n+1}), \quad \tilde{s}_i^{n+1} = \begin{cases} s_i^{n+1} & \text{if } (i) \text{ implicit} \\ s_i^* & \text{otherwise.} \end{cases} \end{aligned} \quad (67)$$

Here s_i^* is an explicit predictor of s_i^{n+1} that is at least first-order accurate, e.g.

$$s_i^* = s_i^n - \frac{\Delta t}{\Delta x} (F_{i+\frac{1}{2}}^n - F_{i-\frac{1}{2}}^n). \quad (68)$$

The scheme (67) can be seen as an adaptive implicit version of the Backward Euler method in the sense that the fluxes are always evaluated at the new time level.

Figure 20 shows numerical solutions of a 1D Buckley-Leverett problem calculated with the AIM-STD-FL2 and AIM-BE-FL2 schemes, which correspond respectively to (66) and (67), where $F_{i+\frac{1}{2}}$ is given by the second-order accurate flux limiting scheme. Both methods give slightly more accurate results than the standard AIM scheme, AIM-STD-UW1. The gain in resolution is quite small because the time integration

remains first-order accurate. On the other hand, these methods are still unconditionally TVD in the implicit regions. As opposed to the AIM-STD-FL2 scheme, the AIM-BE-FL2 scheme is consistent at the I-E boundaries, and therefore the solution profile (in red) has no “kink”. This is a clear advantage of AIM-BE over AIM-STD; however, the CFL criterion in the explicit region is more restrictive.

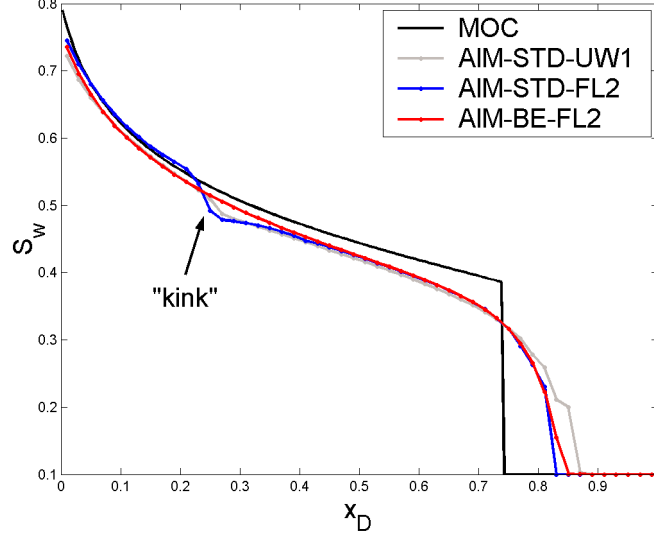


Figure 20: Simulation with AIM-STD-FL2 and AIM-BE-FL2 schemes

Fully high-order AIM

In order to meet all the requirements listed in 2.1, we need to apply a high-order time integration. To illustrate the construction of fully high-order AIM, we introduce below an AIM scheme based on the trapezoidal rule (AIM-TRK2):

$$\begin{aligned}
 s_i^{n+1} &= s_i^n - \frac{\Delta t}{2\Delta x} \left[F_{i+\frac{1}{2}}^n - F_{i-\frac{1}{2}}^n \right] - \frac{\Delta t}{2\Delta x} \left[\tilde{F}_{i+\frac{1}{2}}^{n+1} - \tilde{F}_{i-\frac{1}{2}}^{n+1} \right] \\
 \tilde{F}_{i+\frac{1}{2}}^{n+1} &= F_{i+\frac{1}{2}}^n(\tilde{s}^{n+1}), \quad \tilde{s}_i^{n+1} = \begin{cases} s_{i+\frac{1}{2}}^{n+1} & \text{if } (i) \text{ implicit} \\ s_i^* & \text{otherwise.} \end{cases}
 \end{aligned} \tag{69}$$

By construction, the time integration in the implicit regions corresponds to the implicit trapezoidal rule. Moreover, if we use the predictor (68), the time integration in the explicit regions corresponds to the explicit trapezoidal rule. Finally, we can show from Taylor series expansions that this scheme is first-order accurate (i.e. consistent) at the I-E boundaries. In general this order reduction occurs only locally, so the scheme (69) is globally second-order accurate.

Similarly, we can derive an AIM scheme based on the midpoint rule (AIM-CRK2):

$$\begin{aligned}
s_i^{n+1} &= s_i^n - \frac{\Delta t}{\Delta x} \left[\tilde{F}_{i+\frac{1}{2}}^{n+1/2} - \tilde{F}_{i-\frac{1}{2}}^{n+1/2} \right] \\
\tilde{F}_{i+\frac{1}{2}}^{n+1/2} &= F_{i+\frac{1}{2}}(\tilde{\mathbf{s}}^{n+1/2}), \quad \tilde{s}_i^{n+1/2} = \begin{cases} \frac{1}{2}(s_i^n + s_i^{n+1}) & \text{if } (i) \text{ implicit} \\ \frac{1}{2}(s_i^n + s_i^*) & \text{otherwise.} \end{cases}
\end{aligned} \tag{70}$$

Applying the predictor (68), we can see that the time integration method in the explicit regions corresponds to the explicit midpoint rule. As a result, this scheme is also globally second-order accurate.

The same approach can be used to derive higher order AIM schemes. Below we give the general formulation of a third-order AIM scheme based on the DIRK3 method with $\gamma = 1/2 + \sqrt{3}/6$ (AIM-DIRK3):

$$\begin{aligned}
s_i^{n+1} &= s_i^n - \frac{\Delta t}{2\Delta x} \left(F_{i+\frac{1}{2}}^{(1)} - F_{i-\frac{1}{2}}^{(1)} \right) - \frac{\Delta t}{2\Delta x} \left(F_{i+\frac{1}{2}}^{(2)} - F_{i-\frac{1}{2}}^{(2)} \right) \\
s_i^{(1)} &= s_i^n - \gamma \frac{\Delta t}{\Delta x} \left(\tilde{F}_{i+\frac{1}{2}}^{(1)} - \tilde{F}_{i-\frac{1}{2}}^{(1)} \right) \\
s_i^{(2)} &= s_i^n - (1 - 2\gamma) \frac{\Delta t}{\Delta x} \left(F_{i+\frac{1}{2}}^{(1)} - F_{i-\frac{1}{2}}^{(1)} \right) - \gamma \frac{\Delta t}{\Delta x} \left(\tilde{F}_{i+\frac{1}{2}}^{(2)} - \tilde{F}_{i-\frac{1}{2}}^{(2)} \right)
\end{aligned} \tag{71}$$

where

$$\tilde{F}_{i+\frac{1}{2}}^{(1)} = F_{i+\frac{1}{2}}(\tilde{\mathbf{s}}^{(1)}), \quad \tilde{s}_i^{(1)} = \begin{cases} s_i^{(1)} & \text{if } (i) \text{ implicit} \\ s_i^{*,(1)} & \text{otherwise,} \end{cases} \tag{72}$$

and a similar definition holds for $\tilde{F}_{i+\frac{1}{2}}^{(2)}$. Here we need to apply a third-order numerical flux, such as ENO3. In this case, the explicit predictors $s^{*,(1)}$, $s^{*,(2)}$ should correspond to the times $t^{(1)} = t^n + \gamma\Delta t$ and $t^{(2)} = t^n + (1 - \gamma)\Delta t$.

The high-order AIM schemes presented above require the following three-step approach:

- 1) Apply a predictor step in the explicit blocks,
- 2) Assemble and solve the system for the implicit blocks,
- 3) Update the solution in the explicit blocks.

In terms of computational cost, steps 1 and 3 are cheap, whereas step 2 is generally expensive because it requires solving a system of nonlinear equations. For this purpose we can apply the Newton-Raphson method. Note that there are mainly two factors that explain the additional computational cost of high-order AIM compared to standard AIM. First, the high-order time integration method may require solving several

systems of nonlinear equations in a given time step (e.g. in DIRK3), or solving a larger system if the sub-steps of the time integration are coupled (e.g. in IRK2). Secondly, for each Newton step, the Jacobian has a larger band width than in the first-order case. Indeed, high-order spatial discretizations lead to larger numerical stencils, especially for multi-dimensional problems.

Numerical tests in 1D and 2D

1D Buckley-Leverett problem Figure 21 shows two numerical solutions computed with the second-order accurate AIM-CRK2-WENO2 scheme. The left plot corresponds to $CFL < 2$, while the right plot was obtained for $CFL > 2$. In the first case, the numerical solution is very accurate even near the leading edge, and there is no kink at the I-E boundaries. However, for $CFL > 2$ we observe localized overshoots just ahead of the saturation front. This result is expected, since the implicit trapezoidal rule is known to become oscillatory above this time step threshold.

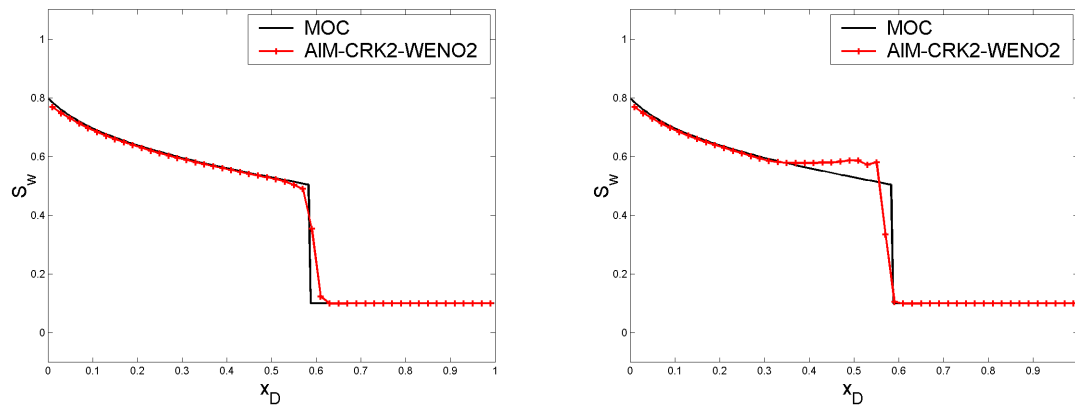


Figure 21: AIM-TRK2-WENO2 solutions for $CFL=1.5$ (left), 2.5 (right)

2D miscible flow in a quarter-five spot Figure 22 shows a reference solution computed on a 50×50 grid using the forward Euler scheme. The left contour plot represents the pressure solution and the right contour plot the concentration profile calculated at $T_f = 2 \times 10^6$ s. For this simulation, the injection rate is $q^w = 10^{-3}$ m³/s, the length of the square is $L = 100$ m, the reservoir depth $h = 1$ m, the viscosity $\mu = 1$ cp, the porosity $\phi = 0.3$, and the permeability tensor is diagonal with $k_x = k_y = 100$ md. The final time corresponds to $2/3$ pore volumes injected.

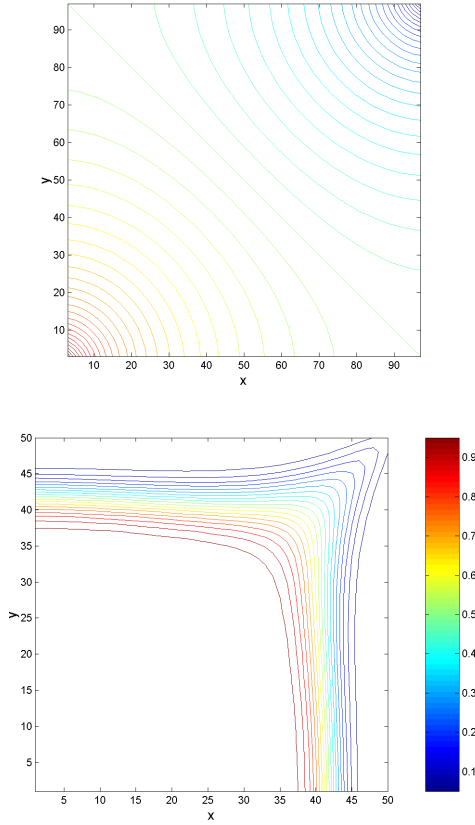


Figure 22: Reference solution of the miscible flow problem in a five-spot pattern

Figure 23 below shows the same simulation on a 25×25 grid, using the second-order accurate AIM-TRK2-WENO2 scheme. The left plot represents the distribution of the implicit blocks (in black) once the maximum time step is reached, which corresponds here to a maximum CFL number around 3. The choice of the explicit blocks was based on the local CFL criterion:

$$\left(\frac{u_{i+\frac{1}{2},j}}{\phi \Delta x} + \frac{v_{i,j+\frac{1}{2}}}{\phi \Delta y} \right) \Delta t \leq \gamma, \quad (73)$$

where γ is a threshold value less than 1. Meanwhile, the right plot shows the contour lines of the concentration profile computed at the final time. Although the theoretical positivity limit is exceeded, there are no visible overshoots or undershoots.

Our AIM-TRK2 method is more efficient than the implicit trapezoidal rule because the number of unknowns is considerably reduced, while the time step restriction for positivity is the same and the second-order accuracy is maintained. It can also be slightly more efficient than the explicit trapezoidal rule, especially if the number of implicit blocks is low. Then there is only a small additional cost for solving implicitly the near-wellbore regions, and the maximum time step size can be at least doubled while maintaining second-order accuracy. To increase the efficiency compared to second-order explicit methods, we need a weaker positivity restriction in the implicit

regions. This can be achieved with other implicit methods such as IRK2 or DIRK3, or as shown later, by applying artificial viscosity.

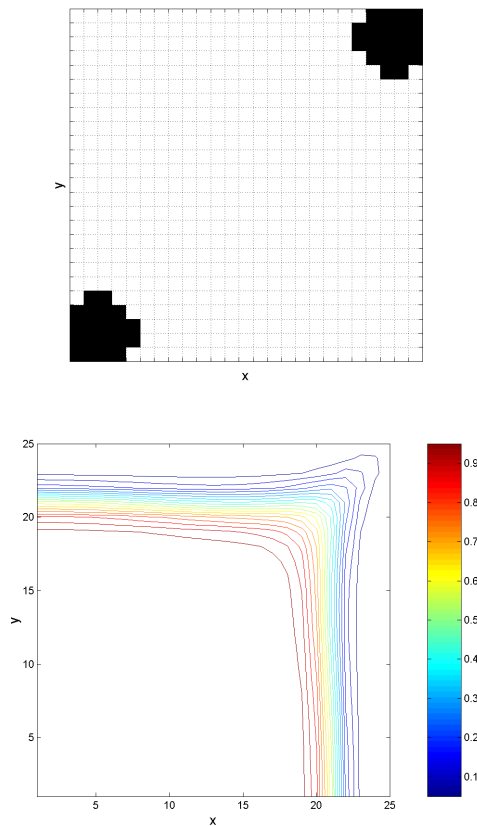


Figure 23: Miscible flow solution using the AIM-TRK2-WENO2 scheme

2D Buckley-Leverett problem with gravity Here we consider a 2D immiscible, incompressible flow in a homogeneous porous medium, with gravity effects along the vertical y -axis. Capillary effects are neglected and it is assumed that a constant and uniform velocity field is imposed along the direction $\theta = \pi/4$. The initial saturation is a circular plume (i.e. $s = 1$ inside a circle, $s = 0$ outside). The flux functions f and g correspond to the fractional flow curves in the x and y directions. These curves are given in the left plot of figure 24. The gravity effect in the y direction translates into a local minimum on the g function curve. In the right plot, we present a reference solution that was computed explicitly on a 70×70 grid, with a gravity number and a mobility ratio given by $G = 5$ and $M = 1$. In the y -direction we used the second-order WENO2 scheme with local flux splitting in order to account for varying local flow directions.

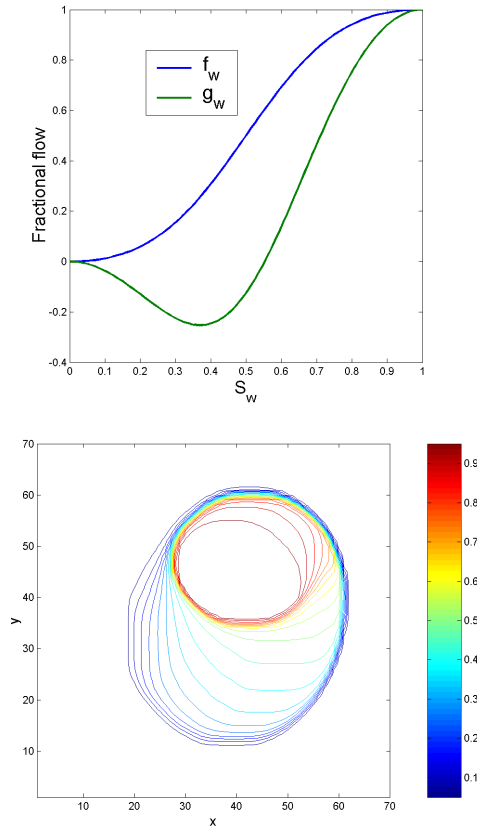


Figure 24: Fractional flow curves (left) and reference solution (right)

Figure 25 below shows simulation results obtained with the AIM-TRK2-WENO2 scheme. The parameters are identical to those of the reference solution, except for the grid size which is only 35×35 . In addition, the maximum time step size was chosen to be four times larger than in the explicit case. Since the grid size was divided by two in both directions, it means that the maximum CFL number is twice as large. The left plot represents the distribution of implicit blocks (in black) during the last time step. In the right plot, we show the contour lines of the saturation profile at the final time. It compares fairly well with the reference solution. Like in the miscible problem, the AIM-TRK2 scheme is quite efficient for this 2D problem because the number of implicit blocks remains small.

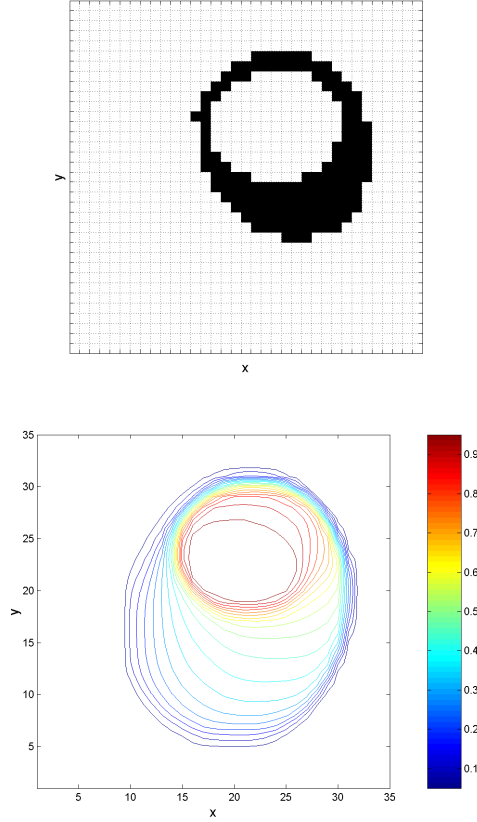


Figure 25: Immiscible flow solution using the AIM-TRK2-WENO2 scheme

High-order AIM with artificial viscosity

The artificial viscosity method is a general approach that helps prevent the creation of spurious oscillations. It was first introduced by Richtmeyer and Von Neumann and it is still widely used today in the CFD community (see [39]). The idea is to introduce a viscous term in specific regions, e.g., near a shock wave or near a steep gradient, where the oscillatory behavior is likely to occur. Meanwhile, the propagation speed must be conserved and the spatial extension of the discontinuity is required to remain on the order of a few grid blocks at all times. Applied to (46) this approach leads to

$$\frac{\partial s}{\partial t} + \frac{\partial f(s)}{\partial x} = \nu_0 \Delta x \frac{\partial}{\partial x} \left(Q(s) \frac{\partial s}{\partial x} \right), \quad (74)$$

where $Q(s)$ is a viscous coefficient which is nonzero only in non-smooth regions. On the discrete level we modify the numerical flux wherever it applies, as follows:

$$\tilde{F}_{i+\frac{1}{2}} = F_{i+\frac{1}{2}} - q_{i+\frac{1}{2}}. \quad (75)$$

Here $q_{i+\frac{1}{2}}$ is an artificial diffusive flux that depends on the function $Q(s)$. From (75)

all the artificial diffusive terms cancel out, hence the scheme remains conservative. Different diffusive terms can be applied, for instance:

- $Q(s) = 1$, $q_{i+\frac{1}{2}} = \nu_0(s_{i+1} - s_i)$,
- $Q(s) = f'(s)$, $q_{i+\frac{1}{2}} = \nu_0(f_{i+1} - f_i)$,
- $Q(s) = [f'(s)]^2$, $q_{i+\frac{1}{2}} = \nu_0(f'_{i+\frac{1}{2}})^2(s_{i+1} - s_i)$.

The second choice should be applied only if $f' \geq 0$. Then we can easily check that it has the desired diffusive effect. In particular the diffusivity increases in the high speed regions where oscillations are likely to occur.

In figure 26, we show simulation results for the CRK2-WENO2 scheme applied with a CFL number close to 3. In the case without artificial diffusion, we observe a non-monotonic behavior near the leading edge due to the violation of the monotonicity restriction given by $CFL < 2$. By adding the right amount of artificial viscosity (here $\nu_0 = 0.4$), we overcome this nonphysical behavior and we obtain a very satisfactory resolution near the shock.

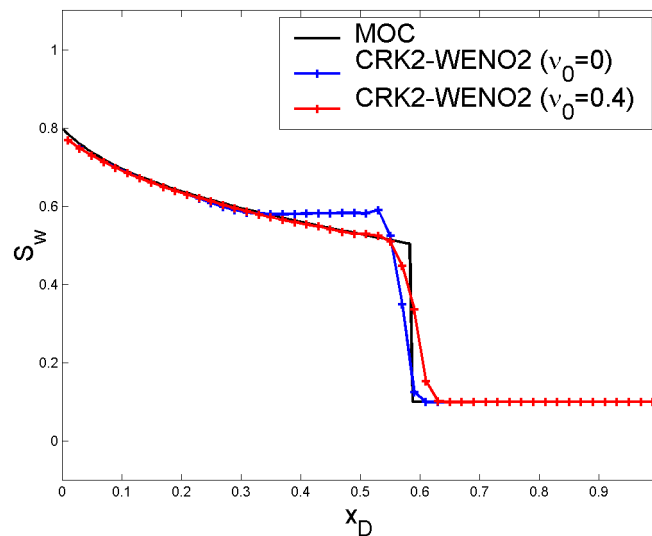


Figure 26: Simulation result using the artificial viscosity method

Remarks and Future Plans

Analysis of the standard AIM formulation revealed a local inconsistency at the I-E boundaries. But the discretization errors are only of the order of the numerical dispersion. So in general we only observe small “kinks” in the solution profile. Moreover, we showed that the monotonicity properties of the solution are preserved, except in specific situations that can be avoided in practice.

Our construction of high-order AIM schemes relies on highly accurate MOL schemes. By using explicit predictors, the time integration in the explicit regions can be based on the same time levels as in the implicit regions. Hence the consistency at the I-E boundaries and the locally conservative form are maintained. Numerical experiments comparing standard AIM with high-order AIM indicate a substantial reduction of the numerical dispersion. However, the high-order implicit time integration leads to a severe positivity restriction on the time step size. In fact, unconditionally positive methods can only be first-order accurate (see [40], [41]). Therefore, we propose to apply artificial viscosity in the implicit regions in order to remove the spurious oscillations at large CFL numbers. We also need to investigate further what optimal time integration method (with respect to positivity) should be employed. Finally, the most robust approach for a wide range of practical applications consists of applying the Backward-Euler method in the implicit regions and a high-order time integration method in the explicit regions. This will be validated using examples of practical interest.

Adaptive Operator Based Multiscale Method for Compressible Multiphase Flow

Investigators

Hamdi Tchelepi, Associate Professor of Energy Resources Engineering; Hui Zhou, Graduate Research Assistant

Introduction

The accuracy of simulating flow and transport in natural formations depends on the quality and resolution of the reservoir description model. Formation properties, such as porosity and permeability, typically vary over many scales. As a result, it is not unusual for a detailed geologic description to have $O(10^7) - O(10^8)$ gridblocks. However, this level of resolution is far beyond the computational capability of existing numerical simulators. Thus, it is necessary to have an efficient and accurate computational method to study these highly detailed models.

The multiscale finite-volume approach is very promising due to its ability to resolve fine-scale information accurately without direct solution of the global fine-scale equations. In order to describe flow and transport of CO_2 in geologic formations, we need to be able to model compressible multiphase flow in large-scale heterogeneous porous media. Existing multiscale methods ([42, 43, 44, 45, 46]), however, deal with the incompressible (elliptic) flow problem only. Here, we extend the multiscale finite-volume method to compressible multiphase flow. The accuracy of Operator Based Multiscale Method is demonstrated using several challenging cases, including highly compressible multiphase flow in a strongly heterogeneous permeability field (SPE 10).

Background

Flow and transport in natural porous formations can be quite complex, and often reflect the intrinsic multiscale character of the geologic formation. This makes the problem of modeling nonlinear flows in heterogeneous porous media a natural target for multiscale mathematical formulations and solution methods. For example, Hou and Wu [43] proposed a multiscale finite-element method (MsFEM) that captures the fine-scale information by constructing special local basis functions. The method proved to be quite accurate except that the reconstructed fine-scale velocity field was not locally conservative. Later, Chen and Hou proposed a locally conservative mixed finite-element multiscale method. Another multiscale mixed finite-element method has been presented by Arbogast[45] and Arbogast and Bryant [46], where numerical Green functions are used to resolve the fine-scale information. The Green functions

are then coupled with coarse-scale operators to obtain the global solution. These methods considered incompressible flow in heterogeneous porous media, where the flow equation is elliptic. A multiscale finite-volume method (MsFVM) was proposed by Jenny, Lee and Tchelepi [42] for heterogeneous elliptic problems. They employed two sets of basis functions – dual and primal. The dual basis functions are identical to those of Hou and Wu[43], while the primal basis functions are obtained by solving local elliptic equations with Neumann boundary conditions calculated from the dual basis functions.

Existing multiscale methods ([42, 43, 44, 45, 46]) deal with the incompressible flow problem only. However, compressibility will be significant if a gas phase is present. Gas has a large compressibility, which is usually a strong function of pressure. Therefore, there can be significant spatial compressibility variations in the formation, and this is a challenge for multiscale modeling. Very recently, Lunati and Jenny considered compressible multiphase flow[47] in the framework of MsFVM. They proposed three different approaches based on the relative importance of compressibility. In their framework, they retained the elliptic construction of the basis functions in order to minimize the need for frequent updating of the basis, and they represented the compressibility effects on the coarse-scale.

Motivated to construct a multiscale finite-volume framework that can deal with compressible multiphase flow in highly detailed heterogeneous formations, we developed an Operator Based Multiscale Method (OBMM), that is adaptive and extensible. The OBMM algorithm is composed of four steps: (1) constructing the prolongation and restriction operators, (2) assembling and solving the coarse-scale pressure equations, (3) reconstructing the fine-scale pressure and velocity fields, and (4) solving the fine-scale transport equations. OBMM is a general algebraic multiscale framework for compressible multiphase flow in heterogeneous reservoirs. This algebraic framework can also be extended naturally from structured to unstructured grids. Moreover, the OBMM approach may be used to employ multiscale solution strategies in existing simulators with a relatively small investment.

Results

A general algebraic multiscale framework for compressible multiphase flow in heterogeneous formation was developed. To deal efficiently and accurately with the nonlinear coupling of flow and transport, we designed a multiscale algorithm that ensures consistency and local conservation of the computations on the fine scale. We also report on the initial results of a multiscale formulation for the nonlinear transport problem (i.e., solving the saturation equations). Adaptive computations are employed to maximize the efficacy of the overall multiscale algorithm.

Operator Based Multiscale Method (OBMM)

First, we describe the operator based multiscale method (OBMM) for the two-phase flow problem. We show that for incompressible flow, OBMM is identical to the original MsFVM[42] with specific forms of the prolongation and restrictions operators. Compressibility effects are reflected in the coarse-scale operators.

Moreover, the basis functions and the reconstructed fine-scale fluxes also contain compressibility effects.

Governing Equations. We consider immiscible two-phase flow in porous media. Gravity and capillarity are neglected here. The governing equations are the mass conservation equations of the two phases,

$$\begin{aligned}\frac{\partial(\phi b_l)}{\partial t} + \nabla \cdot (b_l u_l) &= q_l, \\ u_l &= -\lambda_l \nabla p, \\ \lambda_l &= \frac{k k_{r_l} b_l}{\mu},\end{aligned}\tag{76}$$

where $l = 1, 2$ denotes the two phases; b_l is the inverse of the phase formation volume factor, which is defined as the ratio of density at reservoir conditions to density at standard conditions; u_l is the phase volumetric flux at reservoir condition; q_l is the source term; λ_l is the phase mobility; k_{r_l} is the phase relative permeability; ϕ and k are the porosity and absolute permeability of porous medium.

Because multiscale methods are usually applied only to the flow problem (pressure equation), the flow and transport problems are treated differently. Thus, the flow and transport equations are solved sequentially using either an IMPES (IMPlicit Pressure EXplicit Saturation)[48], or a sequential implicit (SI) [49] method. Here we adopt the sequential implicit approach. The linearized discrete pressure equation can be obtained from Eq.76 through simple algebraic manipulation. The semi-discrete equation for iteration $\nu + 1$ at time step $n + 1$ is

$$C \frac{p^{\nu+1} - p^\nu}{\Delta t} - \alpha_1^\nu \nabla \cdot (b_1^\nu \lambda_1^\nu \nabla p^{\nu+1}) - \alpha_2^\nu \nabla \cdot (b_2^\nu \lambda_2^\nu \nabla p^{\nu+1}) = Q,\tag{77}$$

where,

$$\begin{aligned}\alpha_1^\nu &= \frac{1}{b_1^\nu}, \quad \alpha_2^\nu = \frac{1}{b_2^\nu}, \\ C &= \left(\frac{\partial \phi}{\partial p} - \phi^n (b_1^n S_1^n \frac{\partial \alpha_1}{\partial p} + b_2^n S_2^n \frac{\partial \alpha_2}{\partial p}) + \Delta t \frac{\partial(\alpha_1 q_1 + \alpha_2 q_2)}{\partial p} \right)^\nu, \\ Q &= -\frac{\phi^\nu}{\Delta t} + \frac{\phi^n}{\Delta t} (\alpha_1^\nu b_1^n S_1^n + \alpha_2^\nu b_2^n S_2^n) - (\alpha_1 q_1^\nu + \alpha_2 q_2^\nu).\end{aligned}\tag{78}$$

Given a fine-scale problem, Eq.77 can be written in matrix form as

$$(\mathbf{T}_f - \mathbf{C}_f) \mathbf{p}_f = \mathbf{r}_f,\tag{79}$$

where \mathbf{T}_f is the fine-scale transmissibility matrix associated with the flow, \mathbf{C}_f is the fine-scale compressibility matrix associated with accumulation, \mathbf{p}_f denotes the fine-scale pressure vector, and \mathbf{r}_f is the fine-scale right-hand-side vector.

The linearized discrete form of the transport equation for phase 1 is

$$\frac{\phi^{\nu+1} b_1^{\nu+1} S_1^{\nu+1} - \phi^n b_1^n S_1^n}{\Delta t} = \nabla \cdot \left\{ \left[b_1^{\nu+1} (f_1^\nu + \frac{\partial f_1}{\partial S_1} \Big|^\nu (S_1^{\nu+1} - S_1^\nu)) \right] \mathbf{u}_T^{\nu+1} \right\} - q_1,\tag{80}$$

where f_1 is the fractional flow of phase 1, and \mathbf{u}_T is the total velocity.

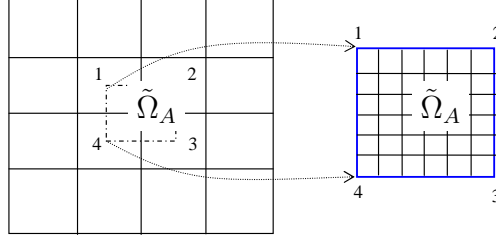


Figure 27: Two-dimensional multiscale grid with a typical dual control-volume. The enlarged dual control-volume shows the underlying fine grid.

Prolongation Operator. The multiscale prolongation operator, \mathcal{P} , is defined as the mapping from coarse-scale pressure to fine-scale pressure, i.e.,

$$\mathbf{p}_f = \mathcal{P}\mathbf{p}_c, \quad (81)$$

where \mathbf{p}_c denotes the cell-center coarse-scale pressure. Hou and Wu [43] used a set of specially constructed basis functions to relate the fine and coarse pressures. Although their study was for the incompressible flow (elliptic) problem, we have found that these basis functions also work for parabolic problems (e.g., compressible flow). The construction of the basis functions for Eq.76 is discussed below.

Consider a two dimensional multiscale grid as shown in Fig.27. The physical domain is partitioned into disjoint coarse blocks (primal coarse blocks), and each coarse block is further partitioned into fine cells. A set of dual coarse blocks is defined by connecting the cell centers of the coarse blocks. The use of a dual-coarse grid is an efficient and flexible tool for constructing accurate and conservative fluxes on the primal coarse grid[42].

A basis function associated with coarse node i ($i = 1, \dots, 4$) in dual block $\tilde{\Omega}_A$ is obtained by solving the elliptic part of Eq.76, namely,

$$\begin{aligned} \alpha_1^\nu \nabla \cdot (b_1^\nu \lambda_1^\nu \nabla \phi_A^i) + \alpha_2^\nu \nabla \cdot (b_2^\nu \lambda_2^\nu \nabla \phi_A^i) &= 0 \quad \text{in } \tilde{\Omega}_A, \\ \alpha_1^\nu \frac{\partial}{\partial x_t} \left(b_1^\nu \lambda_1^\nu \frac{\partial \phi_A^i}{\partial x_j} \right)_t + \alpha_2^\nu \frac{\partial}{\partial x_t} \left(b_2^\nu \lambda_2^\nu \frac{\partial \phi_A^i}{\partial x_j} \right)_t &= 0 \quad \text{on } \partial \tilde{\Omega}_A, \\ \phi_A^i(\mathbf{x}_j) &= \delta_{ij}, \end{aligned} \quad (82)$$

where subscript t denotes the component tangential to the boundary, and j denotes any coarse node in $\tilde{\Omega}_A$ ($j = 1, \dots, 4$). Let K be the global index of a coarse node, $i_{K,A}$ be the local index of node K in dual block $\tilde{\Omega}_A$, and \mathcal{D}_K the set of dual blocks intersected by node K . For Cartesian grid, the number of elements in \mathcal{D}_K is 2^d , where d is the number of dimensions. From a global point of view, a basis function can be written as

$$\phi_K = \sum_{\tilde{\Omega}_A \in \mathcal{D}_K} \phi_A^{i_{K,A}}. \quad (83)$$

The multiscale prolongation operator, \mathcal{P} , is an $n \times N$ matrix, where n is the number of global fine cells and N is the number of global coarse cells. Let k denote a fine cell and K a coarse cell. Then one has

$$\mathcal{P}_{k,K} = \phi_K(\mathbf{x}_k). \quad (84)$$

Restriction Operator. Substitution of Eq.81 into Eq.79 leads to

$$(\mathbf{T}_f - \mathbf{C}_f)\mathcal{P}\mathbf{p}_c = \mathbf{r}_f. \quad (85)$$

The significance of Eq.85 is that its unknowns are coarse-scale pressures. We need to apply a restriction operator, \mathcal{R} , that provides a mapping from fine to coarse space. So we write

$$\mathcal{R}(\mathbf{T}_f - \mathbf{C}_f)\mathcal{P}\mathbf{p}_c = \mathcal{R}\mathbf{r}_f, \quad (86)$$

or,

$$(\mathbf{T}_c - \mathbf{C}_c)\mathbf{p}_c = \mathbf{r}_c, \quad (87)$$

where $\mathbf{T}_c, \mathbf{C}_c, \mathbf{r}_c$ are the coarse-scale counterparts of $\mathbf{T}_f, \mathbf{C}_f, \mathbf{r}_f$, and are defined as

$$\begin{aligned} \mathbf{T}_c &= \mathcal{R}\mathbf{T}_f\mathcal{P} \\ \mathbf{C}_c &= \mathcal{R}\mathbf{C}_f\mathcal{P} \\ \mathbf{r}_c &= \mathcal{R}\mathbf{r}_f. \end{aligned} \quad (88)$$

Eq.87 is the coarse-scale equation we need to solve.

The restriction operator, \mathcal{R} , maps the fine-scale discretization equations into the coarse scale. The specific choice for \mathcal{R} depends on the discretization scheme (e.g., finite-element or finite-volume). We denote a fine-scale conservative equation by E . A finite-volume formulation starts with

$$\int_{\Omega_k} E \, dV = 0 \quad (\forall \text{ fine cell } \Omega_k, k = 1, \dots, n). \quad (89)$$

A coarse-scale finite volume formulation requires

$$\int_{\Omega_K} E \, dV = 0 \quad (\forall \text{ coarse block } \Omega_K, K = 1, \dots, N). \quad (90)$$

Comparing Eq.89 and Eq.90, it is clear that Eq.90 can be obtained by summing Eq.89 for all the fine cells inside a coarse block K , i.e.,

$$\int_{\Omega_K} E \, dV = \sum_{\Omega_k \in \Omega_K} \int_{\Omega_k} E \, dV. \quad (91)$$

The summation in Eq.91 can be represented as a restriction operator, \mathcal{R} , as follows

$$\mathcal{R}_{K,k} = \begin{cases} 1 & \text{if } \Omega_k \subset \Omega_K \\ 0 & \text{otherwise} \end{cases} \quad (K = 1, \dots, N; k = 1, \dots, n). \quad (92)$$

It is important to note that the restriction operator does not depend on the detailed discretization scheme (i.e., backward difference or central difference, etc.) and thus is general for a given formulation. For a Galerkin-type finite element method, the coarse-scale equation may be written as

$$\int_{\Omega_K} \phi_M E \, dV = 0 \quad (K, M = 1, \dots, N), \quad (93)$$

and one can show that \mathcal{R} takes the following form

$$\mathcal{R} = \mathcal{P}^T. \quad (94)$$

Zhou[50] provides a detailed treatment for finite-element based multiscale formulations.

Coarse-Scale Operators. Given the prolongation and restriction operators defined above, the coarse-scale system, Eq.87, can be constructed. We try to shed some light on the physical meaning of the coarse-scale operator. The focus is on OBMM using the finite-volume formulation (i.e., \mathcal{R} given by Eq.92).

To make the analysis easier, consider a one-dimensional problem. Fig.28 shows a grid with coarse blocks $K - 1, K, K + 1$, and fine cells $k - 4, \dots, k + 4$. We first look

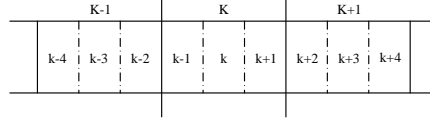


Figure 28: One-dimensional multiscale grid

at the incompressible case. Here, Eq.76 becomes

$$\nabla \cdot (\lambda_t \nabla p) = q_t, \quad (95)$$

where, $\lambda = \lambda_1 + \lambda_2$ is the total mobility, and q_t is the total source term. Using a central difference scheme for the discretization of the fine-scale problem, the OBMM algorithm results in three non-zero elements for the K^{th} row of the coarse-scale transmissibility matrix, i.e.,

$$\begin{aligned} T_{cK, K-1} &= -\frac{\lambda_{k-3/2}}{\Delta x} (\phi_{K-1}(x_{k-1}) - \phi_{K-1}(x_{k-2})), \\ T_{cK, K} &= -\frac{\lambda_{k-3/2}}{\Delta x} (\phi_K(x_{k-1}) - \phi_K(x_{k-2})) \\ &\quad + \frac{\lambda_{k+3/2}}{\Delta x} (\phi_K(x_{k+2}) - \phi_{K-1}(x_{k+1})), \\ T_{cK, K+1} &= -\frac{\lambda_{k+3/2}}{\Delta x} (\phi_{K+1}(x_{k+2}) - \phi_{K+1}(x_{k+1})). \end{aligned} \quad (96)$$

These coarse-scale equations are exactly the same as the effective coarse-grid transmissibility equations constructed by Jenny et al.[42]. For example, from Eq.96, $T_{cK, K-1}$ is the flux across the interface between coarse blocks $K - 1$ and K due to a unit-pressure at node $K - 1$.

Compressibility is taken into account in the basis functions, Eq.82, and in the coarse-scale transmissibility and compressibility matrices, Eq.88. The fine-scale fluxes represented by \mathbf{T}_f contain compressibility effects, and OBMM gives the coarse-scale fluxes by summing up the fine-scale fluxes in a coarse block. The coarse-scale compressibility matrix in Eq.88 is obtained by redistributing accumulation terms in the coarse grid according to the underlying fine-scale accumulation terms. By construction, the scheme is conservative on both the fine and coarse scales. The coarse-scale pressure, \mathbf{p}_c , is obtained from Eq.87 and then, the so-called dual fine-scale pressure, \mathbf{p}_d , is reconstructed by

$$\mathbf{p}_d = \mathcal{P} \mathbf{p}_c. \quad (97)$$

Coupling Flow and Transport

For multiphase problems, the flow (pressure and total velocity) and transport (saturation) equations are solved in a sequential manner. After reconstruction of the fine-scale pressure field, we can then proceed to solve for saturation equations on the fine scale. Note that special care should be taken to ensure the conservation and consistency of the coupled system.

Fine-scale Velocity. The fine-scale velocity, \mathbf{u}_T , calculated using \mathbf{p}_d may be discontinuous at the interfaces of the dual coarse blocks, since the basis functions ensure flux continuity only in the interior of each dual block. To obtain a conservative fine-scale velocity, we solve the fine-scale Eq.77 locally for each primal coarse block with flux boundary conditions, which are obtained from \mathbf{p}_d . The fine-scale pressure computed in this manner, which we denote as \mathbf{p}_v , is the primal fine-scale pressure. Then, the fine-scale velocity in the interior regions of primal coarse blocks is calculated from \mathbf{p}_v , while the velocity on the boundary of the primal coarse block is calculated from \mathbf{p}_d . The total velocity field obtained this way is locally conservative on the fine and coarse scales.

Multiscale Algorithm for Compressible Multiphase Flow. Notice that Eq.77 is nonlinear, and thus we have to solve it iteratively. However, solving the pressure system is usually more expensive than solving the saturation equations. Thus, we have an outer loop, where we solve for the fine-scale pressure only once using OBMM and then calculate the fine-scale primal pressure and total velocity. On the other hand, the saturation equations are solved iteratively in an inner loop until convergence. The pseudo code for one time step is listed in Fig.29, where n denotes a time step and ν denotes an iteration step. Note that for the finite-volume OBMM, the restriction operator is constructed once as shown by Eq.92. Also note that when solving the saturation equations in the inner loops, the total velocity \mathbf{u}_T is fixed.

Careful updating of the pressure dependent properties is an important part of the overall scheme. We have two fine-scale pressure fields: dual and primal. Since the primal pressure yields a conservative fine-scale velocity field, we calculate the pressure dependent properties based on the primal pressure. Also, to ensure consistency and conservation, the properties in the pressure equation are completely consistent with those in the saturation equation.

Adaptive Multiscale Computation

The computational efficiency of multiscale methods mainly lies in that a large-scale problem is decomposed into small local problems. Thus, a lot of time is saved in the linear solver step. Moreover, multiscale algorithms are well suited for parallel computation, since the local problems can be solved independently. Most importantly, multiscale methods are designed to be adaptive, and this is discussed below.

As described in the previous sections, basis functions are constructed by solving a series of local problems in every dual coarse block. Actually, it is not necessary to update the basis functions in every block and for every iteration. It is obvious that if

```

 $\nu_p = 1; \nu_s = 1; p^{\nu_p} = p^n; S^{\nu_s} = S^n$ 
/* outer loop */
while ( system not converged)
    construct fine-scale operators:  $\mathbf{T}_f, \mathbf{C}_f, \mathbf{r}_f$ ;
    update basis functions:  $\phi_A, A = 1, \dots, N$ ;
    assemble prolongation operator:  $\mathcal{P}$ ;
    calculate coarse-scale operators:  $\mathbf{T}_c, \mathbf{C}_c, \mathbf{r}_c$ ;
    solve for coarse-scale pressure:  $\mathbf{p}_c$ ;
    reconstruct dual fine-scale pressure:  $\mathbf{p}_d$ ;
    reconstruct primal fine-scale pressure:  $\mathbf{p}_v$ ;
     $\nu_p = \nu_p + 1; p^{\nu_p} = p_v$ ;
    update pressure dependent properties based on  $p^{\nu_p}$ 
    calculate fine-scale total velocity  $\mathbf{u}_T$ 
    /* inner loop */
    while (saturation equation not converged)
        solve linearized transport equation for  $S^{\nu_s+1}$ ;
         $\nu_s = \nu_s + 1$ ;
        update saturation dependent properties:  $\lambda = \lambda(S^{\nu_s})$ ;
    end
end
 $n = n + 1$ 

```

Figure 29: The multiscale algorithm for compressible multiphase flow

the property change in a block is small, the pressure changes should also be small. By examining the equations for the basis functions (Eq.82), it appears reasonable to update the basis functions according to the change in the total mobility. Namely, if the condition

$$\frac{1}{1 + \epsilon_\lambda} < \frac{\lambda_t^\nu}{\lambda_t^{\nu-1}} < 1 + \epsilon_\lambda \quad (98)$$

is not satisfied for all fine cells inside a dual coarse block, then the basis functions associated with that dual block should be recomputed. The parameter ϵ_λ is a user defined adaptivity threshold. Note that the total mobility contains contributions due to compressibility. A similar criterion was used for incompressible problems by Jenny et al.[48, 49]. In numerical experiments, taking $\epsilon_\lambda < 0.2$ yields results very close to those without adaptivity, and the fraction of basis function that must be recomputed is usually less than 5%.

The saturation equations are also solved on the fine-scale. Consequently, the fine-scale primal pressure field is needed. Therefore, if we are able to calculate the transport equation in an adaptive manner, a great deal of efficiency can be gained. We are developing a multiscale method with adaptive transport computation. This is ongoing work and preliminary results are very promising.

Numerical Results

The Operator Based Multiscale Method (OBMM) for compressible flow is demonstrated using two-dimensional problems. The permeability field is the top layer

of the SPE 10 model[51]. We modified the original permeability field slightly. The extreme low and high values that account for less than 2.5% are clipped. The variance of the logarithmic permeability of this model is $\sigma_{lnk}^2 = 5.04$ (the original variance is 5.45) as shown in Fig.30. It is still a highly heterogeneous model. The fine-scale grid contains 220×60 gridblocks, and the coarse-scale grid contains 20×12 gridblocks. The upscaling factor is 55 (11×5). The field is initially saturated with phase 2 at a uniform pressure. We then begin to inject pure phase 1 in the upper left coarse block and produce in the lower right coarse block. The production and injection rates are constant in each fine cell within the primal coarse injection and production blocks. Quadratic relative permeability curves are used. The viscosity ratio of the two phases is 1 : 10. The porosity is constant at 0.3.

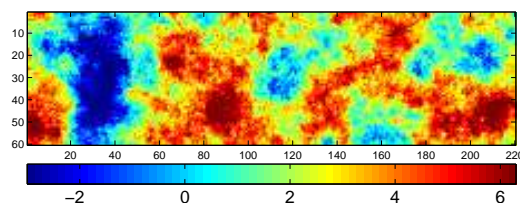


Figure 30: Log-permeability of the top layer of the SPE 10 model

Incompressible Flow. We first show results for incompressible flow. We take solutions obtained using standard fine-scale computations as reference. Then, we compare the reference results with OBMM solutions. Specifically we compare the fine-scale pressure, saturation, and horizontal component of the total-velocity at $t = 0.2$ PVI. Figures 31 and 32 show that the pressure and velocity fields obtained using OBMM are in close agreement with the reference results. Moreover, the fine-scale saturation distribution obtained from OBMM is almost identical to the reference field as shown in Fig.33. Contours of error in the fine-scale saturation are shown in Fig.34, which indicates that the error is concentrated in a few isolated fine cells around the saturation front.

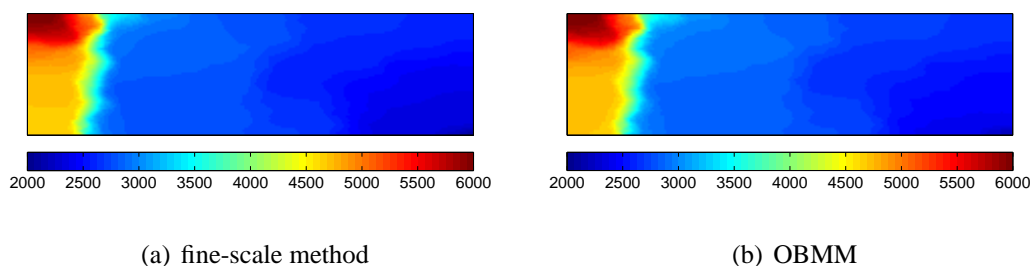


Figure 31: Fine-scale pressure at $t = 0.2$ PVI for the incompressible case

The recovery and the production fractional flow of phase 2 are shown in Fig.35. The excellent agreement with the reference solution suggests that OBMM is very accurate for the incompressible case. This is consistent with the findings reported for the MsFVM[42].

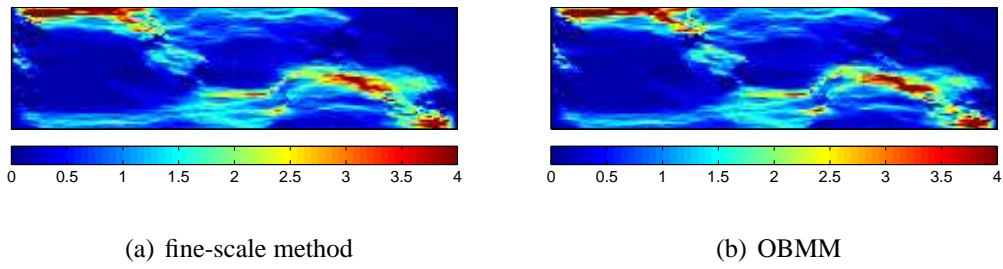


Figure 32: Fine-scale velocity (horizontal component) at $t = 0.2$ PVI for the incompressible case

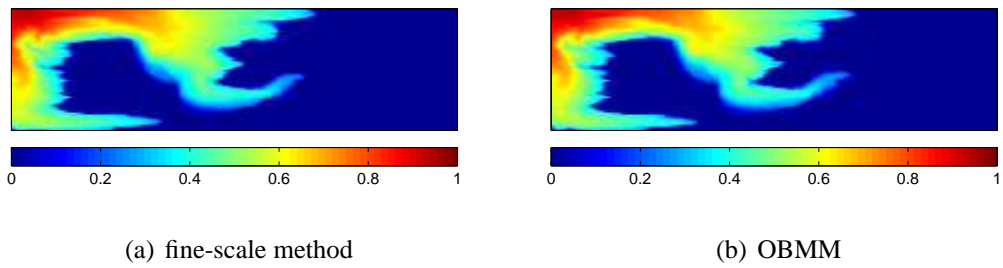


Figure 33: Fine-scale saturation at $t = 0.2$ PVI for the incompressible case

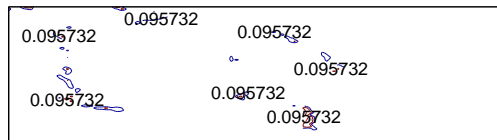


Figure 34: Contours of saturation error at $t = 0.2$ PVI for the incompressible case

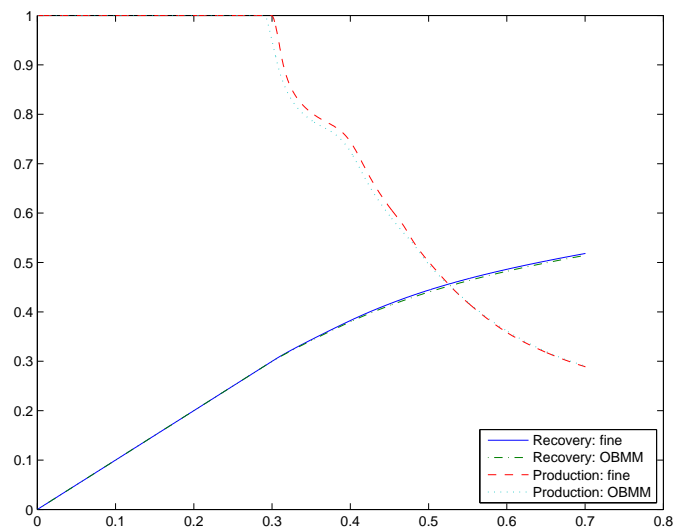


Figure 35: Recovery and production fractional flow of phase 2 for the incompressible case

We report the error statistics and the percentage of basis functions that are recomputed for several time steps in Table II. The pressure error, ϵ_p , and saturation error, ϵ_s , are defined by

$$\begin{aligned}\epsilon_p &= \frac{\|p^{ms} - p^f\|_2}{\|p^f\|_2}, \\ \epsilon_s &= \|S^{ms} - S^f\|_2,\end{aligned}\tag{99}$$

where superscript f and ms , denote, respectively, the reference and OBMM solutions. f_p denotes the percentage of recomputed basis functions. The overall quality of the OBMM solution is quite good. The percentage of recomputed basis functions is very small, which leads to efficient computation of highly detailed models.

Table II: Errors and percentage of the recomputed basis functions in several time steps for the incompressible case

t (PVI)	e_p	e_s	f_p (%)
0.1	2.07e-2	2.21e-4	0.082
0.2	2.77e-2	2.10e-4	0.041
0.5	3.05e-2	2.03e-4	0.033
0.7	3.55e-2	1.94e-4	0.026

Compressible Flow. We consider a highly compressible flow problem. Assume phase 1 is a gas phase satisfying the ideal gas law. Phase 2 is a compressible liquid phase. The PVT properties are given by

$$\begin{aligned}b_1 &= \frac{p}{p_0}, \\ b_2 &= 1 + 10^{-3}(p - p_0),\end{aligned}\tag{100}$$

where p_0 is pressure at standard conditions (14.7 psi).

The OBMM solutions are compared with reference solutions at $t = 0.2$ PVI. From Fig.36, we can see that the pressure variations are large. Thus, we can expect that the effects of compressibility will be very important. For this highly compressible and strongly heterogeneous case, the fine-scale pressure obtained using OBMM is in good agreement with the reference solution. The fine-scale velocity in OBMM is also in excellent agreement with the reference as shown in Fig.37. The saturation solution of OBMM is almost identical to the reference solution as shown in Fig.38. This is confirmed by the fine-scale saturation error contours in Fig.39. The recovery and production fractional flow curves obtained using OBMM and the reference solution are shown in Fig.40, which shows that the results are in close agreement.

Table III reports the pressure and saturation errors as well as the percentage of recomputed basis functions for each time step. The quality of the saturation field using OBMM is excellent, while the pressure solution shows larger errors compared with the incompressible case. Recall that our basis functions are obtained by solving local elliptic problems. In this strongly compressible case, the effects of the parabolic part of the governing equation on the pressure distribution are significant. Thus, the basis

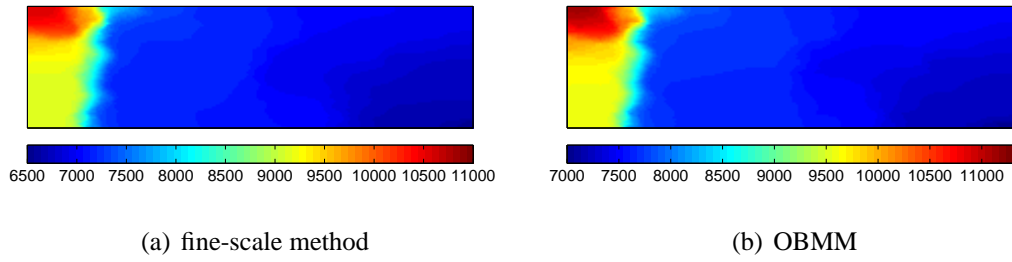


Figure 36: Fine-scale pressure at $t = 0.2$ PVI for the compressible case

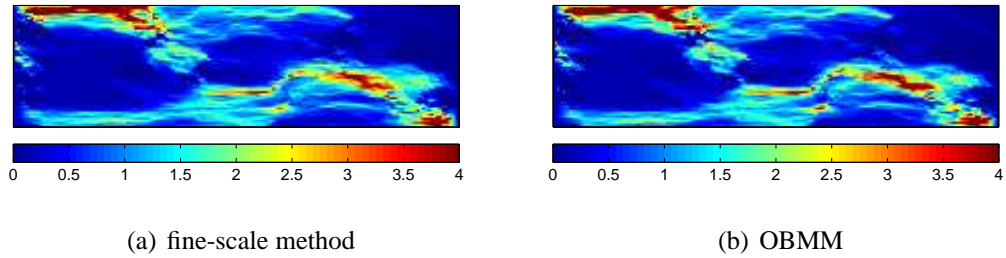


Figure 37: Fine-scale velocity (horizontal component) at $t = 0.2$ PVI for the compressible case

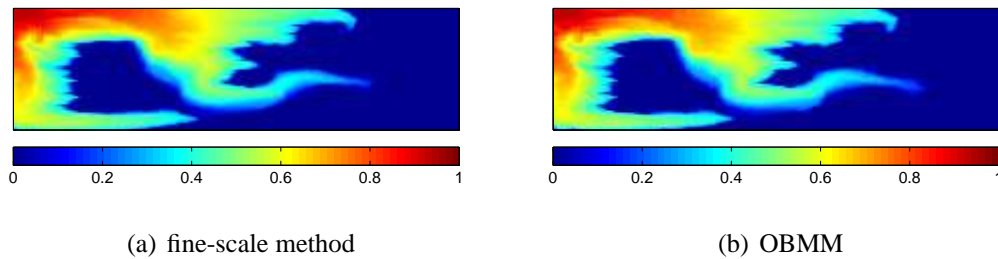


Figure 38: Fine-scale saturation at $t = 0.2$ PVI for the compressible case

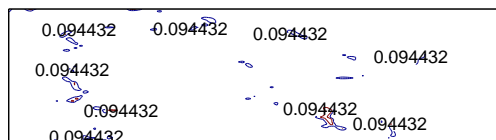


Figure 39: Contours of the saturation error at $t = 0.2$ PVI for the compressible case

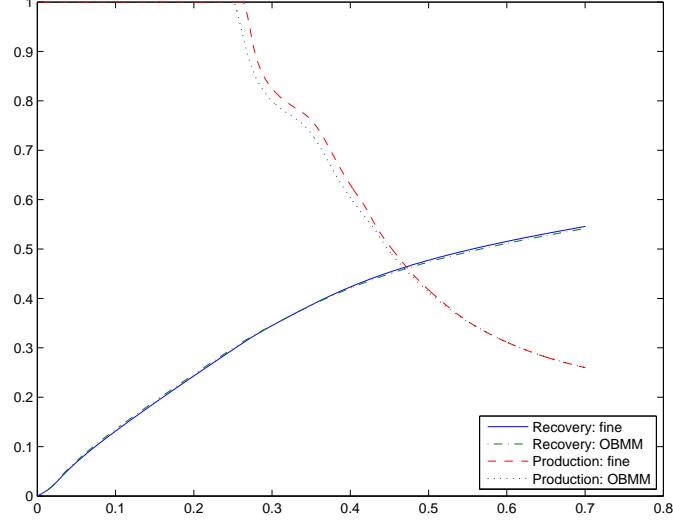


Figure 40: Oil cut and recovery curves for the compressible case

functions are less accurate than in the incompressible case. Nevertheless, the compressibility in this case is extreme, and the pressure error is reasonably small. As shown in Table III, the percentage of recomputed basis function is higher than that in the incompressible case, but it is still small.

t (PVI)	ϵ_p	ϵ_s	$f_p(\%)$
0.1	6.98e-2	2.32e-4	0.15
0.2	6.88e-2	2.43e-4	0.82
0.5	7.60e-2	2.29e-4	0.42
0.7	8.10e-2	2.27e-4	0.31

Table III: Errors and percentage of the recomputed basis functions for several time steps for the compressible case

Progress

An operator based multiscale method (OBMM) has been developed. OBMM serves as a general algebraic multiscale framework. For the incompressible flow problem, the coarse-scale operator constructed by the FVM-based OBMM is identical to the multiscale finite-volume method. OBMM accounts for compressibility effects in a natural way. The fine-scale operators contain the fine-scale compressibility information, and the basis functions are calculated with compressibility effects. The coarse-scale operators constructed by OBMM account for compressibility by summing all the fine-scale information in a coarse block and distributing the contribution to the coarse nodes according to the basis functions.

For coupled flow and transport problems, a conservative fine-scale velocity field is crucial. A conservative velocity field is reconstructed by solving Neumann problems locally on the primal coarse blocks. A sequential implicit scheme is used to solve the coupled equations. Test cases for both incompressible and compressible multiphase flow were presented, and the results obtained by OBMM are in very good agreement

with reference solutions. The permeability field in the test cases is highly heterogeneous. In the compressible flow case, the compressibility is high and the pressure variation is quite large. Such challenging features show that OBMM is a reliable framework for solving highly compressible and strongly heterogeneous problems.

The efficiency of OBMM relative to standard fine-scale methods lies in the fact that we do not solve a global fine-scale system. Constructing and solving the coarse-scale equations takes a much smaller computational effort compared with solving the global fine-scale system. Adaptive updating of the basis functions can lead to great efficiency gains. OBMM is readily extendible to more complicated physics. Moreover, it does not depend on explicit description of grid geometry and can be directly applied to unstructured models. OBMM is purely algebraic and makes full use of the fine-scale properties and equations. Thus, OBMM can be implemented in existing reservoir simulators relatively easily.

Future Plans

To improve the efficiency of the multiscale method, we plan to continue the ongoing work on developing a multiscale formulation for the transport problem (nonlinear saturation equation). The aim is to develop a fully adaptive multiscale method for the nonlinear coupling of multiphase flow and transport in highly heterogeneous problems.

Stochastic Modeling of Non-equilibrium Multiphase Flow in Porous Media

Investigators

Patrick Jenny, Associate Professor of Fluid Dynamics, ETH, Zurich; Hamdi Tchelepi, Associate Professor of Energy Resources Engineering; Manav Tyagi, Graduate Research Assistant, ETH, Zurich.

Introduction

Several mechanisms have been proposed by which CO_2 can be trapped in the rock-brine system, for example, hydrodynamic trapping [52], solution trapping [53], mineral trapping [54], and capillary trapping [55, 56]. The nonlinear multiphase flow processes involved may include nonequilibrium effects. The equilibrium condition corresponds to the case of standard Darcy's law, where the phase mobility is a function of the local saturation. In a nonequilibrium flow, the mobility can be different from the equilibrium mobility, and the difference may depend on, for example, how fast is the flow given the local balance of forces (capillary number) and whether the interface is uniform (viscosity ratio). In the past, several models have been proposed to treat nonequilibrium effects. One such model was proposed by Barenblatt [57], where the relative permeability and capillary pressure are not functions of the local saturation S , but an effective saturation η , which is related to S by a linear relaxation equation

$$\frac{\partial S}{\partial t} = \frac{1}{\tau}(\eta - S). \quad (101)$$

Here τ is the relaxation time, which is zero when flow is in equilibrium. The flow approaches the equilibrium condition with a time scale equal to this relaxation time, which in turn may depend on the flow conditions and fluid properties. There are several variations of Barenblatt's model. For example, the case when τ is a function of saturation has been considered by [58]. Here, we propose a stochastic framework for modeling nonequilibrium effects in multiphase flow in natural porous media. Unlike the deterministic model, the effective saturation is assumed to be a random variable, whose probability density function (pdf) evolves in space and time. We consider a joint-pdf of all the individual pdfs associated with each phase, and we derive an evolution equation for this joint-pdf in physical and (effective) saturation space. The problem is closed using a simple linear relaxation model, in which the effective saturation relaxes toward the actual saturation with a characteristic time scale τ .

Stochastic Framework for Multiphase Flow in Porous Media

Consider the flow of N -phases in a porous media. We define S^i as the probability to find a fluid volume of the i^{th} phase at location (\mathbf{x}, t) . With ϕ defined as the porosity of the medium, the following relation holds

$$\sum_{i=0}^{N-1} S^i = \phi. \quad (102)$$

At a location (\mathbf{x}, t) , a fluid volume has velocity, $\hat{\mathbf{u}}^i$, and mobility, $\hat{\lambda}^i$. Let \mathbf{F}^i be the average mass flux of phase i at (\mathbf{x}, t) , then

$$\mathbf{F}^i = \langle \hat{\mathbf{u}}^i \rangle_i \times \text{Probability of finding a fluid volume of phase } i \quad (103)$$

or

$$\mathbf{F}^i = \langle \hat{\mathbf{u}}^i \rangle_i S^i, \quad (104)$$

where $\langle . \rangle_i$ denotes the conditional expectation with respect to phase i . Thus, the average phase velocity is given by the following expression

$$\langle \hat{\mathbf{u}}^i \rangle_i = \frac{\mathbf{F}^i}{S^i}. \quad (105)$$

According to Darcy's law, we have the following relationship between the average mass flux of a phase and the pressure gradient

$$\text{average phase flux} = \text{average phase mobility} \times \text{pressure gradient}, \quad (106)$$

or

$$\mathbf{F}^i = - \langle \hat{\lambda}^i \rangle_i \nabla p. \quad (107)$$

From Eq.(105) and Eq.(107) we propose the following rule for the phase velocity

$$\hat{\mathbf{u}}^i = - \frac{\hat{\lambda}^i}{S^i} \nabla p. \quad (108)$$

Note that this is only one of the possible solutions of Eq.(105) and Eq.(107). By assuming incompressible flow, a poisson equation for the pressure can be derived

$$\nabla \cdot \mathbf{F} = \nabla \cdot \sum_{i=0}^{N-1} \mathbf{F}^i = q. \quad (109)$$

And it follows that

$$\nabla \cdot \left(- \sum_{i=0}^{N-1} \langle \hat{\lambda}^i \rangle_i \nabla p \right) = q. \quad (110)$$

Eq.(108) can be recast to obtain the fractional flow formulation for the phase velocity

$$\hat{\mathbf{u}}^i = \frac{\hat{\lambda}^i}{\sum \langle \hat{\lambda}^i \rangle_i S^i} \mathbf{F}. \quad (111)$$

A model for phase mobility

In the previous section, we set up a framework, in which we can deal with phase-velocity and phase-mobility as random variables. However, in order to close the problem, we need a model for the phase mobility. Let us associate a quantity \hat{S}^i with each fluid volume of phase i . \hat{S}^i is a random variable defined in the $\hat{s}^i \in (0, 1)$ space with the probability distribution function g^i . If we assume that the phase mobility is a function of \hat{S}^i alone, the expectation of phase mobility can be expressed as

$$\langle \hat{\lambda}^i \rangle_i = \int_0^1 \hat{\lambda}^i g^i d\hat{s}^i. \quad (112)$$

Next we discuss the physical meaning of \hat{S}^i .

Effective and ensemble saturation

The saturation of a phase is defined as the ratio of volumes, namely, fluid to pore, in a certain representative elemental volume (REV), i.e., it is an average quantity. This is the same as the probability of finding a phase fluid volume, S^i , and we call it the ‘ensemble saturation’. In the deterministic approach of modeling multiphase flow in porous media, the phase mobility is a function of the ‘ensemble saturation’. In the present approach, we use another quantity \hat{S}^i , which could be thought of as some effective saturation, to calculate the (local) phase mobility. Since the phase mobility can be represented using \hat{S}^i only, we can attempt to model \hat{S}^i . A simple model could be that \hat{S}^i relaxes to S^i according to a linear relaxation equation

$$\frac{d\hat{S}^i}{dt} = -\frac{1}{\tau}(\hat{S}^i - S^i), \quad (113)$$

where τ is the relaxation time. When $\tau \rightarrow 0$, \hat{S}^i is equal to S^i , and we recover the standard deterministic Darcy flow.

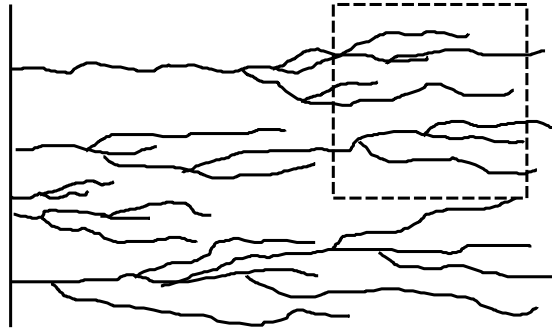


Figure 41: Fine scale structures inside REV

So far we have defined all the quantities at a particular point in the porous media. However, this point represents a volume element (REV) of some length scale, l . In other words, l is the smallest length scale, which is resolved in the problem. Fig. 41

shows a possible flow scenario over this length where the invading phase fingers through the resident phase. In the deterministic approach, it is not possible to consider the effect of such "fine" scale structures on the large-scale flow behavior. However, if we assume that the system is ergodic over the length l , a fine scale fluid volume can be taken as a realization in our model. For example, we can associate the random variable \hat{S}^i to a finger to determine its dynamics.

Transport Equation for Joint Probability Density Function (JPDF)

We can combine the individual pdfs, g^i , of \hat{S}^i into a single joint PDF of \hat{S} and \hat{A} , where $\hat{S} = \hat{S}^i$ when $\hat{A} = i$. We get

$$\mathcal{G}(\hat{s}, \hat{a}) = \sum_i S^i g^i \delta(\hat{a} - i), \quad (114)$$

and the following relation holds

$$\int \mathcal{G}(\hat{s}, \hat{a} = i; \mathbf{x}) d\hat{s} = S^i. \quad (115)$$

The evolution of \mathcal{G} in $\mathbf{x} - \hat{s} - \hat{a}$ space, is governed by the following transport equation

$$\frac{\partial \mathcal{G}}{\partial t} + \frac{\partial}{\partial x_j} \left\{ \left\langle \frac{dX_j}{dt} \middle| \hat{s}, \hat{a}; \mathbf{x} \right\rangle \mathcal{G} \right\} + \frac{\partial}{\partial \hat{s}} \left\{ \left\langle \frac{d\hat{S}}{dt} \middle| \hat{s}, \hat{a}; \mathbf{x} \right\rangle \mathcal{G} \right\} \quad (116)$$

$$+ \frac{\partial}{\partial \hat{a}} \left\{ \left\langle \frac{d\hat{A}}{dt} \middle| \hat{s}, \hat{a}; \mathbf{x} \right\rangle \mathcal{G} \right\} = 0. \quad (117)$$

After substituting the conditional expectation expressions, we obtain

$$\frac{\partial \mathcal{G}}{\partial t} + \frac{\partial}{\partial x_k} \left\{ \left(\sum_i \hat{u}_k^i \delta(\hat{a} - i) \right) \mathcal{G} \right\} \quad (118)$$

$$- \frac{\partial}{\partial \hat{s}} \left\{ \frac{1}{\tau} \sum_i (\hat{s}^i - S^i) \delta(\hat{a} - i) \mathcal{G} \right\} = 0. \quad (119)$$

Nonequilibrium capillary pressure effects

In this section, we use the stochastic framework to model nonequilibrium capillary pressure effects. We consider two-phase flow $i = 0, 1$ with the average phase pressures $p^0 = \langle \hat{p}^0 \rangle_0$ and $p^1 = \langle \hat{p}^1 \rangle_1$. The capillary pressure is a random variable defined as

$$\hat{p}^1 - \hat{p}^0 = \hat{P}_c = P_c(\hat{s}^0) \quad (120)$$

For calculating the phase velocities, we use the average pressures

$$\hat{\mathbf{u}}^i = -\hat{\lambda}^i \frac{\nabla p^i}{S^i}, \quad i = 0, 1. \quad (121)$$

The expectation of $\hat{\mathbf{u}}^i$ will be

$$\mathbf{F}^i = \langle \hat{\mathbf{u}}^i \rangle = - \langle \hat{\lambda}^i \rangle_i \frac{\nabla p^i}{S^i}, \quad i = 0, 1, \quad (122)$$

and the total mass flux is

$$\mathbf{F} = \mathbf{F}^0 S^0 + \mathbf{F}^1 S^1 = - \langle \hat{\lambda}^i \rangle_0 \nabla p^0 - \langle \hat{\lambda}^i \rangle_1 \nabla p^1 \quad (123)$$

Taking the average of Eq.(120)

$$\langle p^1 \rangle_1 - \langle p^0 \rangle_0 = p^1 - p^0 = \langle P_c(\hat{s}^0) \rangle_0 \quad (124)$$

Substituting for p^1 in Eq.(123)

$$\mathbf{F} = - \langle \hat{\lambda}^0 \rangle_0 \nabla p^0 - \langle \hat{\lambda}^1 \rangle_1 \nabla p^0 - \langle \hat{\lambda}^1 \rangle_1 \nabla \langle P_c(\hat{s}^0) \rangle_0 \quad (125)$$

From the above relation, we get an expression for ∇p^0

$$\nabla p^0 = \frac{-\mathbf{F} - \langle \hat{\lambda}^1 \rangle_1 \nabla \langle P_c(\hat{s}^0) \rangle_0}{\langle \hat{\lambda}^0 \rangle_0 + \langle \hat{\lambda}^1 \rangle_1}, \quad (126)$$

and for ∇p^1

$$\nabla p^1 = \frac{-\mathbf{F} + \langle \hat{\lambda}^0 \rangle_0 \nabla \langle P_c(\hat{s}^0) \rangle_0}{\langle \hat{\lambda}^0 \rangle_0 + \langle \hat{\lambda}^1 \rangle_1}. \quad (127)$$

We can write the phase velocities in fractional flow form as follows

$$\hat{\mathbf{u}}^0 = \frac{\hat{\lambda}^0 \mathbf{F}}{S^0(\langle \hat{\lambda}^0 \rangle_0 + \langle \hat{\lambda}^1 \rangle_1)} + \frac{\hat{\lambda}^0 \langle \hat{\lambda}^1 \rangle_1 \nabla \langle P_c(\hat{s}^0) \rangle_0}{S^0(\langle \hat{\lambda}^0 \rangle_0 + \langle \hat{\lambda}^1 \rangle_1)}, \quad (128)$$

and

$$\hat{\mathbf{u}}^1 = \frac{\hat{\lambda}^1 \mathbf{F}}{S^1(\langle \hat{\lambda}^0 \rangle_0 + \langle \hat{\lambda}^1 \rangle_1)} - \frac{\hat{\lambda}^1 \langle \hat{\lambda}^0 \rangle_0 \nabla \langle P_c(\hat{s}^0) \rangle_0}{S^1(\langle \hat{\lambda}^0 \rangle_0 + \langle \hat{\lambda}^1 \rangle_1)}. \quad (129)$$

Numerical Results

The joint-pdf for transport derived in the previous section is solved using a Finite Volume Method (FVM). Here we present some one-dimensional results for the classical Buckley-Leverett problem. We also solve the problem using the stochastic particle method (SPM) [59] and compare the results with FVM. In FVM, we use 100×100 grid to discretize Eq. 118. The mass flow rate F is 1 m s^{-1} . We assume the following initial condition for the pdfs

$$g^0 = \delta(x) \frac{\delta(\hat{s} - S_{in})}{\Delta x} + (1 - \delta(x)) \frac{\delta(\hat{s} - S_{out})}{\Delta x}, \quad (130)$$

$$g^1 = \delta(x) \frac{\delta(\hat{s} - S_{out})}{\Delta x} + (1 - \delta(x)) \frac{\delta(\hat{s} - S_{in})}{\Delta x}, \quad (131)$$

where S_{out} is the initial saturation in the domain and S_{in} is the saturation of injected fluid at $x = 0$.

In order to show the effect of the relaxation parameter on the flow process, we consider a test case in which τ increases suddenly by a factor of 100 at $x = 0.3$. Fig. 42 shows the saturation profiles at different time intervals for the case when $S_{in} = 0.95$ and $S_{out} = 0.05$. Fig. 43 shows the corresponding time evolution of the pdf. In order to check the validity of the code, we also solve the problem by SPM. Fig. 44 shows the comparison of the solutions obtained from SPM and FVM for two different values of τ . Next we vary τ . Fig. 45 depicts the saturation profiles for different values of τ with $S_{in} = 0.95$ and $S_{out} = 0.05$. Fig. 46 depicts the saturation profiles for different values of τ with $S_{in} = 0.8$ and $S_{out} = 0.2$. For the second case, we compare the mean and ensemble saturation in Fig. 47. It clear that for large values of τ the difference between the mean and ensemble saturations is significant.

Discussion and Conclusions

The main idea behind this work is to show how one can deal with the randomness in a large scale flow quantity arising because of pore-scale fluctuations. Here we consider the example of effective saturation (phase mobility) and derive a transport equation for the joint-pdf of the effective saturations associated with the phases. The transport equation can either be solved by a finite-volume method (FVM), or by constructing an equivalent stochastic system with the same joint-pdf and then performing monte carlo simulation using the stochastic particle method (SPM) [59]. If the dimensionality of the problem is up to four, then FVM is expected to be less expensive than SPM. However, for high-dimensional problems, numerical solutions are feasible only with SPM. In our examples here, in addition to physical space of location and time, we have only one extra dimension representing the saturation space. As a result, the FVM method is quite efficient.

From the modeling viewpoint we showed how a simple relaxation model for effective saturation can give rise to drastic change in the flow behavior. In this model, we have a parameter, τ which could be tuned such that the capillary pressure and

relative permeability relations as a function of saturation represent large-scale dynamics more accurately. In this framework, the relative probabilities and capillary pressure are no longer fixed functions of the ensemble saturations and depend upon how far the flow is from equilibrium. Although the selection of τ for a particular flow problem is an open question, we hope that a detailed study of pore-scale flow dynamics, either by performing pore-network simulations, or by doing high-resolution experiments, may provide reasonable values for τ under various conditions. The present framework can be easily extended for the modeling CO_2 dissolution in brine and for accounting for chemical reactions. Similar to the effective saturation we can consider a composition vector of the species associated with the each phase

$$\hat{\phi} = \hat{\phi}_1, \hat{\phi}_2, \dots, \hat{\phi}_n^T \quad (132)$$

Each species may undergo some chemical change according to the following equation

$$\frac{d\hat{\phi}_i}{dt} = \hat{R}_i \quad (133)$$

Consider a joint-pdf $\mathcal{F}(\hat{\psi}_1, \hat{\psi}_2, \dots, \hat{\psi}_n, \hat{a})$ of $\hat{\phi}_1, \hat{\phi}_2, \dots, \hat{\phi}_n, \hat{A}$ in $(\hat{\psi}_1 - \hat{\psi}_2, \dots - \hat{\psi}_n - \hat{a} - \mathbf{x} - t)$ space. Similar to Eq. 116, we can derive a transport equation for \mathcal{F} .

$$\frac{\partial \mathcal{F}}{\partial t} + \frac{\partial}{\partial x_j} \left\{ \left\langle \frac{dX_j}{dt} \middle| \hat{s}, \hat{a}; \mathbf{x} \right\rangle \mathcal{F} \right\} + \frac{\partial}{\partial \hat{\psi}_1} \left\{ \left\langle \frac{d\hat{\phi}_1}{dt} \middle| \hat{\psi}, \hat{a}; \mathbf{x} \right\rangle \mathcal{F} \right\} \quad (134)$$

$$+ \frac{\partial}{\partial \hat{\psi}_2} \left\{ \left\langle \frac{d\hat{\phi}_2}{dt} \middle| \hat{\psi}, \hat{a}; \mathbf{x} \right\rangle \mathcal{F} \right\} \dots + \frac{\partial}{\partial \hat{\psi}_n} \left\{ \left\langle \frac{d\hat{\phi}_n}{dt} \middle| \hat{\psi}, \hat{a}; \mathbf{x} \right\rangle \mathcal{F} \right\} \quad (135)$$

$$+ \frac{\partial}{\partial \hat{a}} \left\{ \left\langle \frac{d\hat{A}}{dt} \middle| \hat{s}, \hat{a}; \mathbf{x} \right\rangle \mathcal{F} \right\} = 0. \quad (136)$$

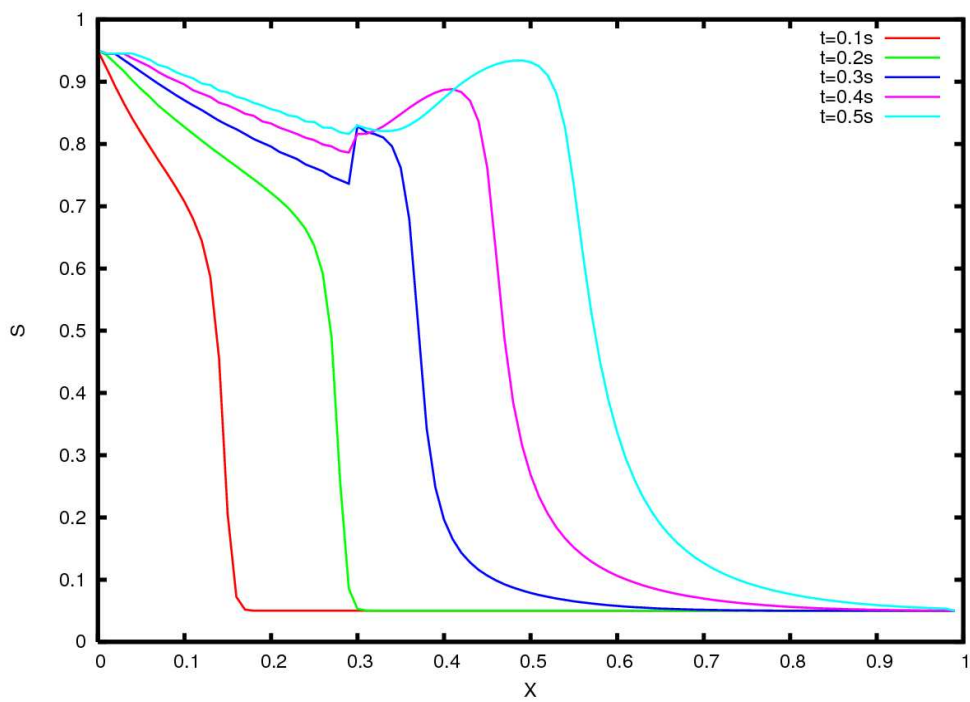


Figure 42: Evolution of ensemble saturation in a medium where τ changes from 0.001 to 0.1 at $x = 0.3$. $S_{in} = 0.95$ and $S_{out} = 0.05$.

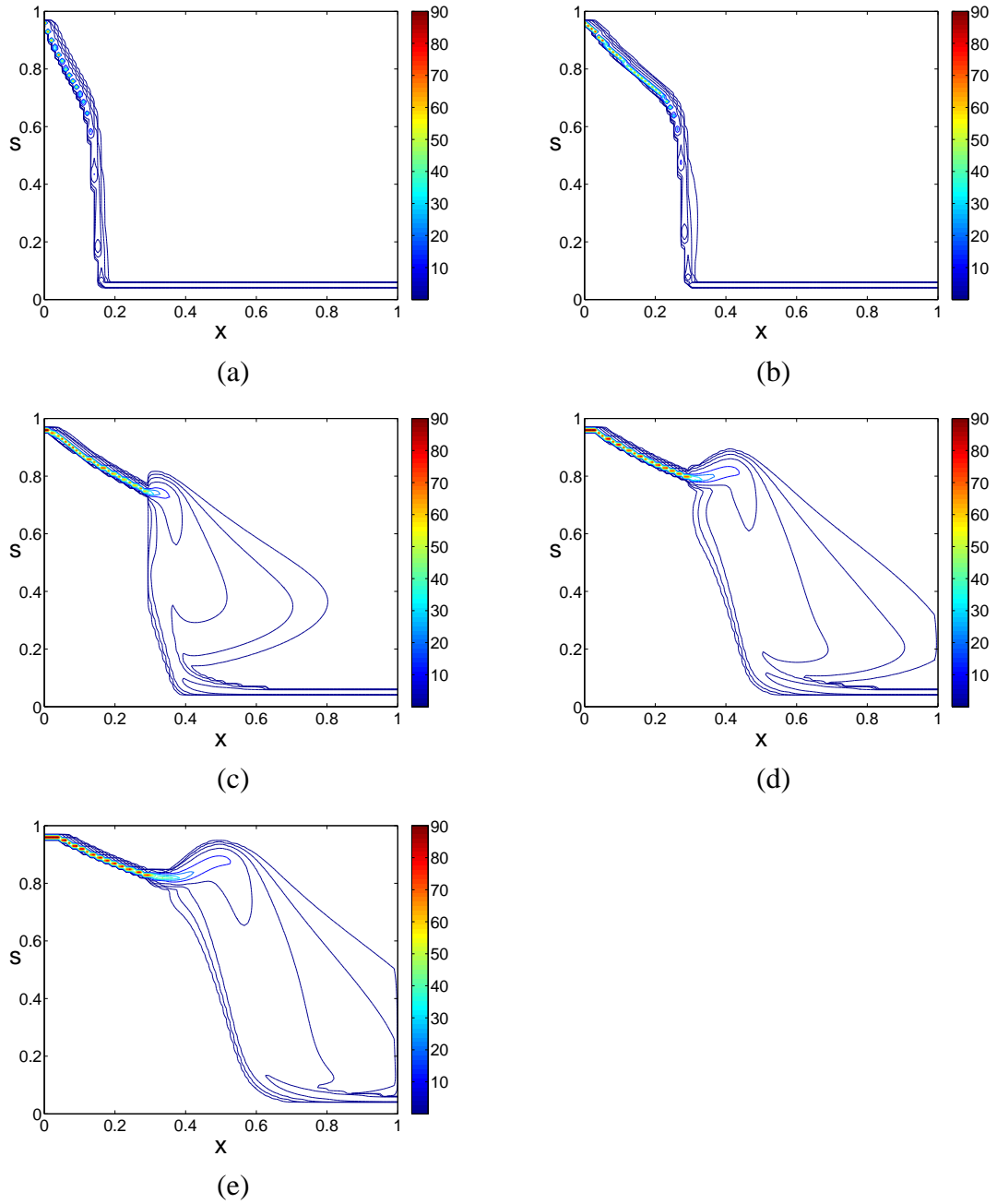
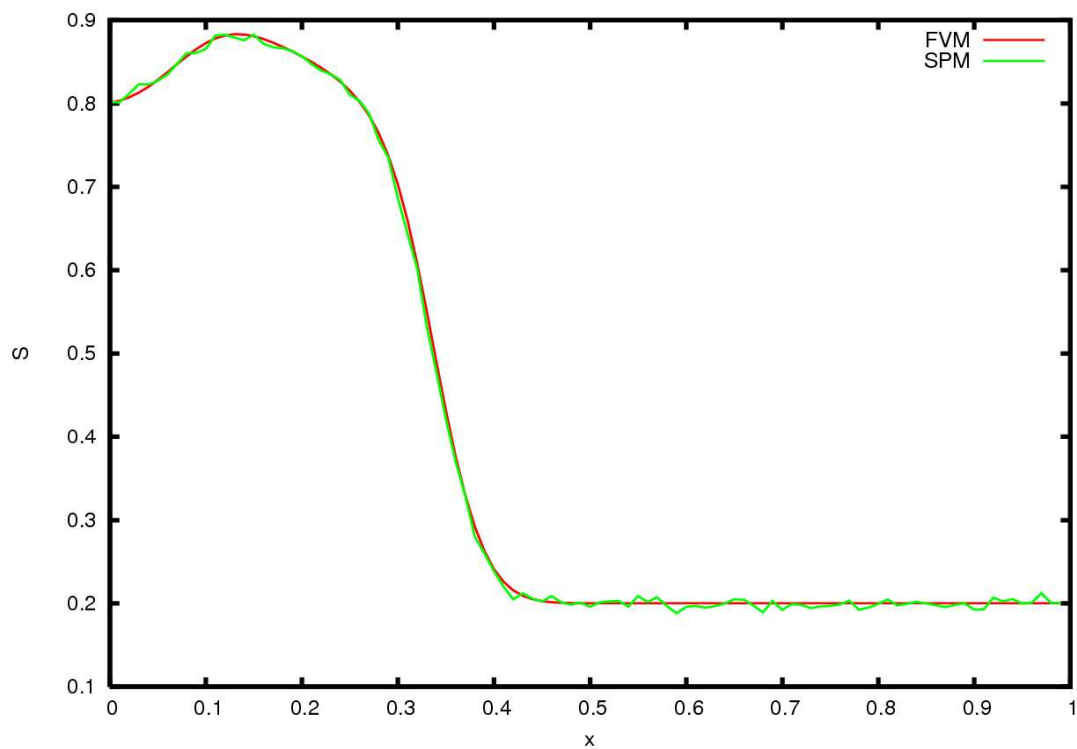
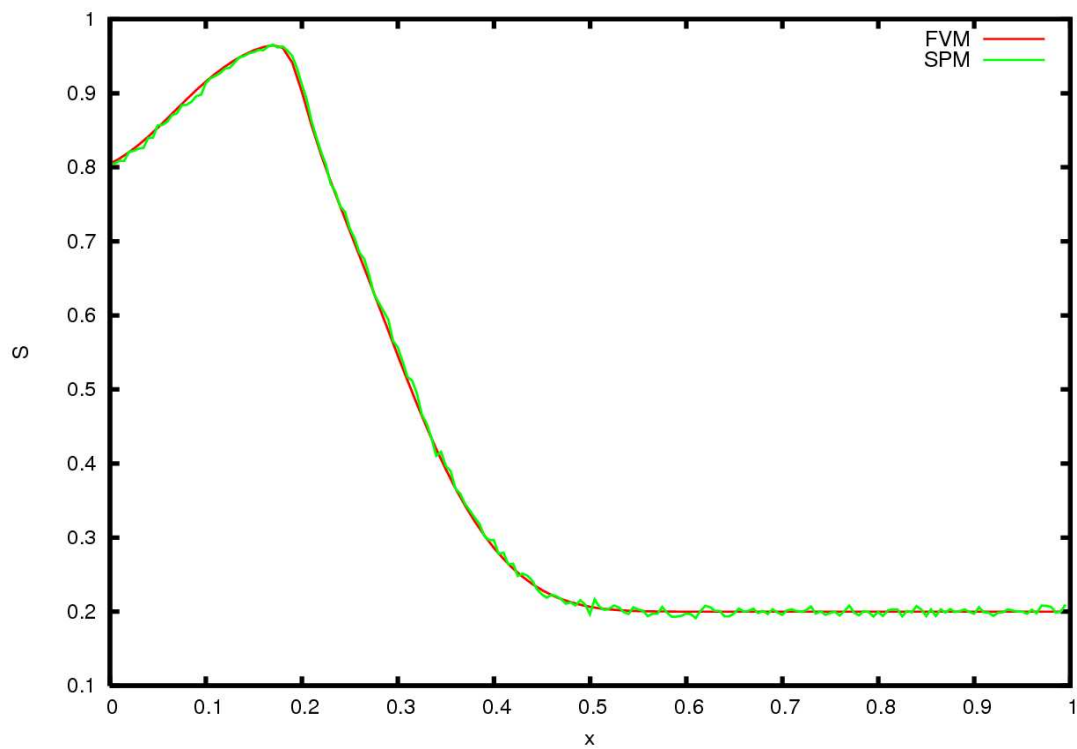


Figure 43: Evolution of pdf in a medium where τ changes from 0.001 to 0.1 at $x = 0.3$; (a) $t = 0.1s$ (b) $t = 0.2s$ (c) $t = 0.3s$ (d) $t = 0.4s$ (e) $t = 0.5s$. $S_{in} = 0.95$ and $S_{out} = 0.05$.



(a)



(b)

Figure 44: Comparison of the finite volume method for solving pdf transport equation with the stochastic particle method; (a) $\tau = 0.04$ (b) $\tau = 0.1$ $S_{in} = 0.8$ and $S_{out} = 0.2$.

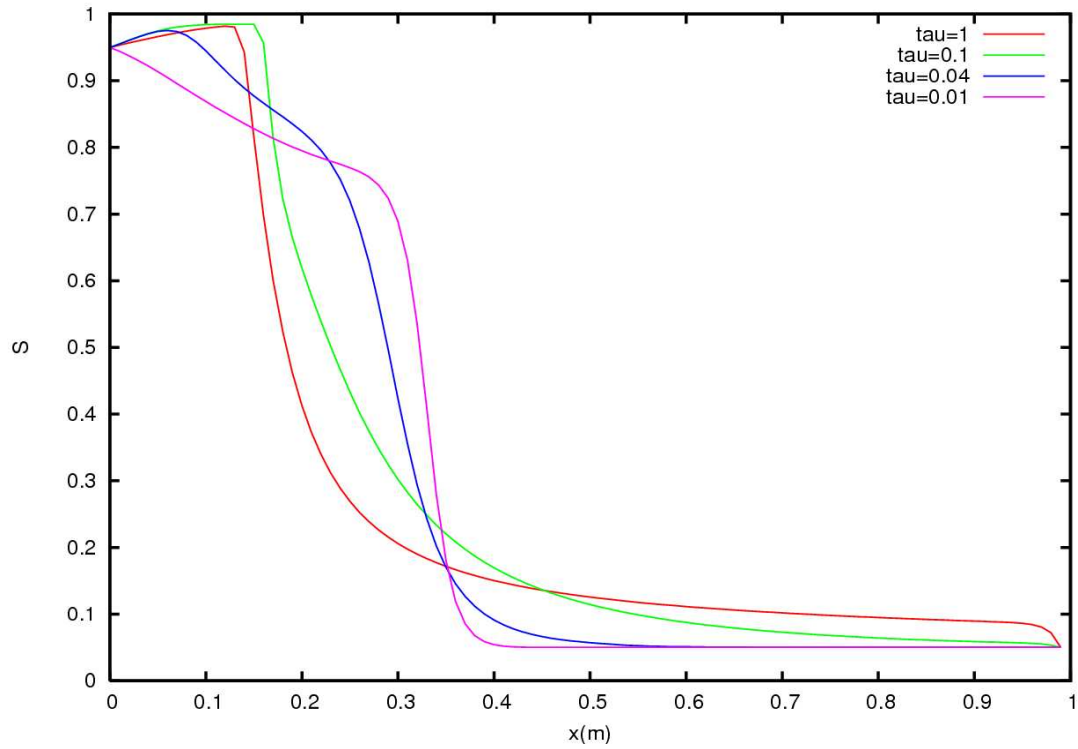


Figure 45: Ensemble saturation profiles for the different values of relaxation time τ (finite volume method). $S_{in} = 0.95$ and $S_{out} = 0.05$.

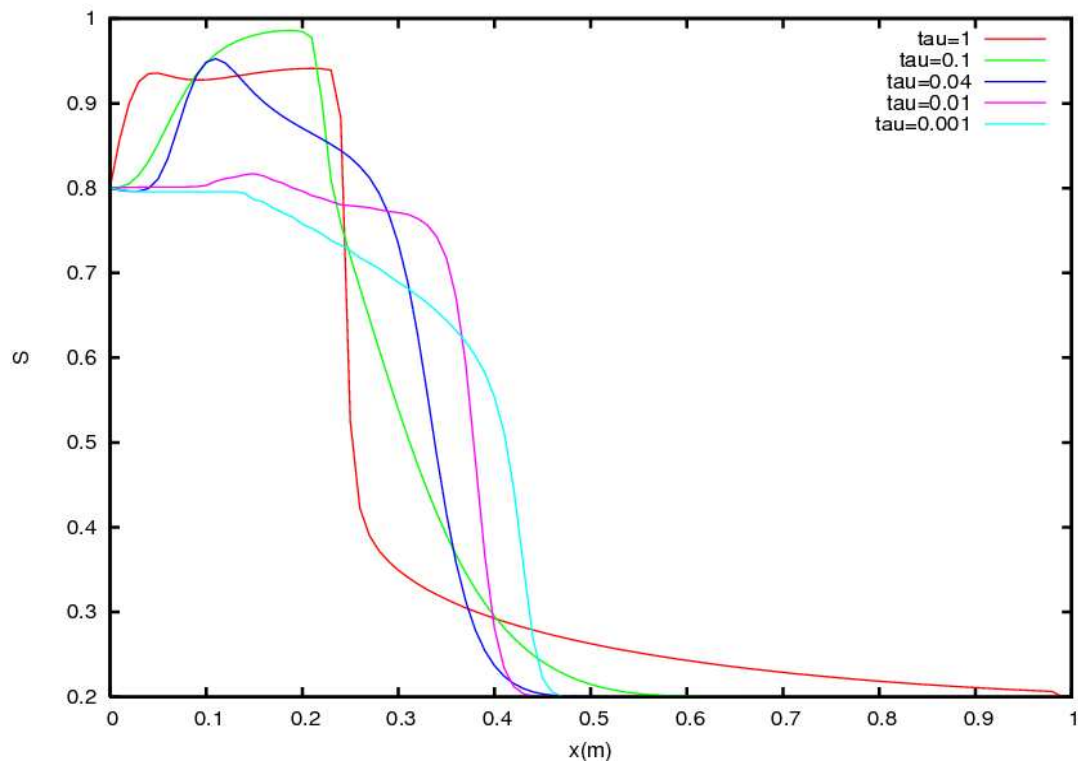


Figure 46: Ensemble saturation profile for the different values of relaxation time τ (finite volume method). $S_{in} = 0.8$ and $S_{out} = 0.2$.

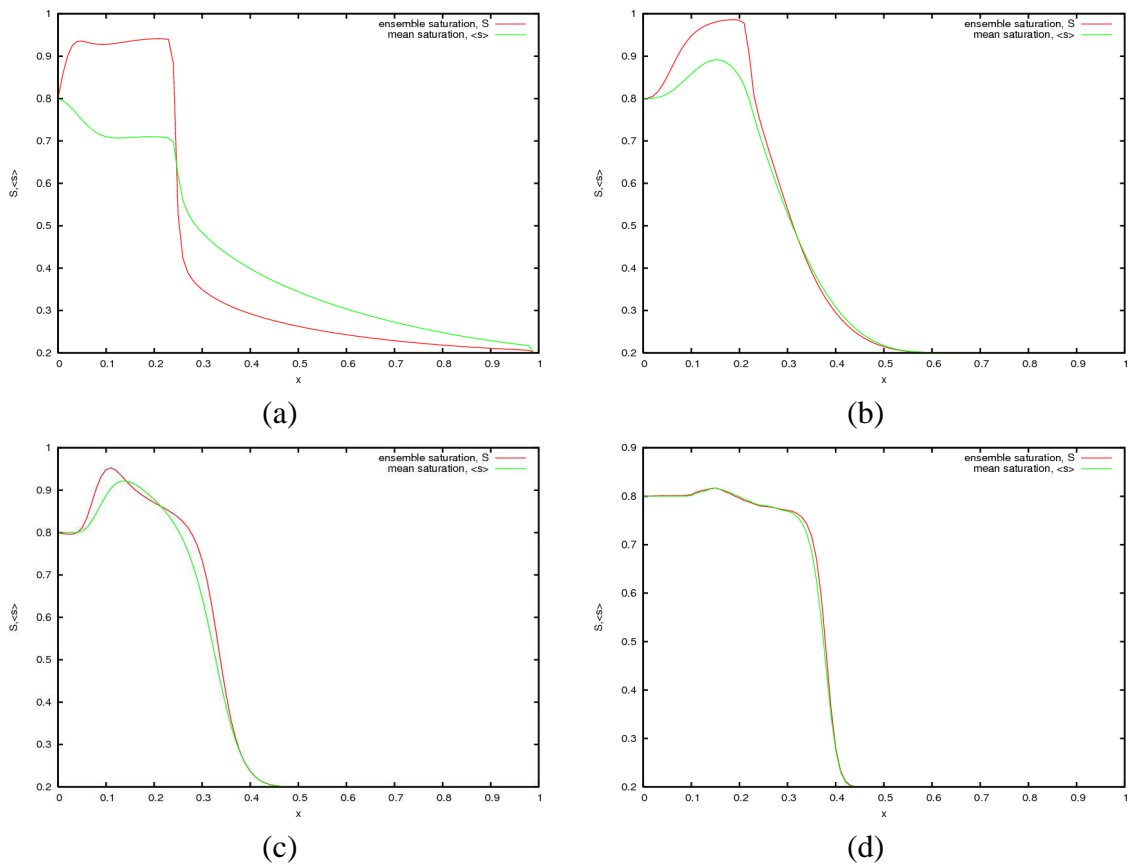


Figure 47: Mean and ensemble saturation profiles for the different values of relaxation time τ (finite volume method); (a) $\tau = 1$ (b) $\tau = 0.1$ (c) $\tau = 0.04$ (d) $\tau = 0.01$. $S_{in} = 0.8$ and $S_{out} = 0.2$.

Modeling CO₂ Mineralization Reactions in a General Purpose Flow Simulator

Investigators

Lou Durlofsky, Professor of Energy Resources Engineering; Hamdi Tchelepi, Associate Professor of Energy Resources Engineering; Yaqing Fan, Graduate Research Assistant

Introduction

The design and monitoring of geological carbon storage operations require many key capabilities, including advanced techniques for computational modeling. Because an important long-term storage mechanism is the mineralization of the injected CO₂ [60], it is essential that large-scale engineering models accurately represent the chemical interactions between liquids and minerals. The goal of this work is to develop a robust, flexible and efficient capability for such modeling and to incorporate it into Stanford's General Purpose Research Simulator (GPRS).

GPRS is our platform for research in the areas of general reservoir simulation and geological storage of carbon dioxide. The simulator is object oriented, flexible and extensible, and has many advanced features (as described below) that render it particularly well suited for both sets of applications. As discussed in last year's annual report to GCEP (and described in full detail in Fan's MS thesis [61]), we recently incorporated several mechanisms (e.g., three-phase relative permeability hysteresis, dispersion) that are required for accurate modeling of CO₂ sequestration into this simulator. With the introduction of CO₂ mineralization reactions, the simulator will be able to model all of the key currently known mechanisms for the long-term geological storage of carbon dioxide.

Chemical reaction modeling within the context of CO₂ sequestration has been studied by several research groups and incorporated into a number of simulators. It is therefore of interest to distinguish our work from these earlier efforts. CMG's GEM simulator is a coupled reactive-transport compositional simulator based on generalized equations of state. Extensions were introduced to model the chemical reactions related to asphaltene precipitation and GHG sequestration. Specifically, Nghiem *et al.* [62] enhanced GEM to include mineral dissolution and precipitation kinetics. TOUGHREACT [63] is a reactive-transport simulator developed by Lawrence Berkeley National Laboratory. Interactions between gas, minerals, and liquid are modeled. The software package NUFT [64], developed by Lawrence Livermore National Laboratory, has similar capabilities to TOUGHREACT. UTCHEM [65] is a simulator developed by The University of Texas at Austin which includes

reactive-transport with chemical and biological reactions.

Our intent is to develop GPRS as a generalized compositional - chemical reaction simulator. GPRS already has many advanced features such as the ability to use unstructured (e.g., tetrahedral or general control volume) grids and adaptive implicit (AIM) treatments that are lacking or less well developed in the other simulators. Figure 48 compares GPRS with the simulators discussed above in terms of features. Note that GPRS has all of the features of the other simulators with the exception of chemical reactions. In addition, GPRS is formulated quite generally; this will allow us to investigate a variety of numerical treatments for modeling coupled flow and reaction systems. Such assessments cannot be accomplished (or can be accomplished to much less of an extent) with existing simulators. Finally, we note that GPRS is compatible with adjoint-based computational optimization techniques, which can be used to optimize carbon storage operations. Thus it is clearly worthwhile to implement a chemical reaction modeling capability into GPRS.

Features	GEM	TOUGH	NUFT	UTCHEM	GPRS
Generalized Compositional	⦿	⦿	⊖	⦿	✓
Unstructured Grids	⊖	✓	⊖	⊖	✓
Chemical Reactions	⦿	✓	✓	✓	⊖
Adaptive Implicit	✓	⊖	⊖	⊖	✓
Thermal Options	⊖	✓	✓	✓	✓
Advanced Facilities (Wells)	⊖	⊖	⊖	⊖	✓
Optimization	⦿	⦿	⦿	⦿	✓

⊖ Not Available ⦿ Not Fully Flexible or Efficient ✓ Available and Flexible

Figure 48: Comparison of simulator capabilities

In the following sections of this report, we describe the proposed mathematical formulation and strategy for incorporating chemical reactions into GPRS. In this formulation, we reduce the number of species we are tracking and distinguish (i.e., introduce separate treatments for) fast and slow reactions. Finally, preliminary results are shown for a case involving flow and equilibrium chemistry.

Chemical Reaction Modeling in GPRS

We now describe our approach for chemical reaction modeling in the context of a general purpose compositional formulation. The basic equations and our approach for model reduction are discussed.

Model Formulation

When chemistry is introduced into a compositional simulator, new relations are established for each reaction. We describe the formulation using a simple combustion process between CO and O₂:



We can write an equation relating pressure p , temperature T , and mole fraction X_c of each component

$$F_r(p, T, X_{\text{CO}}, X_{\text{O}_2}, X_{\text{CO}_2}) = 0. \quad (138)$$

Here F_r is the residual equation for reaction (137).

A new term in the mass conservation equation is required to account for the mass change due to reactions. For a particular control volume (grid cell), the mass conservation equation for each component c can be expressed as

$$A_c - (In - Out)_c + q_c^r = 0, \quad (139)$$

where A_c is the accumulation of component c over the time step, In and Out are the mass flowing in and out of the control volume, and q_c^r is a source term for component c due to chemical reaction. Well source terms are not included in this description for simplicity.

For the combustion reaction (137), we can write the mass balance equations for CO, O₂, and CO₂ as

$$F_{\text{CO}} = A_{\text{CO}} - (In - Out)_{\text{CO}} + q_{\text{CO}}^r = 0, \quad (140)$$

$$F_{\text{O}_2} = A_{\text{O}_2} - (In - Out)_{\text{O}_2} + q_{\text{O}_2}^r = 0, \quad (141)$$

$$F_{\text{CO}_2} = A_{\text{CO}_2} - (In - Out)_{\text{CO}_2} + q_{\text{CO}_2}^r = 0. \quad (142)$$

The reaction source terms are not independent, because each element (C and O) is conserved in reaction (137). Thus the following relations hold:

$$q_{\text{CO}}^r + q_{\text{CO}_2}^r = 0, \quad (143)$$

$$q_{\text{CO}}^r + 2q_{\text{O}_2}^r + 2q_{\text{CO}_2}^r = 0. \quad (144)$$

Equations (143) and (144) can be used to eliminate the reaction source terms in equations (140)-(142) to obtain element balance equations for C and O:

$$F_{\text{C}} = F_{\text{CO}} + F_{\text{CO}_2} = [A_{\text{CO}} - (In - Out)_{\text{CO}}] + [A_{\text{CO}_2} - (In - Out)_{\text{CO}_2}] = 0, \quad (145)$$

$$F_{\text{O}} = F_{\text{CO}} + 2F_{\text{O}_2} + 2F_{\text{CO}_2} = [A_{\text{CO}} - (In - Out)_{\text{CO}}] + 2[A_{\text{O}_2} - (In - Out)_{\text{O}_2}] + 2[A_{\text{CO}_2} - (In - Out)_{\text{CO}_2}] = 0.$$

Before generalizing the treatment described above, it is useful to define some notation. Let N_c be the number of components, including hydrocarbons, aqueous

species, and minerals. The number of elements is denoted by N_e . The number of reactions is N_r , consisting of N_{eq} reactions at equilibrium and N_{neq} nonequilibrium reactions controlled by reaction rates. It is always the case that $N_r = N_{eq} + N_{neq}$.

In general, the N_c component mass balance equations can be transformed to N_e element balance equations by linear combinations (as above) to eliminate reaction source terms, as long as the reactions occur within the target block and within the time step. This is often the case in subsurface reactive-transport problems and we will use this assumption in the first phase of this work. We may eventually need to treat situations in which reactions in a particular block depend strongly on effects in surrounding blocks, in which case our treatment will be extended.

After the linear transformation from component balance equations to element equations, the computational cost will be reduced significantly compared to the case when all components are tracked. In fact, because the number of components can be very large (due to complex reactions), it is usually not practical or desirable to solve for all components simultaneously. The number of elements, by contrast, is usually much smaller, particularly when we have a large number of components composed of only a few elements. Thus, tracking N_e elements is generally much more efficient computationally than tracking N_c components.

We can further reduce the number of governing equations and unknowns by treating fast reactions and slow reactions separately. In general, chemical reactions can be roughly divided into two groups: ‘sufficiently fast and reversible’ reactions, and ‘slow or irreversible’ reactions. In the first group, the time scales for the reactions are small compared to the global time step, so these reactions can be assumed to reach equilibrium instantaneously. For example, the hydrolysis of calcium chloride is sufficiently fast such that the equilibrium state is reached in each block at every time step. For this reaction we have:



$$K_{eq} = \frac{a_{\text{Ca}^{2+}} a_{\text{Cl}^-}^2}{a_{\text{CaCl}_2}}, \quad (147)$$

where a is activity of the component, which is related to mole fraction via the activity coefficient γ

$$a = \gamma_c X_c. \quad (148)$$

Rearranging equation (147),

$$X_{\text{Ca}^{2+}} = \frac{K_{eq} a_{\text{CaCl}_2}}{\gamma_{\text{Ca}^{2+}} a_{\text{Cl}^-}^2}. \quad (149)$$

Equation (149) indicates that the mole fraction of Ca^{2+} can be expressed explicitly in terms of other variables. Therefore, $X_{\text{Ca}^{2+}}$ can be updated locally after each time step rather than being computed in the full set of governing equations.

We now consider the second type of reactions, so-called ‘rate-controlled’ reactions, which are generally not in equilibrium. The reaction in (150) is such a reaction, with a temperature-dependent rate k_f



$$\frac{dX_{CO}}{dt} = -2k_f X_{CO}^2 X_{O_2}. \quad (151)$$

It is usually not easy to express X_{CO} as an explicit function of other variables. In addition, if the reaction rate is so slow that it depends on the mole fractions of neighboring cells, equation (151) has to be discretized and solved together with the element conservation equations. Such a treatment will, if necessary, be considered in the future.

The equations and unknowns for a two-phase non-isothermal case are listed in the following summary table.

Table IV: Governing equations and unknowns

Equations		Unknowns	
N_e	mass balance equations	2	pressures
N_c	thermodynamic equations	2	saturations
1	saturation constraint	$2N_c - N_{eq}$	mole fractions
2	mole fraction constraints		
1	capillary pressure relations		
N_{neq}	slow reaction relations		
sum = $N_e + N_c + N_{neq} + 4$		$2N_c - N_{eq} + 4$	

In GPRS, the equations and variables are split into primary and a secondary parts. The fully implicit method (FIM) solves the primary equations for each block together (implicitly) and then updates the secondary variables locally. The basis for this method is that the number of primary equations (and variables) is equal to the number of degrees of freedom at equilibrium conditions, as determined by the Gibbs phase rule. According to the Gibbs phase rule, the thermodynamic degrees of freedom (N_D) for a system with N_{eq} reactions at equilibrium is

$$N_D = N_c - N_{eq} = N_c - (N_r - N_{neq}). \quad (152)$$

Since $N_c = N_e + N_r$, we have that $N_D = N_e + N_{neq}$. If the N_{neq} reactions occur locally, the number of primary equations is then N_e . A natural choice for the primary equations thus appears to be N_e element balance equations. As we describe below, such a representation can be readily accomplished at the matrix level within GPRS.

Proposed Strategy and Implementation Plans

The incorporation of chemistry into GPRS requires switching mass balance equations to element balance equations and redefining the primary equations and variables. It would be extremely difficult and time consuming to reconstruct the current GPRS framework if the equations were re-written (and re-discretized) in terms of element balances. Rather, we propose a strategy that aims to minimize the code changes while maintaining code extensibility. This approach entails changing the code mainly at the Jacobian (linear solution) level.

Using this procedure, instead of rewriting the mass conservation equations in terms of element balances, we use the current mass balance equations to construct the Jacobian matrix. Then, instead of forming the derivatives required for the element balance equations directly, these derivatives are obtained by performing linear transformations on the Jacobian matrix. In GPRS, these transformations are performed after all of the governing equations are discretized. The Jacobian matrix for the facilities (i.e., wells) requires similar linear transformations. The process of reducing from the full equation set to the set of primary equations is very similar to reduction procedures already performed in the current code.

Besides the manipulation of the Jacobian matrix, the local equilibrium calculations also need to be modified to account for chemical reactions. The equilibrium state now must satisfy both chemical and thermodynamic equilibrium relations. Two strategies could be applied for this. In the first approach, the thermodynamic and chemical equilibrium equations are calculated iteratively until the results for both converge. In the second approach, the two sets of equilibrium equations are solved together until convergence. The first approach is used in the initial implementation in GPRS (as shown in the case in the next section). The second approach will be explored soon in order to determine which treatment is superior.

The implementation plan is divided into three stages. In the first stage, a local equilibrium module will be developed. The second stage entails transforming the Jacobian matrix to calculate coupled reactive-transport equations. After these stages are completed, GPRS will be able to solve chemical reaction problems in which reactions are either at equilibrium or are rate-controlled. However, the chemical reactions must not have significant dependency on surrounding blocks. In the third stage, we will investigate how to incorporate reactions that are affected by surrounding blocks.

Preliminary Results

A simple case involving CO₂ injection into a carbonate reservoir is now presented. In the results presented here we consider only local chemical equilibrium reactions.

Model Description

The reservoir is modeled as a one-dimensional homogeneous carbonate reservoir, in which the reactive mineral is calcite (CaCO₃). Initially, the reservoir is saturated with 100% water. Initial equilibrium is established between water, calcite, and electrolytes in the water. A pure CO₂ stream is injected at one end of the reservoir and a producer is introduced at the other end (as shown in Figure 49). The parameters describing the reservoir are listed in Table V.

A total of four equilibrium reactions are considered. The reactions and their equilibrium constants are listed in Table VI. The species in these reactions are distributed in the three phases. The gas phase contains CO₂ and H₂O, the solid phase contains calcite only, and the aqueous phase contains CO₂(aq), H₂O and all ions. In the current calculation, neither ion adsorption nor ion change is included, and the ions

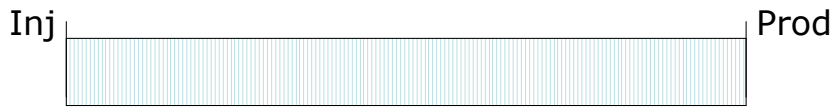


Figure 49: 1-D reservoir model

Table V: Model parameters for 1-D carbonate reservoir

Parameter	Values
block size	$200 \times 200 \times 20 \text{ ft}^3$
tops	8300 ft
porosity	0.3
temperature	104 °F
grid	$100 \times 1 \times 1$
well location	Injector: (1 , 1 , 1), Producer: (100 , 1 , 1)
permeability k_x	100 mD

are assumed to be in the aqueous phase only.

Table VI: Reactions in 1-D carbonate reservoir

Reaction	Equilibrium Constant (K_{eq})
$\text{CO}_2(\text{aq}) + \text{H}_2\text{O} = \text{HCO}_3^- + \text{H}^+$	3.981×10^{-7}
$\text{HCO}_3^- = \text{H}^+ + \text{CO}_3^{2-}$	1.995×10^{10}
$\text{H}_2\text{O} = \text{H}^+ + \text{OH}^-$	1.000×10^{14}
$\text{CaCO}_3 = \text{Ca}^{2+} + \text{CO}_3^{2-}$	4.467×10^9

In this case, we solve the flow equations for CO_2 and H_2O first to obtain the saturations and mole fractions. Then the chemical equilibrium module is used to calculate the molalities of each species in the aqueous phase. The amount of dissolution or precipitation of calcite can then be obtained.

Simulation Results

The results shown below are the equilibrium state after 2000 days of CO_2 injection. Figure 50 shows the saturation of the gas phase. The injected CO_2 front is approximately at the 15th block. The conditions beyond the 30th block are still essentially at the initial state. Figure 51 shows the mole fraction of $\text{CO}_2(\text{aq})$ and the pH value. We can see that the dissolved CO_2 reduces the pH value from approximately 9.5 to about 5.5. From the curve of the mole fraction of CO_2 , we observe that the aqueous phase is changed from near-zero CO_2 concentration to CO_2 mole fraction around 0.03 (Figure 51).

Figure 52 shows the mole fractions of aqueous species containing carbon. This

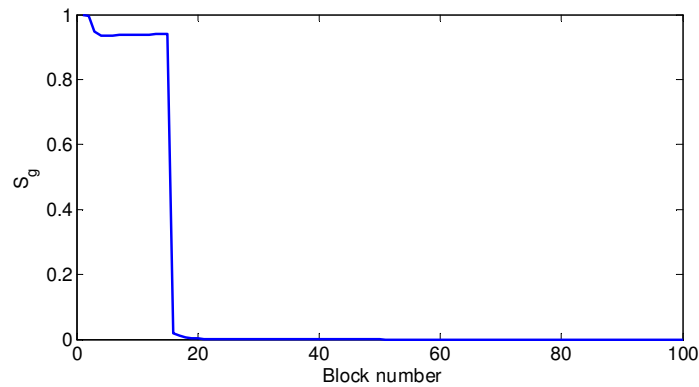


Figure 50: Gas saturation at 2000 days

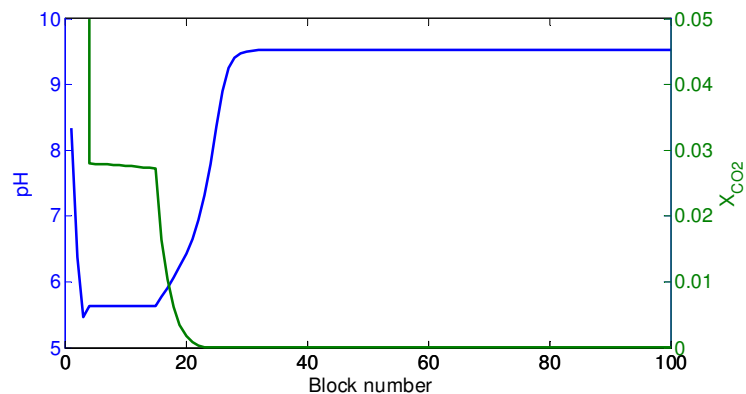


Figure 51: pH and CO₂ mole fraction in aqueous phase at 2000 days

figure indicates that behind the gas front the dominant species are HCO_3^- and $\text{CO}_2(\text{aq})$, and that the mole fraction of CO_3^{2-} is around 5 orders of magnitude less than HCO_3^- or CO_2 . Figure 53 shows that the mole fraction of Ca^{2+} is significantly increased by CO_2 injection, indicating more calcite is dissolved in the water.

Progress and Future Plans

In this report, we described our initial work on the implementation of chemical reaction modeling into our General Purpose Research Simulator (GPRS). The motivation and current focus of this work is to simulate chemical reactions relevant to

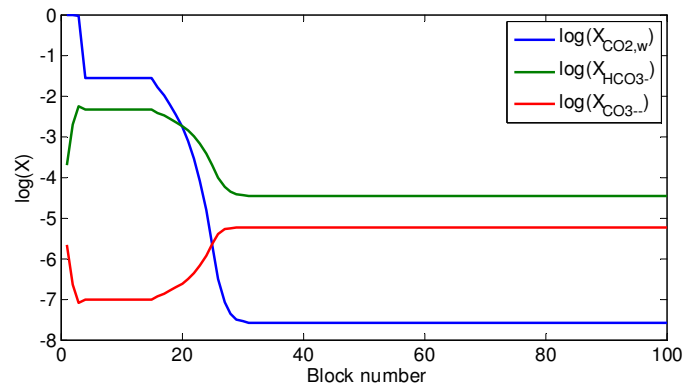


Figure 52: Carbon distribution at 2000 days

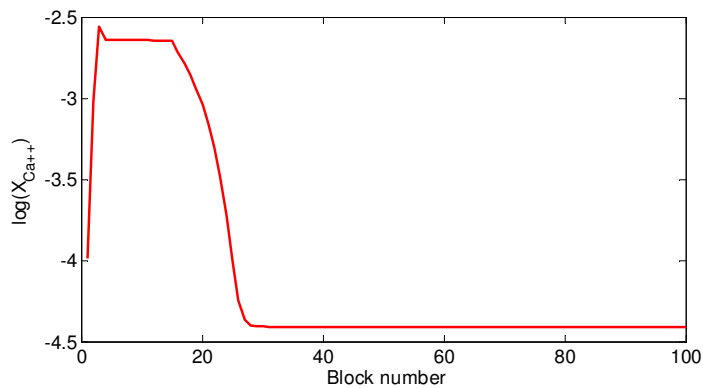


Figure 53: Calcium ion mole fraction in aqueous phase at 2000 days

CO₂ sequestration. The initial design and implementation strategy have been completed. The design entails element balance equations, and effectively utilizes the current GPRS framework because many of the key changes are introduced at a low level (i.e., the Jacobian matrix level) in the code. Preliminary results have been obtained for a simple case that models CO₂ injection into a carbonate reservoir with equilibrium chemistry.

The next step is to complete the implicitly coupled reactive-transport implementation. This work is expected to make GPRS an efficient and flexible simulator that accounts for both equilibrium and rate-controlled reactions occurring

locally. As GPRS contains a variety of numerical options for treating flow, we plan to explore the use of various combinations of options for modeling flow and reaction. We expect this to provide an efficient and flexible overall capability for the modeling of carbon dioxide injection and geologic storage.

Publications

- 1 Y. Fan. Development of CO₂ modeling capabilities in Stanford General Purpose Reservoir Simulator, M.S Thesis, June 2006.
- 2 M. A. Hesse, H. A. Tchelepi, B. J. Cantwell, and F. M. Orr, Jr. Gravity currents in horizontal porous layers: Transition from early to late self-similarity. *Journal of Fluid Mechanics*, Vol. 577, 2007.
- 3 A. Riaz, H. Hesse, H. A. Tchelepi, and F. M. Orr, Jr. Onset of convection in a gravitationally unstable diffusive boundary layer in porous media. *Journal of Fluid Mechanics*, Vol. 548:87, 2006.
- 4 A. Riaz and H. A. Tchelepi. Numerical simulation of immiscible two-phase flow in porous media. *Physics of Fluids*, 18(1):14104, 2006.
- 5 A. Riaz and H. A. Tchelepi. Stability of two-phase vertical flow in homogeneous porous media. *Physics of Fluids* (In Press).
- 6 A. Riaz and H. A. Tchelepi. Dynamics of vertical displacement in saline aquifers associated with CO₂ sequestration. Submitted: *SPE Journal*.
- 7 M. Tyagi and P. Jenny, Stochastic particle method for nonlinear hyperbolic problems, presented at GAMM, Berlin, Germany, March 27-31, 2006.
- 8 M. Tyagi, P. Jenny, I. Lunati and H.A. Tchelepi. Multi-scale approach for multi-phase transport in porous media using stochastic particles, accepted in XVI International Conference on Computational Methods in Water Resources, Copenhagen, Denmark, June 19-22, 2006.
- 9 M. Tyagi, P. Jenny, I. Lunati, and H.A. Tchelepi. A lagrangian, stochastic modeling framework for multiphase flow in porous media, submitted to *Journal of Computational Physics*, 2007.
- 10 H. Zhou. Multiscale modeling of compressible multiphase flow in heterogenous porous media, M.S report, Stanford University (June 2006).
- 11 H. Zhou and H.A. Tchelepi. Operator Based Multiscale Method for Compressible Flow, SPE 106254, Presented at the SPE Reservoir Simulation Symposium, Houston, Texas, U.S.A, February 26-28, 2007.

References

1. S. Bachu, W. D. Gunter, and E. H. Perkins. Aquifer disposal of CO₂. Hydrodynamic and mineral trapping. *Enrg. Cons. Mang.*, 35:269, 1994.
2. W. D. Gunter, B. Wiwchar, and E. H. Perkins. Aquifer disposal of CO₂-rich green house gases: Extension of the time scale of experiment for CO₂-sequestering reactions by geochemical modeling. *Minr. Petr.*, 59:121, 1997.
3. J. Ennis-King and L. Paterson. Role of convective mixing in the long-term storage of carbon dioxide in deep saline formations. *SPE 84344*, pages 1–12, 2003.
4. A. Riaz, G.-Q. Tang, H. A. Tchelepi, and A. R. Kavscek. Forced imbibition in natural porous media: Comparison between experiments and continuum models. *Phys. Rev. E*, 75:036305, 2007.
5. A. Riaz, H. Hesse, H. A. Tchelepi, and F. M. Orr JR. Onset of convection in a gravitationally unstable diffusive boundary layer in porous media. *J. Fluid Mech.*, 548:87, 2006.
6. M. Wood, C. T. Simmons, and J. L. Hutson. A breakthrough curve analysis of unstable density driven flow and transport in homogeneous porous media. *Water. Resou. Res.*, 40:W03505, 2004.

7. M. Stohr and A. Khalili. Dynamic regimes of buoyancy-affected two phase flow in unconsolidated porous media. *Phy. Rev. E*, 73:036301, 2006.
8. T. Tokunaga, K. Mogi, O. Matsubara, and H. Tosaka. Buoyancy and interfacial force effects on two-phase displacement patterns: An experimental study. *AAPG Bul.*, 84:65, 2000.
9. R. Lenormand, E. Touboul, and C. Zarcone. Numerical-models and experiments on immiscible displacements in porous-media. *J. Fluid. Mech.*, 189:165, 1988.
10. B. Cockburn, C. Johnson, C.-W. Shu, and E. Tadmor. *Advanced numerical approximation of nonlinear hyperbolic equations*. Lecture notes in mathematics. Springer, Berlin, 1998.
11. S. K. Lele. Compact finite differences with spectral-like resolution. *J. Comput. Phys.*, 103:16, 1992.
12. A. Riaz and H. A. Tchelepi. Linear stability analysis of immiscible two-phase flow in porous media with capillary dispersion and density variation. *Phys. Fluids*, 16(12):4727, 2004.
13. L. L. Lake. *Enhanced Oil Recovery*. Prentice-Hall, Inc., 1989.
14. T. Xu, J. A. Apps, and K. Pruess. Reactive geochemical transport simulation to study mineral trapping for CO₂ disposal in deep arenaceous formations. *Journal of Geophysical Research*, 108(doi:10.1029/2002JB001979), 2003.
15. J. W. Johnson and J. J. Nitao. Reactive transport modeling of geologic CO₂ sequestration at Sleipner. In J. Gale and Y. Kaya, editors, *Greenhouse Gas Control Technologies*, volume 1, pages 327–333. Elsevier Science Ltd, 2003.
16. E. J. Spiteri, R. Juanes, M. J. Blunt, and F. M. Orr Jr. Relative permeability hysteresis: Trapping models and application to geological CO₂ sequestration. In *SPE Annual Technical Conference and Exhibition*, number SPE 96448, Dallas, TX, 9-12 October 2005 2005.
17. A. Kumar, R. Ozah, M. Noh, G. A. Pope, S. Bryant, K. Sepehrnoori, and L. W. Lake. Reservoir simulation of CO₂ storage in deep saline aquifers. *SPE Journal*, pages 336–348, September 2005.
18. R.C. Ozah, S. Lakshminarasimhan, G.A. Pope, K. Sepehrnoori, , and S.L. Bryant. Numerical simulation of the storage of pure CO₂ and CO₂-H₂S gas mixtures in deep saline aquifers. In *SPE Annual Technical Conference and Exhibition*, number SPE 97255-MS, Dallas, TX, 9-12 October 2005 2005.
19. S. Mo and I. Akervoll. Modeling long-term CO₂ storage in aquifer with a black-oil reservoir simulator. In *SPE/EPA/DOE Exploration and Production Environmental Conference*, number SPE 93951, Galveston, TX, 7-9 March 2005 2005.
20. S. Mo, P. Zweigel, E. Lindeberg, and I. Akervoll. Effect of geologic parameters on CO₂ storage in deep saline aquifers. In *SPE Eurospec/EAGE Annual Conference*, number SPE 93952, Madrid, Spain, 13-16 June 2005 2005.
21. J. Ennis-King and L. Paterson. Engineering aspects of geological sequestration of carbon dioxide. In *Asia Pacific Oil and Gas Conference and Exhibition*, number SPE 77809, Melbourne, Australia, 8 - 10 October 2002 2002.
22. I. N. Kochina, N. N. Mikhailov, and M. V. Filinov. Groundwater mound damping. *Int. J. Eng. Sci.*, 21:413–421, 1983.
23. H. E. Huppert and A. W. Woods. Gravity-driven flows in porous media. *J. Fluid Mech.*, 292:55–69, 1995.
24. G. I. Barenblatt. *Scaling, self-similarity, and intermediate asymptotics*. Cambridge University Press, 1996.
25. D.A. Collins J. Grabenstetter, Y.-K. Li and L.X. Nghiem. Stability-Based Switching

- Criterion for Adaptive-Implicit Compositional Reservoir Simulation. *SPE*, (21225), 1991.
26. Jr. P.A. Forsyth and P.H. Sammon. Practical Considerations for Adaptive Implicit Methods in Reservoir Simulation. *Journal of Computational Physics*, 62:265–281, 1986.
 27. T.F. Russell. Stability Analysis and Switching Criteria for Adaptive Implicit Methods Based on the CFL condition. *SPE*, (18416), 1989.
 28. G.W. Thomas and D.H. Turnau. Reservoir Simulation Using an Adaptive Implicit Method. *SPE*, (10120), 1983.
 29. G.W. Thomas and D.H. Turnau. The Mathematical Basis of the Adaptive Implicit Method. *SPE*, (25245), 1993.
 30. L.C. Young and T.F. Russell. Implementation of an Adaptive Implicit Method. *SPE*, (25245), 1993.
 31. E. Godlewski and P.A. Raviart. *Numerical Approximation of Hyperbolic Systems of Conservation Laws*. Springer Verlag, 1991.
 32. W. Hundsdorfer and J.G. Verwer. *Numerical Solution of Time-Dependent Advection-Diffusion-Reaction Equations*. Springer, 2003.
 33. Arieh Iserles. *Numerical Analysis of Differential Equations*. Cambridge University Press, 1996.
 34. B. Rubin and M.J. Blunt. High-Order Implicit Flux Limiting Schemes for Black-Oil Simulation. *SPE*, (21222), 1991.
 35. Alexander Kurganov and Eitan Tadmor. Non-oscillatory central differencing for hyperbolic conservation laws. *Journal of Computational Physics*, 87:408–463, 1990.
 36. Bjorn Engquist, Stanley Osher, and Sukumar R. Chakravarthy. Uniformly High Order Accurate Essentially Non-oscillatory Schemes. *Journal of Computational Physics*, 71:231–303, 1987.
 37. Chi-Wang Shu and Stanley Osher. Efficient implementation of essentially non-oscillatory shock capturing schemes. *Journal of Computational Physics*, 83:32–78, 1989.
 38. Guang-Shan Jiang and Chi-Wang Shu. Efficient Implementation of Weighted ENO Schemes. *Journal of Computational Physics*, 126:202–228, 1996.
 39. Robert D. Richtmyer and K.W. Morton. *Difference Methods for Initial Value Problems*. Krieger, 1967.
 40. Zoltan Horvath. On the positivity step size threshold of Runge-Kutta methods. *Applied Numerical Mathematics*, 53:341–356, 2005.
 41. Zoltan Horvath. Positivity of Runge-Kutta and diagonally split Runge-Kutta methods. *Applied Numerical Mathematics*, 28:309–326, 1998.
 42. P. Jenny, S. H. Lee, and H. A. Tchelepi. Multiscale finite-volume method for elliptic problems in subsurface flow simulation. *Journal of Computational Physics*, 187:47–67, 2003.
 43. T. Hou and X. H. Wu. A multiscale finite element method for elliptic problems in composite materials and porous media. *Journal of Computational Physics*, 134:169–189, 1997.
 44. Z. Chen and T. Hou. A mixed finite element method for elliptic problems with rapidly oscillating coefficients. *Mathematical Computation*, 72:541–576, 2003.
 45. T. Arbogast. Implementation of a locally conservative numerical subgrid upscaling scheme for two-phase darcy flow. *Computational Geosciences*, 6:453–481, 2002.
 46. T. Arbogast and S. L. Bryant. A two-scale numerical subgrid technique for waterflood simulations. *SPE Journal*, 7:446–457, 2002.
 47. I. Lunati and P. Jenny. Multiscale finite-volume method for compressible multiphase flow in porous media. *Journal of Computational Physics*, 216(2):616–636, 2005.

48. P. Jenny, S. H. Lee, and H. A. Tchelepi. Adaptive multiscale finite-volume method for multiphase flow and transport in porous media. *Multiscale Modeling and Simulation*, 3:50–64, 2004.
49. P. Jenny, S. H. Lee, and H. A. Tchelepi. Adaptive fully implicit multiscale finite-volume method for multiphase flow and transport in heterogeneous porous media. *Journal of Computational Physics*, 217:627–641, 2006.
50. Hui Zhou. Operator based multiscale method for compressible flow. Master's thesis, Stanford University, 2006.
51. M. A. Christie and M. J. Blunt. Tenth SPE comparative solution project: A comparison of upscaling techniques. *SPE Reservoir Eval. & Eng.*, 4:308–317, 2001.
52. S. Bachu, W.D. Gunther, and E.H. Perkins. Aquifer disposal of CO₂: hydrodynamic and mineral trapping. *Energy Conversion and Management*, 35:269–279, 1994.
53. K. Pruess and J. Garcia. Multiphase flow dynamics during CO₂ disposal into saline aquifers. *Environmental Geology*, 42:282–295, 2002.
54. K. Pruess, T. Xu, and J. Apps J. Garcia. Numerical modeling of aquifer disposal of CO₂. *SPE Journal*, 8:49–60, 2003.
55. A. Kumar, R. Ozah, M. Noh, G.A. Pope, S. Bryant, K. Sepehrnoori, and L.W. Lake. Reservoir simulation of CO₂ storage in deep saline aquifers. *SPE Journal*, 10:336–348, 2005.
56. R. Juanes, E.J. Spiteri, F.M. Orr Jr., and M.J. Blunt. Impact of relative permeability hysteresis on geological CO₂ storage. *Water Resources Research*, 42:W12418, doi:10.1029/2005WR004806, 2006.
57. G. I. Barenblatt, V. M. Entov, and V. M. Ryzhik. *Theory of Fluid Flows Through Natural Rocks*, volume 3 of *Theory and Applications of Transport in Porous Media*. Kluwer Academic Publishers, 1990.
58. D. Silin and T. Patzek. On barenblatt's model of spontaneous countercurrent imbibition. *Transport in Porous Media*, 54:297–322, 2004.
59. M. Tyagi, P. Jenny, H.A. Tchelepi, and I. Lunati. A lagrangian, stochastic modeling framework for multiphase flow in porous media. *submitted to Journal of Computational Physics*, 2007.
60. K. Pruess, T. Xu, J. Apps, and J. Garcia. Numerical modeling of aquifer disposal of CO₂. *SPE 66537 presented at the SPE/EPA/DOE Exploration and Production Environmental Conference held in San Antonio, Texas, 26-28 February, 2001*.
61. Y. Fan. Development of CO₂ sequestration modeling capabilities in Stanford General Purpose Research Simulator. *M.S. Thesis*, June, 2006.
62. L.X. Nghiem, P. Sammon, J. Grabenstetter, and H. Ohkuma. Modeling CO₂ storage in aquifers with a fully-coupled geochemical EOS compositional simulator. *SPE 89474 presented at the SPE/DOE Symposium on Improved Oil Recovery held in Tulsa, Oklahoma, 17-21 April, 2004*.
63. T. Xu and K. Pruess. Coupled modeling of non-isothermal multiphase flow, solute transport and reactive chemistry in porous and fractured media: 1. Model development and validation. *Lawrence Berkeley National Laboratory Report LBNL-42050, Berkeley, CA, 1998*.
64. J.J. Nitao. Reference manual for the NUFT flow and transport code, version 2.0. *UCRL-MA-130651*, 1998.
65. UTCHEM-9.0: A three-dimensional chemical flood simulator. *Reservoir Engineering Research Program Center for Petroleum and Geosystems Engineering Technical Documentation*, University of Texas at Austin, July, 2000.

Contacts

Khalid Aziz: aziz@stanford.edu
Louis J. Durlfolsky: lou@stanford.edu
Yaqing Fan: yaqing@stanford.edu
Marc Hesse: mhesse@pangea.stanford.edu
Patrick Jenny: jenny@ifd.mavt.ethz.ch
Romain de Loubens: rloubens@stanford.edu
Franklin M. Orr, Jr: fmorr@pangea.stanford.edu
Amir Riaz: ariaz@stanford.edu
Hamdi Tchelepi: tchelepi@stanford.edu
Manav Tyagi: tyagi@ifd.mavt.ethz.ch
Hui Zhou: huizhou@pangea.stanford.edu